Growth and Characterisation of Metal Alloy and Metal Oxide Surfaces

by

Katarzyna Jadwiga Krupski

Thesis

Submitted to the University of Warwick in partial fulfilment of the requirements for admission to the degree of

Doctor of Philosophy

Department of Physics

2017

Contents

List of Figures

List of Tabels

Acknowledgements

Firstly, I should thank my supervisor Prof. Chris McConville for his help, support, and encouragement in guiding me through this PhD. Secondly, I would like to thank the many members of the surface science group, in particular Dr. Sean McMittchel for his excellent introduction to PLD, Dr. David Walker for introduction XRD and Dr. Neil Wilson for introduction to AFM, at the start of this PhD, Rob Johnston for his excellent technical support and discussions. The people I have shared an office with: Dr. Aleksander Krupski, Badriya Al. Hashami, Philip Mousley and Stephanie Greis. Other past and present members of thegroup: Dr. Marc Walker, Dr. Chris Burrows, Dr. Daesung Park, Dr. Nessa Fereshteh Saniee, Dr. Sep Vasheghani Farahani, Haiyuan Wang, Collins Ouserigha are all thanked for their help and friendship during this PhD. Dr. Gavin Bell, and Dr. Ana Sanchez are all thanked for helpful scientific discussions, and pointing me in the right direction, resulting in the completion of this thesis.
Finally, I would like to thank my my Husband and friends for their support throughout my studies, without which I would have not made it to this point.

I would like to dedicate this thesis to my Son – Joshua who change my life and gave me power to finish this PhD. I love you!

Declarations

I declare that this thesis contains an account of my research work carried out at the Department of Physics, University of Warwick, between October 2012 and July 2017 under the supervision of Prof. C. F. McConville. The research reported here has not been previously submitted, wholly or in part, at this or any other academic institution for admission to a higher degree.

Dr. Anna Sanchez (University of Warwick) was performed the TEM measurements presented in figure 3.11.(a) and 3.12.(a). Dr. Aleksander Krupski (University of Portsmouth) was performed the STM and LEED measurements presented in figures 4.2-4.4. Dr. Marco Moors (Peter Grünberg Institut (PGI-7) and JARA-FIT, Forschungszentrum Jülich GmbH) was performed the STM and LEED measurements presented in figures 5.1.(a)-(d) and 5.3.

All the remaining data collection, simulations and analysis have been performed by the author.

Dr Katarzyna Krupski

June 2017

Peer Reviewed Papers

Published articles related to this work:

K. Krupski, A.M. Sanchez, A. Krupski, C.F. McConville, *„Optimisation of anatase TiO_2 thin film growth on $LaAlO_3(001)$ Using pulsed laser deposition"*, Applied Surface Science **388** (2016) 684

K. Krupski, M. Moors, P. Jóźwik, T. Kobiela and A. Krupski *"Structure determination of Au on Pt(111) surface: LEED, STM and DFT study."* Materials **8** (2015) 2952

Articles in preparation related to this work:

K. Krupski, C.F. McConville , *„DFT study about structure determination of Pt_3Ti."* in preparation to be submitted to App. Phys. Lett.

Conference Contributions

Oral Presentations

"Structural Optimization Of Titanium Dioxide of (4×1) Reconstruction for Photocatalytic Applications." Seminar on: XPS and TEM applied to surfaces and interfaces characterization." Warsaw, Poland. (26 II 2015).

"Structural Optimization Of Photocatalytic Titanium Dioxide of (4×1) reconstruction." EMRS Fall Meeting2014, Warsaw, Poland. (15 IX 2014).

Poster Presentations

"Structural Optimization Of Titanium Dioxide of (4×1) Reconstruction for Photocatalytic Applications." ISSC-20. Birmingham, United Kingdom. (III-IV 2015)

"Structure determination of CdO(100): A combined quantitative LEED and DFT study." ISSC-20. Birmingham, United Kingdom. (III-IV 2015)

"Structure determination of TiO_2(001)-(4×1) surface using quantitative low-energy electron diffraction." ICSOS-11. Coventry, United Kingdom. (VII 2014).

"Structure determination of CdO(100): A combined quantitative LEED and DFT study." ICSOS-11. Coventry, United Kingdom. (VII 2014).

"Structure determination of TiO_2(001)-(4×1) surface using quantitative low-energy electron diffraction." DPG-Frühjahrstagung 2014. Dresden, Germany.(IV 2014).

"Structure determination of CdO(100): A combined quantitative LEED and DFT study." DPG-Frühjahrstagung 2014. Dresden, Germany. (IV 2014).

Abstract

Optimisation of epitaxial anatase TiO_2 thin films grown on $LaAlO_3(001)$ substrates was performed using ultra-high vacuum based pulsed laser deposition (PLD) and studied by in-situ reflection high-energy electron diffraction (RHEED). In addition, ex-situ X-ray diffraction (XRD), atomic force microscopy (AFM), and scanning transmission electron microscopy (STEM) were performed to characterise the bulk properties of these thin films. The deposited TiO_2 thin film is demonstrated to have anatase phase and bonded directly to the $LaAlO_3(001)$ substrate. In a separate ultra-high vacuum system low-energy electron diffraction (LEED) and scanning tunnelling microscopy (STM) measurements were performed and a well-ordered two-domain (1×4) and (4×1) reconstruction of anatase surface was observed. Analysis of the STM measurements indicates the coexistence of atomic steps of both 2.5 Å and 5.0 Å, confirming the existence of two TiO_2 domains. The atomic resolution STEM images reveal that the $TiO_2/LaAlO_3$ interface to be terminated with LaO layer and that the anatase-TiO_2 reconstruction was found to be stable during the film growth.

Low-energy electron diffraction (LEED), scanning tunneling microscopy (STM) and density functional theory (DFT) calculations have been used to investigate the atomic and electronic structure of gold deposited (between 0.8 and 1.0 monolayer) on the Pt(111) face in ultrahigh vacuum at room temperature. The analysis of LEED and STM measurements indicates two-dimensional growth of the first Au monolayer. Change of the measured surface lattice constant equal to 2.80 Å after Au adsorption was not observed. Based on DFT, the distance between the nearest atoms in the case of bare Pt(111) and Au/Pt(111) surface is equal to 2.83 Å, which gives 1% difference in comparison with STM values. The first and second interlayer spacing of the clean Pt(111) surface are expanded by +0.87% and contracted by −0.43%, respectively. The adsorption energy of the Au atom on the Pt(111) surface is dependent on the adsorption position, and there is a preference for a hollow *fcc* site. For the Au/Pt(111) surface, the top interlayer spacing is expanded by +2.16% with respect to the ideal bulk value. Changes in the electronic properties of the Au/Pt(111) system below the Fermi level connected to the interaction of Au atoms with Pt(111) surface are observed.

Detailed structural properties of the $Pt_3Ti(111)$ surface have been studing with the use of ab initio density functional theory calculations and scanning tunelling microscopy measurements. The DFT calculations show that the atoms composition of the second and third atomic layer have influence upon the top surface of the Pt_3Ti.

Abbreviations

AES	Auger Electron Spectroscopy
AFM	Atomic Force Microscopy
ARPES	Angle Resolved Photoelectron Spectroscopy
BFGS	Broyden-Fletcher-Goldfarb-Shanno Geometry Optimisation
bcc	Body Centred Cubic
CASTEP	Cambridge Serial Total Energy Package
DFT	Density Functional Theory
DOS	Density Of States
EC-STM	Electrochemical Scanning Tunneling Microscopy
fcc	Face Centred Cubic
FL	Fermi Level
FWHM	Full Width At Half Maxium.
GGA	Generalized Gradient Approximation
hcp	Hexagonal Close-Packed
HEIS	High Energy Ion Scattering
IMFP	Inelastic Mean Free Path
KE	Kinetic Energy
LEED	Low Energy Electron Diffraction
LDA	Local Density Approximation
MBE	Molecular Beam Epitaxy
MEIS	Medium Energy Ion Scattering
ML	Monolayer
NN	The Nearest Neighbor
NNN	Next-Nearest Neighbor
ORR	Oxygen Reduction Reaction
PAMBE	Plasma Assisted Molecular Beam Epitaxy
PAW	Projector Augmented Wave
PBE	Perdew-Burke-Ernzerhof Functional
PW91	Perdew-Wang 1991 Functional
RPBE	Revised Perdew-Burke-Ernzerhof Functional
PDOS	Partial Density Of States

PLD	Pulsed Laser Deposition
RHEED	Reflection High-Energy Electron Diffraction
STEM	Scanning Transmission Electron Microscopy
STM	Scanning Tunneling Microscopy
SXRD	Surface X-ray Diffraction
TPD	Temperature Programmed Desorption
TEM	Transmission Electron Microscopy
UHV	Ultra High Vacuum
UPS	Ultraviolet Photoelectron Spectroscopy
XPS	X-ray Photoelectron Spectroscopy
XRD	X-ray Diffraction
XRR	X-ray Reflectivity

Chapter 1

Introduction

1.1. Outline of the Thesis

The work presented in this thesis focuses upon the growth and characterisation of metal alloy and metal oxide surfaces of $TiO_2/LaAlO_3$, Au/Pt(111) and $Pt/Pt_3Ti(111)$. The remainder of the current chapter introduces some general properties of the titanium dioxide, platinum and Pt_3Ti alloy. A set of experimental techniques have been used to investigate the properties of materials mentioned above, and these are introduced in Chapter 2. Chapter 3 followed by an overview of the theoretical methods and background required for analysing the data in the thesis, including underlying theory of DFT and highlights the approximations made when using the the Cambridge Serial Total Energy Package (CASTEP) code. The aim of the study presented in Chapter 4 is the optimisation of the Pulsed Laser Deposition (PLD) growth parameters to generate smooth, flat surfaces and a well-defined interface between film and substrate. Bulk and surface characterization of the anatase-TiO_2(001)-(4×1) films on $LaAlO_3$(001) using Reflection High-Energy Electron Diffraction (RHEED), Low Energy Electron Diffraction (LEED), X-ray diffraction (XRD), atomic force microscopy (AFM), scanning tunnelling microscopy (STM), and scanning transmission electron microscopy (STEM). Chapter 5 presented study of the structural and electronic properties during the initial adsorption process of gold on Pt(111) surface at room temperature, performed by LEED, STM measurements, and density functional theory (DFT) calculations with the use of CASTEP code. Structural properties of surface terminations and adsorption position of Pt atom on Pt_3Ti and Pt terminated surfaces are described in the chapter 6. Finally, in Chapter 7 the outlook for conclusions and future work is presented.

1.2. Titanium Dioxide

Titania, TiO_2, has a wide range of applications and a large number of extremely interesting properties. A key 'low-tech' application that stems not only from its optical properties, but also its non-toxicity, is use as a whitening agent in paints and paper. However, applications that more directly stem from its surface properties, as well as the bulk, arise in heterogeneous catalysis including photo-catalysis [1-2], the photovoltaic effect [3-4], and collar cells [5], and it is these applications that are at least part of the reason why TiO_2 is almost certainly the most studied of all oxides surface [6]. Until now, the majority of studies of TiO_2 have been performed on the rutile phase [7-9]. Rutile is the thermodynamically equilibrium phase of TiO_2 at ambient pressures, but two other isomorphs, anatase and brookite also occur naturally. Crucially anatase appears to be the equilibrium phase for small particles with dimension less than 11 nm [2]. It is therefore generally believed that anatase is the active component in many titania based heterogeneous catalysts [4, 10] and in current solar cell applications based on nano-crystalline material. Anatase phase of TiO_2 is crystalise in space group 141 $I4_1/amd$ with lattice parameters a=b=3.7845Å and c=9.5143 Å (Figure 1.1).

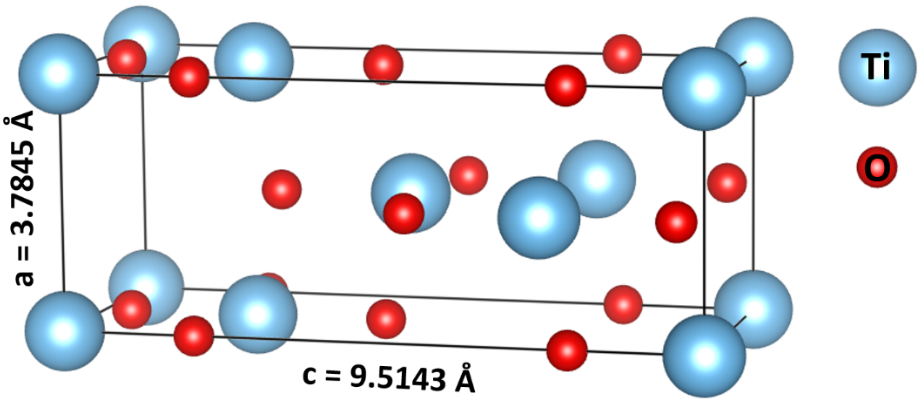

Figure 1.1. *The crystal structure of TiO_2 Anatase phase (space grupe 141 $I4_1/amd$) structure with lattice distance a=b=3.7842Å and c=9.5143Å.*

As such, there is a clear need to gain a better understanding of the anatase surface structure and the role of the TiO_2 growth conditions (e.g. substrate temperature, oxygen pressure - during growth and annealing, etc.). TiO_2 anatase and LAO (Figure 1.2) are both conventional band insulators, with in-plane bulk lattice parameter a=3.79Å [11]. The small mismatch between the in-plane lattice constants allows for a good epitaxial experimental outcome [12].

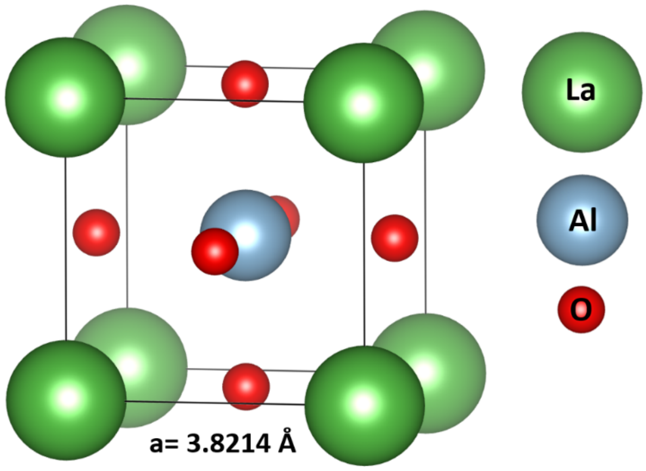

Figure 1.2. *The crystal structure of $LaAlO_3$ (space group 221) with lattice constant a=3.8214 Å.*

1.3. Platinum

Platinum is scystaline in fcc structure with the lattice constant 3.9242Å (Figure 1.3). A large number of studies on epitaxy have been carried out for many years. Ultra-thin epitaxial film systems exhibit a variety of interesting properties due to the strong correlation between the electronic structure of the film and its morphology, strain, and defect structure [13-22]. Structural studies of *fcc/fcc* systems provide a great deal of information on the connection between the geometrical properties of the adsorbed atomic layers and the atomic arrangements of the substrates. Various fields are concerned with epitaxial growth; these range from basic research on the growth mechanism of thin films to advanced research on the development of devices. Platinum is widely used as a catalyst in the chemical and petrochemical industries [23, 24]. For example, in oil refineries, platinum catalysts are employed in processes that involve the reforming of paraffin and the hydrogenation of unsaturated hydrocarbons [23-26]. The clean Pt(111) surface itself has been the subject of several structural determinations with Low Energy Electron Diffraction (LEED) [27-35], medium energy ion scattering (MEIS) [36], high energy ion scattering (HEIS) [37] and surface X-ray diffraction (SXRD) [38, 39]. Differently from the other noble metal (111) surfaces, clean Pt(111) normally has an unreconstructed bulk-periodic surface [35,40-42]. Adams *et al.* [30] found the first layer spacing to be possible to expand by 0.04 ± 0.10 Å, while Hayek *et al.* [33] found an unrelaxed surface with 0.05 Å. Materer *et al.* [35] found the first and second interlayer spacing expanded by 0.04 ± 0.10 Å and 0.005 ± 0.03 Å, respectively. MEIS and HEIS experiments [36,37] support the LEED results.

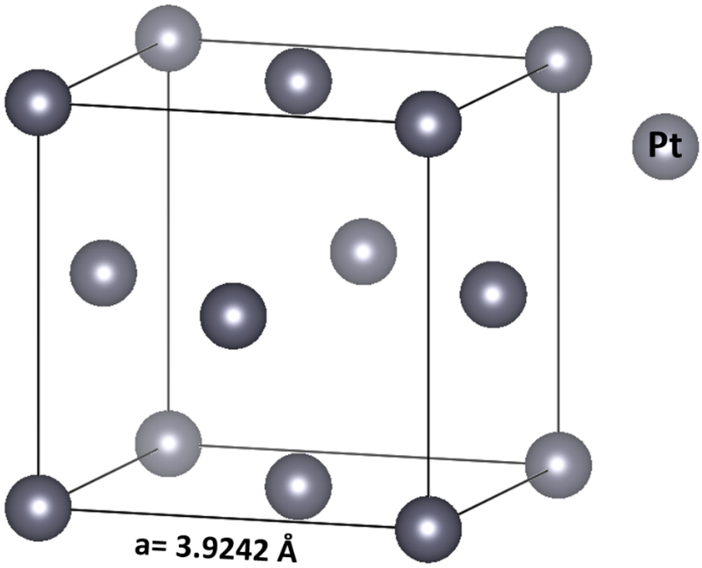

Figure 1. 3. *The crystal structure of Platinum which crystalise in fcc (space group 255 Fm-3m) structure with lattice distance 3.9242Å.*

Namely, the ion scattering data indicate that the Pt(111) structure deviates from the bulk geometry by a possible small outward expansion of the top interlayer spacing of 0.03 ± 0.02 Å [36] or 0.03 ± 0.02 Å [37]. No deviation from the bulk position was found in the direction parallel to the surface, with a small accuracy of about 0.01 ± 0.02 Å. The surface geometry of clean Pt(111) has been the subject of surface X-ray diffraction investigations [26]. These investigations gave an outward relaxation of the topmost layer of 0.045 ± 0.005 Å (+2.0%) with respect to the ideal bulk termination.

1.4. Pt_3Ti

Pt_3Ti is a stoichiometric intermetallic phase, which crystallizes in the Cu_3Au-type with a cubic face centered structure and a lattice constant of 3.906 Å (Figure 1.4). Pure platinum lattice constant is only 0.4% bigger than Pt_3Ti [43]. This results in an interatomic distance of 0.276 nm on the hexagonal (111) orientated surface. Results presented by LEED show that the titanium atoms create a p(2 × 2) superstructure with respect to the p(1×1) structure of a pure Pt(111) crystal [44-46]. STM studies confirmed the p(2×2) superstructure but not the p(1×1) [43]. The crystal structure remains stable up to its high melting point of 2213 K. It seems, that this is caused by a strong interaction of the Pt 5d and the Ti 3d bands in the bulk. Such properties are very important for a catalytic applications [46–48]. It should be pointed out, that the system has been investigated since the 1980ies, but the fundamental question about the composition of the outermost atomic layer of the clean alloy surface has not been definitely solved yet. Early studies by Paul et al. interpreted the similarity of thermal desorption spectroscopy (TDS) measurements of CO on $Pt_3Ti(111)$ and Pt(111) with a pure Pt termination of the outermost atomic layer. Core level photoemission measurements under grazing incidence [49] and tensor LEED experiments [50] by Chen et al. lead to the same conclusion. In contrast to these findings other LEED and TDS measurements by Bardi et al. indicated a bulk-like termination consisting of 75 % platinum and 25 % titanium atoms [51-52]. The above mentioned catalytic CO conversion also argues for the existence of Ti atoms on the top layer [53]. DFT calculations done by Duan et al. might explain these contrary results. They found that the affinity towards a surface reconstruction depends very strongly on the alloy composition. Samples with a slightly Pt enriched stoichiometry (i.e. more than the theoretical 75 % value) tend to segregate Pt atoms to the surface in order to form a pure Pt outermost layer, while the second layer and below remain stoichiometric [54].

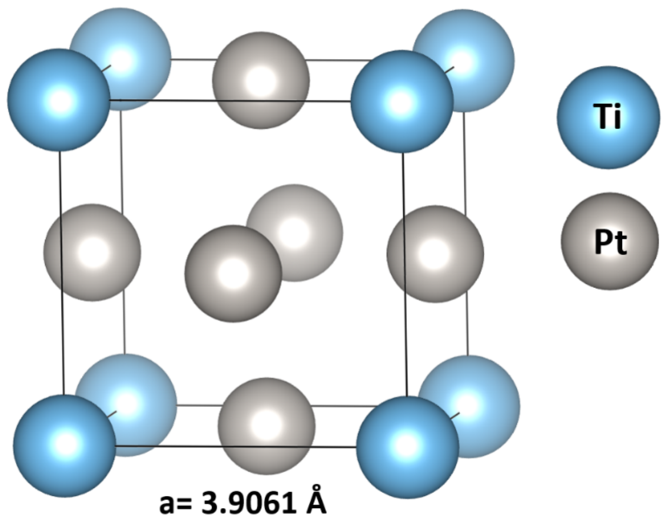

Figure 1.4. *The crystal structure of Pt_3Ti which crystalise in space group 221 Pm-3m. Lattice distance of Pt_3Ti is 3.9061Å.*

References

[1] R. Asahi, T. Morikawa, T. Ohwaki, K. Aoki, and Y. Taga, Science, **293** (2001) 269.

[2] O. Carp, C.L. Huisman, and A. Reller, Prog. Solid State Chem. **32** (2004) 33.

[3] C. J. Barbe, F. Arendse, P. Comte, M. Jirousek, F. Lenzmann, V. Shklover, and M. Gratzel, J. Am. Ceram. Soc. **80** (1997) 3157.

[4] W. Zhou, F. F. Sun, K. Pan, G. H. Tian, B. J. Jiang, Z. Y. Ren, C. G. Tian, and H. G. Fu, Adv. Functional Mater. **21** (2011) 1922.

[5] T.B. Song, Q. Chen, H. Zhou, C. Jiang, H.H. Wang, Y. Yang, Y. Liu, J. You, and Y. Yang, J. Mater. Chem. A **3** (2015) 9032.

[6] D.P. Woodruff (ed.) *The Chemical Physics of Solid Surface*, *Vol. 9 Oxide Surfaces* (Elsevier, Amsterdam, 2001).

[7] U. Diebold, Surf. Sci. Rep. **48** (2003) 53.

[8] M.A. Henderson, Surf. Sci. Rep. **46** (2002) 5.

[9] C.L. Pang, R. Lindsay, and G. Thornton, Chem. Soc. Rev. **37** (2008) 2328.

[10] G.S. Herman, M.R. Sievers, and Y. Gao, Phys. Rev. Lett. **84** (2000) 3354.

[11] S. Kitazawa, Y. Choi, S. Yamamoto, T. Yamaki, Thin Solid Films **515** (2006) 1904

[12] A. Lotnyk, S. Senz, D. Hesse Thin Solid Films **515** (2007)

[13] F. Himpsel. J. Ortega, G. Mankey, *Adv. Phys. **47*** (1998) 511.

[14] J. Larsen, I. Chorkendorff, *Surf. Sci. Rep. **35*** (1999) 163.

[15] A. Krupski, *J. Phys. Condens. Matter* **26** (2014) 053001.

[16] M. Jiang, E. Sak, K. Gentz, Krupski, K. Wandelt, *ChemPhysChem* **11** (2010) 1542.

[17] A. Krupski, S. Mróz, *Surf. Rev. Lett.* **10** (2003) 65.

[18] S. Mróz, M. Nowicki, A. Krupski, *Prog. Surf. Sci.* **74** (2003) 109.

[19] A. Krupski, S. Mróz, *Surf. Rev. Lett.* **10** (2003) 843.

[20] L. Jurczyszyn, A. Krupski, S. Degen, B. Pieczyrak, M. Kralj, C. Becker, K. Wandelt, *Phys. Rev. B* **76 (2007)** 04510101.

[21] A. Krupski, *Phys. Rev. B **80*** (2009), 0354241.

[22] K. Miśków, A. Krupski, K. Wandelt, *Vacuum* **101** (2014) 71.

[23] J.M. Thomas, W.J. Thomas, *Principles and Practice of Heterogeneous Catalysis*; VCH: New York, NY, USA, 1997.

[24] G.A. Somorjai, *Introduction to Surface Chemistry and Catalysis*; Wiley: New York, NY, USA, 1994.

[25] R.I. Masel, *Principles of Adsorption and Reaction on Solid Surfaces*; Wiley: New York, NY, USA, 1996.

[26] J.G. Speight, *The Chemistry and Technology of Petroleum*, 2nd ed.; Marcel-Dekker: New York, NY, USA, 1991.

[27] L.L. Kesmodel, G.A. Samorjai, *Phys. Rev. B* **11** (1975) 630.

[28] L.L. Kesmodel, P.C. Stair, G.A. Somorjai, *Surf. Sci.* **64** (1975) 342.

[29] R. Feder, *Surf. Sci.* **68** (1977) 229.

[30] D.L. Adams, H.B. Nielsen, M.A. van Hove, *Phys. Rev. B* **20** (1979) 4789.

[31] P. Bauer, R. Feder, N. Mueller, *Surf. Sci.* **99** (1980) L395.

[32] R. Feder, H. Pleyer, P. Bauer, N. Mueller, *Surf. Sci.* **109** (1981) 419.

[33] K. Hayek, H. Glassl, A. Gutmann, H. Leohard, *Surf. Sci.* **152-153** (1985) 419.

[34] D.F. Ogletree, M.A. van Hove, G.A. Samorjai, *Surf. Sci.* **173** (1986) 351.

[35] N. Materer, U. Starke, A. Barbieri, R. Doell, K. Heinz, M.A. van Hove, G.A. Samorjai, *Surf. Sci.* **325** (1995) 207.

[36] J.A. Davies, D.P. Jackson, N. Matsunami, P.R. Norton, *Surf. Sci.* **78** (1978) 274.

[37] J.F. Van der Veen, R.G. Smeenk, R.M. Tromp, F.W. Saris, *Surf. Sci.* **79** (1979) 219.

[38] R. Felici, M. Pedio, F. Borgatti, S. Iannotta, M. Capozi, G. Ciullo, A. Stierle, *Nat. Mater.***4** (2005) 688.

[39] A. Krupski, K. Krupski, A. Bailly, M.C. Saint-Lager, R. Baudoing-Savois,P. Dolle, C. Becker, K. Wandelt, Structure determination of the Pt(111)(2 × 2)-Sn and Pt(111)(√3 × √3)R30°-Sn surface alloys: Surface X-ray-Diffraction and DFT study. In preparation.

[40] G. Grübel, K.G. Huang, D. Gibbs, D.M. Zehner, R.S. Sandy, S.G.J. Mochrie, *Phys. Rev. B* **48** (1993) 18119.

[41] A.R. Sandy, S.G.J. Mochrie, D.M. Zehner, K.G. Huang, D. Gibbs, *Phys. Rev. B* **43** (1991) 4667.

[42] P.J. Feibelman, *Phys. Rev. B* **56** (1997) 2175.

[43] W. Chen, L. Severin, M. Göthelid, M. Hammar, S. Cameron and J. Paul, Phys. Rev. B: Condens. Matter, **50** (1994) 5620.

[44] W. Chen, J. A. K. Paul, A. Barbieri, M. A. van Hove, S. Cameron and D. J. Dwyer, J. Phys.: Condens. Matter, **5** (1993) 4585.

[45] S. Le Moal, M. Moors, J. M. Essen, C. Breinlich, C. Becker and K. Wandelt, J. Phys.: Condens. Matter, **25** (2013) 045013.

[46] S. Le Moal, M. Moors, J. M. Essen, C. Becker and K. Wandelt, Surf. Sci., **604** (2010) 1637.

[47] S. Ringler, E. Janin, M. Boutonnet-Kizling and M. Gothelid, Appl. Surf. Sci., 162 (2000)190.

[48] W. Chen, E. Chulkovl and J. Paul, Phys. Scr., **54** (1996) 392.

[49] W. Chen, L. Severin, M. Göthelid, M. Hammar, S. Cameron, J. Paul, Phys. Rev. B **50** (1994) 5620.

[50] W. Chen, J. Paul, A. Barbieri, M. Van Hove, S. Cameron, D.J. Dwyer, *J.Phys. Condens. Matter* **5** (1993) 4585.

[51] U. Bardi, P.N. Ross, *Surf. Sci.* **146** (1984) L555.

[52] U. Bardi, D. Dahlgren, P.N. Ross, *J. Catal.* **100** (1986) 196.

[53] S. Le Moal, M. Moors, J.M. Essen, C. Becker, K. Wandelt, *Surf. Sci.* **604** (2010) 1637.

[54] Z. Duan, J. Zhong, G. Wang, *J. Chem. Phys.* **133** (2010) 114701.

Chapter 2

The current Chapter contains brief description of the experimental methods used to grow and characterize the metal alloys and metal oxides surfaces. First part of the Chapter is focused on the pulsed laser deposition technique. Next, the diffraction methods (Low-Energy Electron Diffraction (LEED), Reflection high-energy electron diffraction (RHEED), X-ray Diffraction (XRD) incl. reflectivity) are described. Finally, the microscopy methods Scanning Tunneling Microscope (STM) and Atomic Force Microscopy (AFM) are introduced.

Experimental and Theoretical Techniques

2.1. Pulsed Laser Deposition

Pulsed laser deposition (PLD) [1-3] is one of the most powerful deposition techniques using a high-powered UV pulsed laser to ablate material from a target. Next, a plasma plume is formed, which then condenses on a heated saple placed opposite the target. Mainly, this takes place in the presence of a background oxygen, nitrogen or some other gas atmosphere. The photonic energy is coupled to the bulk material of the target and is converted into electronic excitations. A transfer of energy from the electrons to the lattice occurs within a few picoseconds and heating begins [1].

The growth parameters include: the KrF pulsed laser frequency; laser energy density; and oxygen pressure during deposition, all play a crucial role in the formation of proper epitaxial TiO_2 phase. The geometry of the ultra-high vacuum pulsed deposition system (including the sample holder to target distance), Figure 2.1, affects the

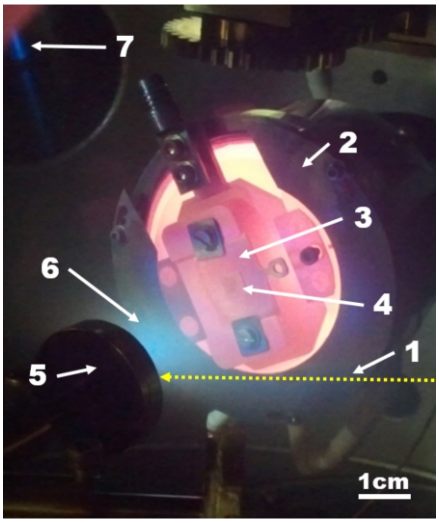

Figure 2.1. *Geometry of the ultra-high vacuum pulsed laser deposition system: (1) KrF pulsed laser beam, (2) sample holder, (3) stainless steel sample plate, (4) $LaAlO_3$(001) sample, (5) TiO_2 target, (6) laser ablation plume, (7) RHEED screen.*

material transport between the target and the substrate. The substrate temperature influences the thermodynamic equilibrium for the well-defined epitaxial growth of atomically flat surfaces. Furthermore, the correct stoichiometry of the substrate surface (in this case $LaAlO_3$) during heating, deposition and cooling to the room temperature after deposition, is ensured by the use of the proper oxygen pressure. Further, the proper shape of the laser ablation plume corresponds to well-chosen laser energies and the oxygen pressures.

The laser pulse is absorbed in the target within the optical absorption depth, $1/\alpha$, where α is the optical absorption coeficient. If $1/\alpha$ is smaller than the thermal difusion length, ($l_T = 2\sqrt{D\tau}$, where D is the thermal diffusion constant and τ is the laser pulse duration), such as is the case in metals, then all the photonic energy is deposited into the optical absorption depth and e-ciently heats the target down to a depth of l_T during the laser pulse. As a result, the ejection of thermal particles is observed which can lead to nonstochiometric ablation. However, in the case when $1/\alpha$ is larger than l_T , as it happends for most complex oxides and insulators, then the material is only heated within the optical absorption depth and the condition for stoichiometric transfer is met. In such regime, with ns pulse durations, laser supported ablation takes place where only around the first 100 picoseconds of the laser pulse ablates material from the target. The bulk is then protected from the remainder of the laser pulse by the plasma which absorbs the energy becoming more ionized and increasingly hotter. This is true by assuming that in most cases the materials used in PLD have an extinction coeffcient, ξ, of approximately 1.5 [1,4]. In this situatation, the absorption depth (= around 13nm) is given by

$$\frac{1}{\alpha} = \frac{\lambda}{4\pi\xi}, \qquad (2.1)$$

for these materials.

If there is a laser focus on the target of 2 mm^2 then the absorption volume contains approximately 3×10^{-9} moles. The enthalpy of vaporisation for most materials deposited in PLD is of the order of 500 kJ mol^{-1} [1,5] and therefore, only 1.5 mJ is required for vaporisation of the optical absorption depth. If it is assumed that the total photonic energy of each 20 ns laser pulse is 30 mJ then only 5% of the pulse energy is used in vaporising, leaving 95% to ionise the plume.

After the plasma is formed in a layer next to the target it starts to expand outwards due to the high local pressure. The expansion of gas can cause particulates or "laser droplets" to be ejected into the plume from the heated target because of the contact with the hot plasma. The other possible mechanism for the creation of laser droplets is if the time required for the laser energy to be converted into heat in the bulk is shorter than the time that is required for the surface layer to be vaporised. In such case, the underlayers ejects droplets from the surface layer [1,6]. In addition, the solid particulates can be expelled from the target when surface roughening caused by the laser becomes signficant [1,7]. The outgrowths within the roughened area can fracture and be released into the plasma if the conditions are suitable. Described effects of these mechanism can be eliminated or reduced by selecting the depostion parameters.

When the plasma starts to expand out from the target it forms so called "plume" [2,8]. The shape and size of the "plume" is determined by the angular distribution of kinetic energy of the ablated particles and the pressure of the background atmosphere. The plumes have a standard form [8] with a number of possible features as shown in Figure 2.2. The core is the brightest area of a plume which is adjacent to the point on the target where the laser is impinging. From the core, a central stream is directed orthogonally away from the target surface as a result of the high kinetic energy of the ablated particles in this direction. Surrounding the core is a less luminous body and surrounding the central stream there is a finger of similar brightness. Depending on deposition parameters and the ablated there could be a "halolike" feature where the light emission is even lower than in the body and finger. The background pressure can influence the size and shape of the plume. As the background pressure is decreased

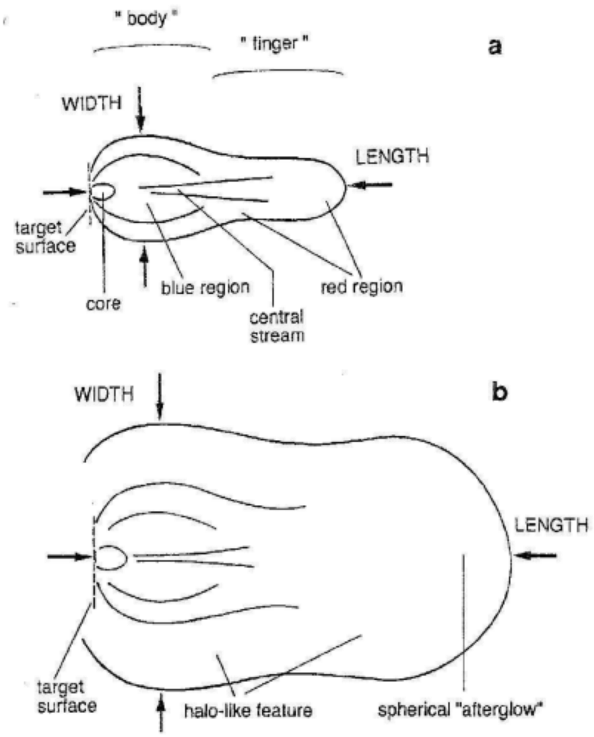

Figure 2.2. *Schematic diagram of a plasma plume [8]: (a) without, and (b) with the halo-like features occasionally seen. The colours refer to the plume from a YBCO target ablated in oxygen.*

the shape changes from having a halolike structure through having a more pronounced body and finger shape, with the plume getting longer, to at lower pressures the plume growing ever more spherical in shape, all the while the plume getting larger before thermalizing.

By decreasing the laser spot size on the target, the plume becomes spherical, and with less material per pulse being ablated the size of the plume decreases. As with the effect of spot size on the plume, decreasing the fluence of the laser beam decreases the amount of ablated material in the plume and so makes it smaller.

In the next step, the particles from the plume recondense on the sample surface placed directly in front of the target. To promote surface disfussion of the adatoms to stable positions, the substrate is held at elevated temperatures. However, this high temperature also increases the probability of a small percentage of the adatoms being reevaporated. The way, the adatoms settle in stable sites and the manner in which the crystal structure of the film grows depends on a number of factors like lattice mismatch between the substrate and the growing film and surface mobility.

The PLD-RHEED system wich was used during the growth optimization of the $TiO_2/LaAlO_3(001)$ system is shown on Figure 2.3 and Figure 2.4. This system with *in-situ* X-ray photoemission spectroscopy (XPS) and STM system consisted of an external Excimer laser source in addition to two UHV chambers with independent pumping systems. Thos systems are connected by a valve gate and a transfer arm which allowed to transfer sample in UHV. This UHV system was made on the way of collaboration between Omicron GmbH and Twente Solid State Technologies (TSST). The typical preassure inside the PLD/RHEED chamber operated by turbo pumps was 4×10^{-8}mbar and inside STM/XPS operated by turbo and ion pumps was chamber 2.1×10^{-11}mbar. The laser used during deposition process in this work was a Lambda Physik LPXPro 210, from Coherent GmbH. Using Krypton Fluoride (KrF) as the active lasing medium gives an output at a wavelength of 248 nm. This wavelength provides the high photon energy required in PLD to initiate the laser ablation. The maximum repetition rate for the LPXPro 210 laser was 100 Hz (can be varied from 1 to 100 Hz), nominal pulse energy of 1000 mJ and maximum average power of 65 W. The pulse duration was 25 ns for this laser.

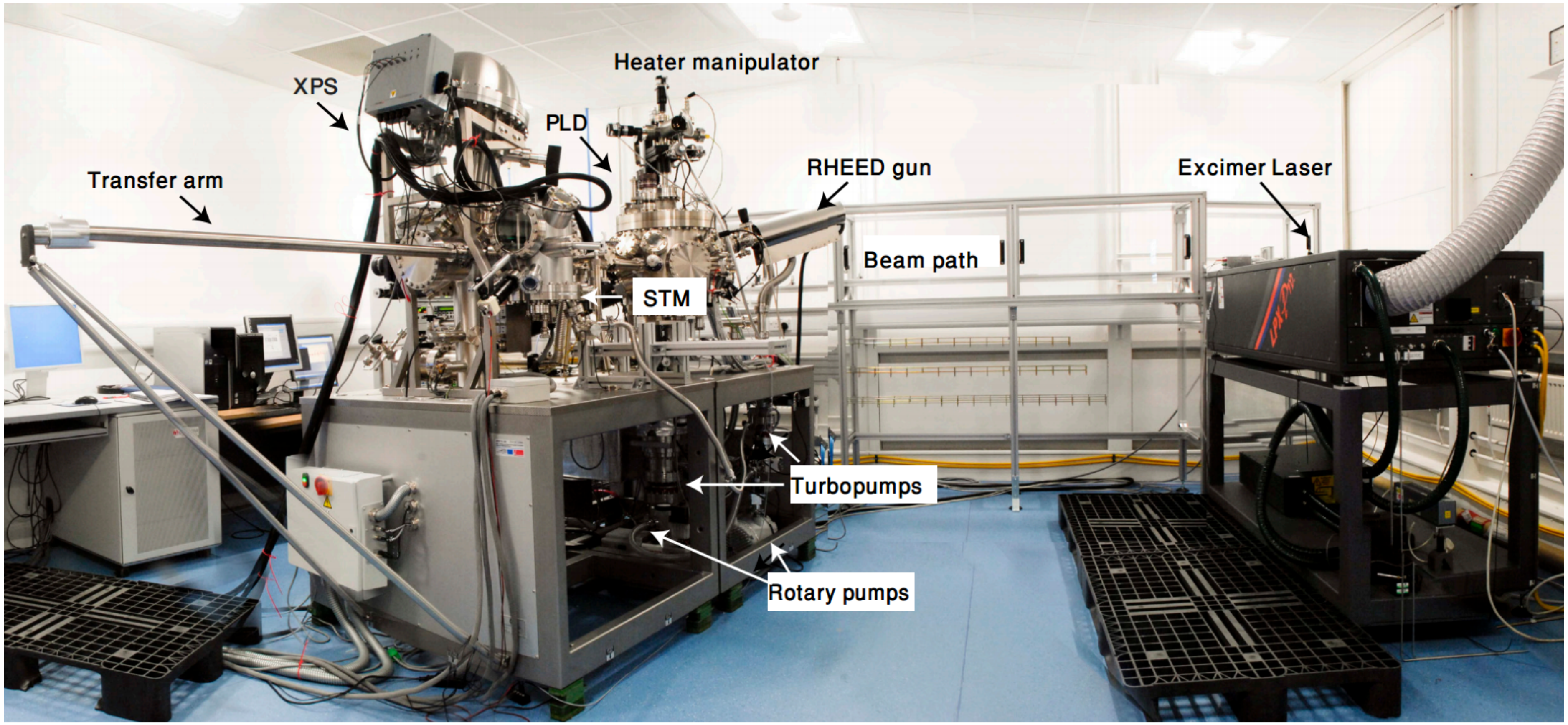

Figure 2.3. *Photo of the PLD-RHEED with XPS-STM laboratory – left part, and On the right hand side is the KrF laser with gas container equipped with sensitive sensors to fluorine gas with extractors to the roof of the laboratory.*

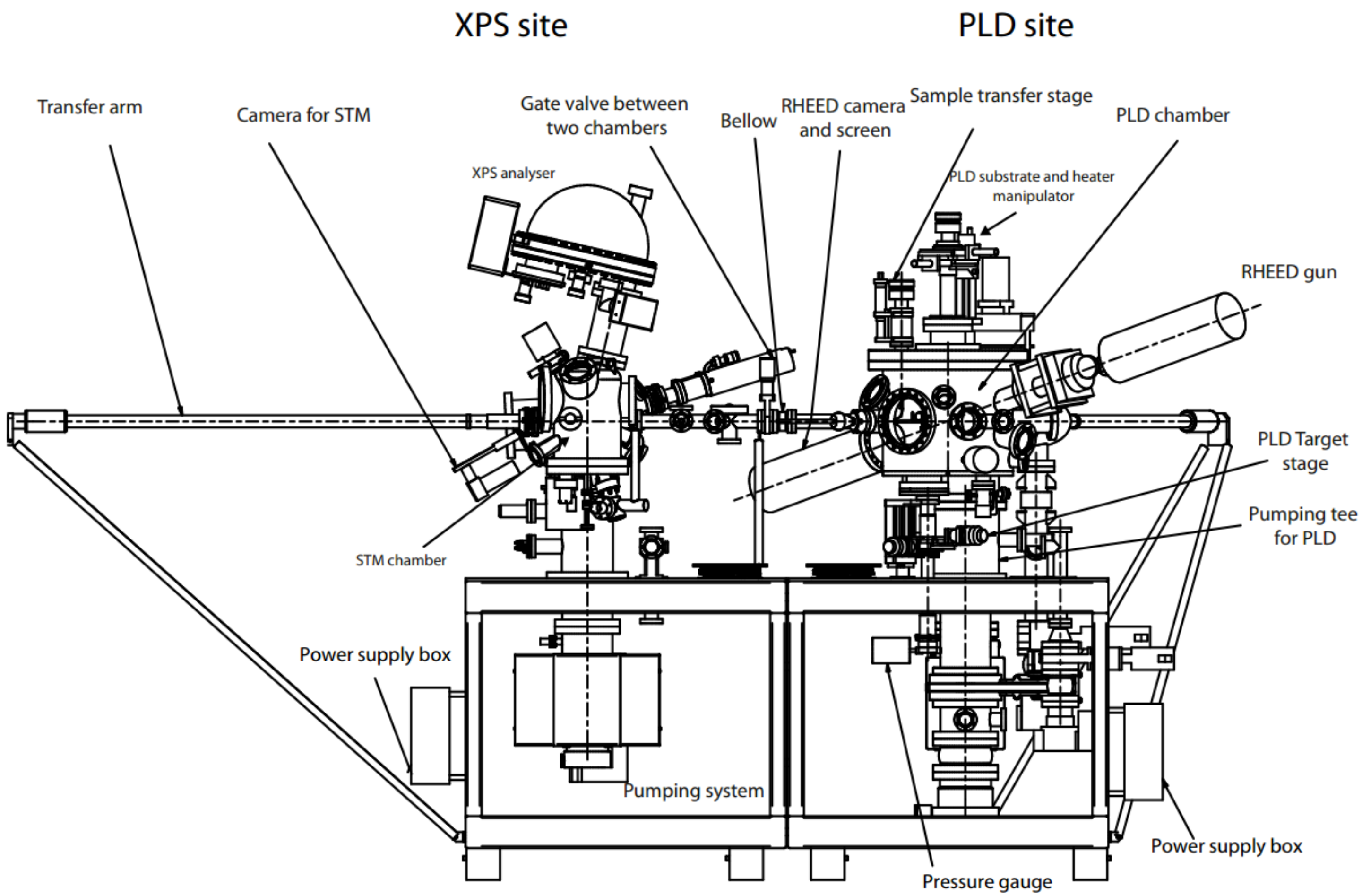

Figure 2.4. *Side view plan of the system showing the vacuum components and two sites of PLD equipped with the RHEED system and XPS site with XPS/STM chamber.*

2.2. Diffraction Methods

2.2.1. Low Energy Electron Diffraction

Low energy electron diffraction (LEED) is one of the most widely used surface science techniques and it is provides mostly information about 2D atomick structure of the sample surface [9, 10]. LEED is a technique which is used as a complementary experiment to check the surface periodicity and orientation before engaging other surface sensitive techniques like STM, AFM ect. LEED can be used quantitatively by

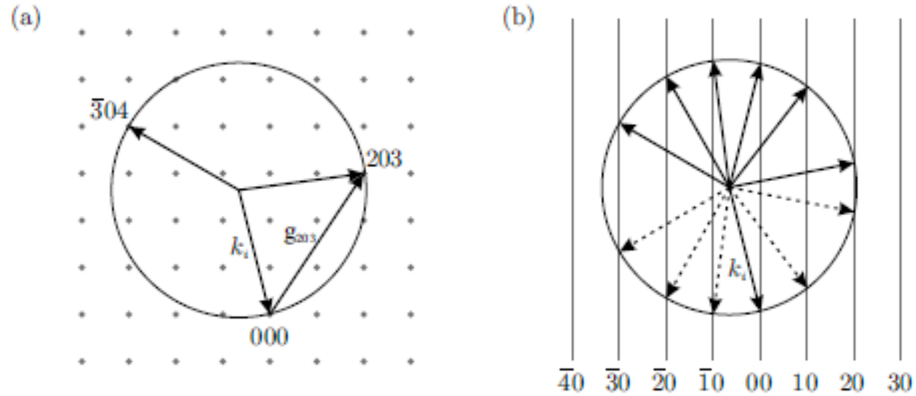

Figure 2.5. *Ewald sphere construction for (a) bulk and (b) surface cases. The incident wavevector is labeled ki, the other vectors indicate possible diffracted wavevectors. For the bulk case the reciprocal lattice vector g_{203} is also shown. For the surface case the dashed vectors indicate wavevectors diffracted into the crystal bulk which are therefore not observable. Adapted from [10].*

measuring the intensity of diffracted beams as a function of beam energy, a technique known as LEED-IV [11, 12]. The surface sensitivity of LEED is due to the short Inelastic Mean Free Path (IMFP) of low energy electrons in solids.

LEED is based on the diffraction of low energy electrons. The de Broglie wavelength of electron given by

$$\lambda = \frac{h}{\sqrt{2mE}};\ \lambda[\text{Å}] = \sqrt{\frac{150}{E(eV)}} \tag{2.2}$$

for a typicall energy range 30-200eV the electron has a wavelength of 1-2 Å, which is compatybile with atomic diffraction condition. Diffraction can be understood in terms of the conservation of energy and momentum and this gives

$$k_2^i = k_2^f, \tag{2.3}$$

$$k_f = k_i + k_{hkl}, \tag{2.4}$$

where $\boldsymbol{k}_i$ and $\boldsymbol{k}_f$ are the incident and final wavevectors respectively, and $\boldsymbol{g}_{hkl}$ is a bulk reciprocal lattice vector. The Ewald construction which is describer by equesions above modified for diffraction on 2D lattice is shown in Figure 2.5.b. Moving from bulk to surface diffraction greatly relaxes these

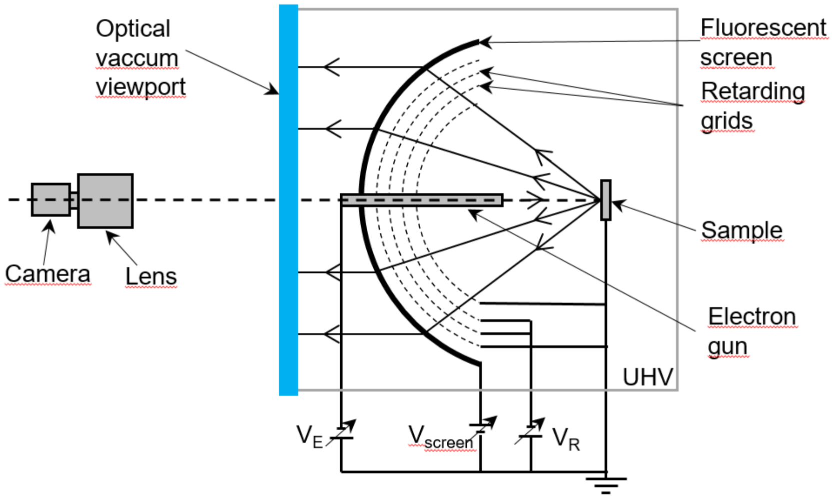

Figure 2.6. *Schematic of a reverse-view LEED optics, with the key components labeled. The electron gun provides an incident beam of electrons at an energy set by (VE). These electrons travel through the field free region, established by grounding both the sample and inner most grid, and diffract from the sample surface. To filter out the inelastically scattered electrons, a retarding voltage (V_R) is applied just below the beam energy. The elastically diffracted electrons are then accelerated into the fluorescent screen, from where they can be imaged using a camera. The optics need to be operated in UHV conditions.*

constraints as $\mathbf{k}\perp$ is no longer conserved, and therefore equation 2.4 becomes

$$\mathbf{k}_f|| = \mathbf{k}_i|| + \mathbf{g}_{hk}, \tag{2.5}$$

and is illustrated by Figure 2.5.b where the reciprocal lattice points have been replaced by reciprocal lattice space.

The standard experimentall set-up is shown in Figure 2.6, where the main elements are shown: the optic consists of a low energy electron guns, a series of grids used to apply potentials, and a phosphor screen. Electron gun have a cathode with Wehnelt cylinder on negative potential. Electrons, which are typically supplied by a heated tungsten or filament, are focused and accelerated towards the sample with a well defined kinetic energy K_E. The sample and the fourth grid and sample is on the earth potential. Thos electrons which will undergo inelastic scattering and will not contribute to the LEED pattern. To help the electrons which were elastically scattered to reach the screen LEED optics have retarding grids. They are working as a high pass energy filter for them. After the retarding grids, a high positive voltage (3 to 7 kV) is applied to the phosphor screen to accelerate the electrons and make the diffraction pattern visible. Two typs of LEED system are in use [29]:

- Normal-view arrangement where a viewport is placed in front of the back side of the sample
- Reverse-view arrangement where the LEED pattern are observed through a viewpoint pleaced behind the transmission phosphorescent screen.

2.2.2. Reflection high-energy electron diffraction

Reflection high-energy electron diffraction (RHEED) is a very powerfull tool in surface science because of the high surface sensitivity. RHEED provides information about the periodic arrangement of the surface atoms as a result of utilizing diffraction of electrons by surface atoms. In addition, RHEED is often used in-situ for the investigation of the surface morphology during thin film growth.
Figure 2.7.1 represents a schematic view of a typical RHEED geometry system.

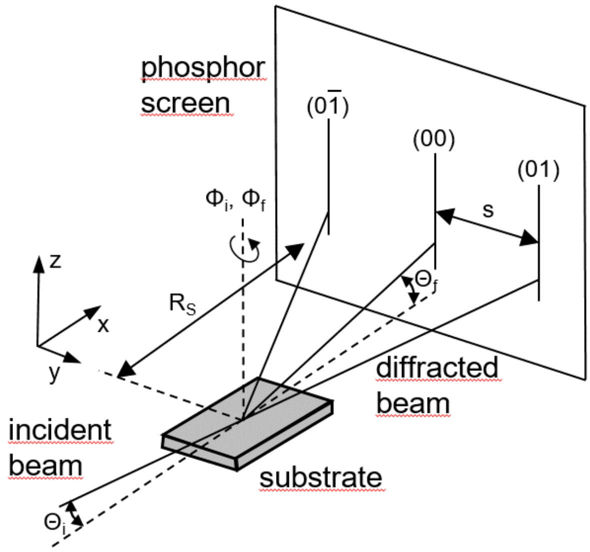

Figure 2.7. *RHEED geometry system: $\theta_I(\theta_F)$ and $\varphi_I(\varphi_F)$ are the incident and azimuthal angles of the incident (diffracted) electron beam. R_S is the distance between substrate and phosphor screen and S the distance between the diffraction spots or streaks.*

The incident electrons (e-beam) are mono-energetic with a typical energy of E ~10-50 keV. They strike the sample surface at a grazing angle θi. For these high-energy electrons, the energy of the wavevector k_0 can be estimated using:

$$\boldsymbol{E} = \sqrt{\frac{\hbar^2 |\boldsymbol{k_0}|^2}{\boldsymbol{m^*}}}, \tag{2.6}$$

where m^* is the effective mass of the electron. Omitting the relativistic correction, the electron wavelength λ can be defined as:

$$\boldsymbol{\lambda}(\text{Å}) = \sqrt{\frac{\mathbf{150.4}}{\boldsymbol{E}}}, \tag{2.7}$$

with E given in eV. Concerning typical energies used in RHEED experiments (eg. 15 -35 keV), the electron wavelength λ is around 0.05 - 0.1 Å. This is an order of magnitude smaller than the thickness of an atomic layer. Typical value of the angle of incidence is between 0.1 and 5°. At such small grazing angles the penetration depth is small, and it makes RHEED one of the most surface sensitive diffraction techniques. The incidence electrons (e-beam) are easily scattered by surface steps and terraces.

The coherence length (CL) [13], defined as the maximum distance between reflected electrons that are able to interfere is typically of the order of several hundred's nanometers. The CL is mainly determined by the the beam convergence and the energy spread of the electrons.

To avoid the interference with the deposition process, the electron gun and phosphor screen (detector) are located far from the sample. At such geometry of the experimental setup, electrons are scattered from the crystal surface, and as a result one can see a characteristic diffraction pattern on the phosphor screen. The RHEED patern is observed continuously during experiment and can be used to define the crystallographic structure or monitor a growth of thin films. The RHEED technique involves strong interaction of electrons with the periodic potential of the crystal surface, and cannot be described quantitatively by the kinematic approach [14]. The kinematic scattering theory is applied to describe weak interacting diffraction techniques (e.g. x-ray or neutron diffraction). However, the kinematic approach can be sucesfully used for the physical understanding and qualitative description of the growth process.

During the experiment can be observe a "spots" as well as rings on the RHEED patterns. For the single crystal sample, many spots are generated as the atom positions are well defined by the symmetry. After measuring the intensities of all of the diffraction spots (reflections), it is generally possible to find the lattice symmetry and spacing but the positions of the atoms in the unit cell (the structure) is still not possible to determinated straightforwardly because of the multiple scattering. Most real samples are polycrystalline then single crystal materials. In the diffraction pattern, the effect is that each of the spots is spread out into a ring (cone) Figure 2.8. If the crystallites are oriented randomly, the rings are uniform.

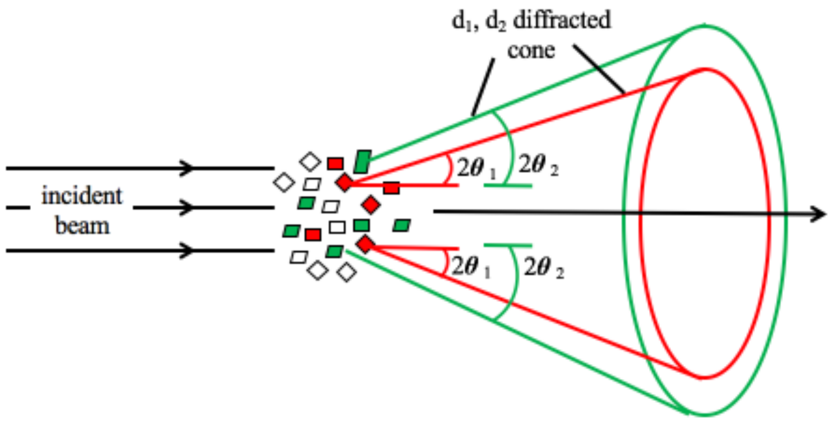

Figure 2.8. *Diffraction cone scheme. Different crystal orientations will produce will produce another cone of diffracted rays illustrated in green and red, and so on for* d_3*,* d_4 *etc.*

2.2.3. X-Ray Diffraction

X-ray diffraction has been a well-established technique for a structural investigations last decades, applied not only by physicists. Any method which used X-rays is based upon their discovery in 1895 by W. C. Röntgen [15]. X-rays show wave nature with wavelength ranging from about 10 to 103 nm.

Figure 2.8 is the construction shown the Bragg's law. The interplanar spacing, d, sets the difference in path length for the ray scattered from the top plane and the ray scattered from the bottom plane. Figure 2.9 shows that this difference in path lengths is described by equation 2.9

$$n\lambda = 2d \sin\theta, \quad (2.9)$$

where n is the product of the diffraction order (n) and the wavelength (λ) is equal to twice the product of the distance between the lattice planes (*d*) and the sine of the diffraction angle (sinθ).

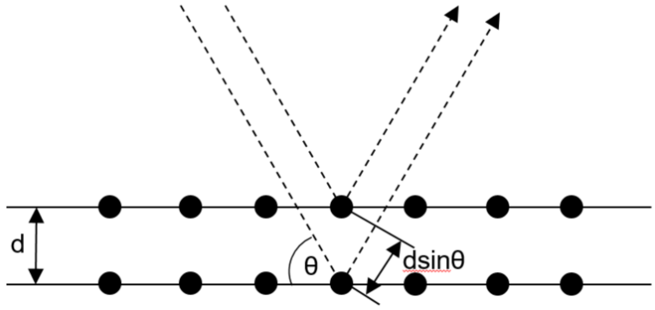

Figure 2.9. *Schematic diagram of how the Bragg equation is derived from a crystal structure.*

The Bragg low also required to remember the following two geometric relationships[16]:

1. The angle between the incident X-ray beam and the normal to the reflection plane is equal to that between the normal and the diffracted X-ray beam. The incident X-ray beam, the plane normal, and the diffracted X-ray beam are always coplanar [16].
2. The angle between the diffracted X-ray beam and the transmitted one is always 2θ, and this angle is called "the diffraction angle [16]".

Crystal structure of TiO_2 were investigated by X-ray diffraction (XRD) using a Philips PANalytical X'Pert Pro MPD diffractometer with Cu Kα filtered radiation with the incident X-rays wavelength of 1.540598 Å. The diffractograms were recorded data using in the 2Θ angular range of 20° to 140°.

2.2.4. X-Ray Reflectivity

X-ray reflectivity (XRR) is a technique often applied to thin film to check the growth quality of the sample. This metod will shown information about a layer thicknesses and interfacial roughness. It should be noted that the reflectivity depends only on the interface properties.

In crystalline material, the electron density ρ is characterized by a certain symmetry. Kiessig firinges depend on the constructive and destructive interference of x rays reflected from the two interfaces as a consequence of the angular-dependent phase shift. Their period is determined by the thickness of the layer [28] and they are very sensivity on the qualities of the interface. From Laue oscillations which depend weakly onsurface roughness but are very sensitive to crystalline disorder we can tell about surfaces quality

2.3. Microcscopy Methods

2.3.1. Scanning Tunneling Microscope [27,30]

The principle of electron tunneling was first published by Giaever in 1960 [16]. The tunneling effect can be observed between two metallic surfaces where the electric potential between them is observed. If the distance between surface and tip is less then 5nm electrons can tunnel between the electrodes.

According to quantum mechanics, a particle with energy E can penetrate a barrier ϕ>E (Figure 2.10).

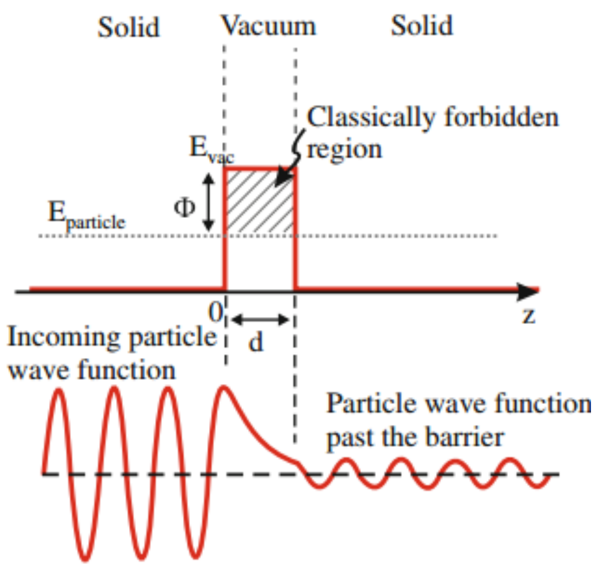

Figure 2.10. *The top graph shows the potential for a solid-vacuum-solid configuration. The lower graph shows the electron wave function oscillating in front of the barrier, exponentially decaying inside the barrier and again oscillating past the barrier [27,30].*

In the classically forbidden region, the wave function ψ decays expotentially

$$\psi(x) = \psi\left(0)exp - \frac{\sqrt{2m(\phi-E)}z}{\hbar}\right) \tag{2.10}$$

Where m is the mass of the particle and $\hbar = 1.05x10^{-34}Js$. Barrier in STM is given by the vaccum gap between sample and tip. Then tunneling current occurs and is exponentially dependent on the surface separation distance and is equal to the

$$I_t \propto V\rho_s(E_F)e^{-1.025\sqrt{\Phi}z} \tag{2.11}$$

This leads to very high vertical resolution.

Binnig and his colleagues [17] have invented the STM technique. In Figure 2.11 is presented a schematic of the STM where the sharp tip is mouted on the piezoelectric transducer. The piezoelectric element is used to move the tip into the surface for the very small distance – only few angstrom units. This small distance means that the wave functions of tip and sample start to overloop and the tunneling process by the barrier is possible. The tunneling current is usually in a range of pA to nA and is measured by the amplifier. For the STM measurements the constant current or constant hight mode can be used. In the constant current mode, the distance between tip and surface is controlled using a feedback loop and the tip is scanned surface with constant voltage and current. The signal from the loop goes directly to the z-piezo element. For each mesurements the feedback parameters need be optimize separtly. The gain of the whole loop depended on the parameters like preamplifier gain or voltage amplifier gain. For ideal electronically homogeneous surface constant current mean constant gap. In this case tip follow all the topography features of the sample. The constant current mode is in reality include ability to determine the surface height quantitatively from V_z direction and the sensivity of the piezo element as the surface is not necessarily atomically flat. The constant hight mode does not use the feedback loop but the tip scans topography of the surface with the constant hight V_z=const. Chang of the tunneling current are recorded directly what gave the possibilities of the much grade speed then in constant current mode. That is usefull for studying real-time dynamic processes measurements. This mode is applicable only for relatively flat surfaces. For more details about STM see [18-25].

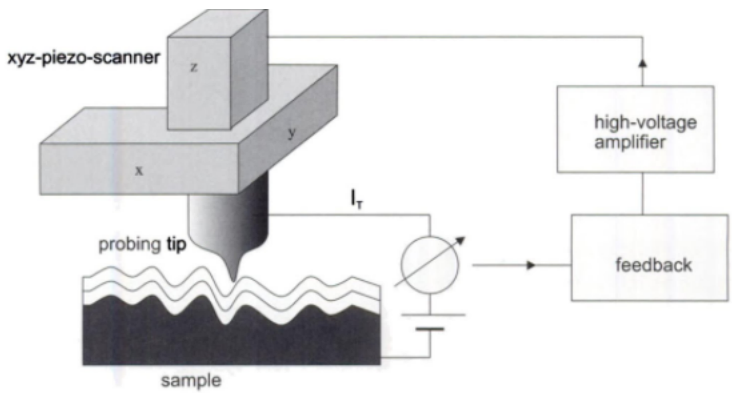

Figure 2.11. *Schematic of the STM. An xyz-piezo scanner move the tip into the sample. The feedback loop cna be used to keep the tunneling current constant [27].*

The STM measurements for teh semiconductors for positive bias, measure tunneling current arise from electrons from the unoccupied states of the tip into unoccupied states of the sample so the STM tip follow contour which is related to the occupited states. For negative bias the electrons tunnel from occupited states of the sample into unoccupied states of the tip. In this case STM image shown contour related to the epty (unoccupied) electronic states.

The main limitation of Scanning Tunneling Microscopy is the necessity of working with conductive materials, which puts strong constrains on possible applications.

2.3.2. Atomic Force Microscopy

By AFM is possible to measure any solid material without the condition of surface conductivity. Such measurements are not possible to do by STM. The concept of AFM is the measurement of force between tip (mounted on the cantilevel) and a surface [17]. Limitations of the force detection is far lower then the force between atoms at lattice distance. AFM can be operated in several modes. The most common is the contact mode (static). In this mode the distance between tip and surface is controlled to maintain a constant cantilevel bending. Topography of the surface is recorded by constant force. With using contact moded is possible to measure at an atomic scale resolution. In the dynamic modes is measurering changes in vibrational properties of cantilevel due the tip-sample interactions. The Tapping mode is a combination of the static and dynamic modes. The oscillating tip only touches the measured surface at maximum deection of the cantilever towards measured surface. In this moment, there is direct mechanical contact with strong repulsive interaction forces between tip and surface. In this work was used tapping mode during the measurements.

2.4. DFT

Density functional theory (DFT) has been the most successful used method in condensed - matter physics in past few decades. This theoretical approach based on Schrödinger equation (equesion 2.12) describe the properties of condensed matter systems.

$$\hat{H}\Psi = E\Psi \qquad (2.12)$$

where Ĥ is the Hamiltonian operator, Ψ the total wavefunction, and E is the total energy of the system, provides a precise quantum-mechanical description of the physical behavior of the universe [35].

The most important adwantage is that not only standard bulk materials can be circumscribe but also complex materials such as molecules, proteins, interfaces and nanoparticles. Description of many - body system interactions are the main idea of DFT with using particle density wavefunction. Following the Born-Oppenheimer approximation [31] for N electrons interacting with static nuclei, the time - independent Hamiltonian neglecting electron spin may be expressed:

$$\hat{H} = -\frac{\hbar^2}{2m}\sum_{i=1}^{N}\nabla_i^2 + \sum_{i=1}^{N}V(r_i) + \sum_{i=1}^{N}\sum_{j<i}U(r_i, r_j) \qquad (2.13)$$

where the three terms define the kinetic energy, the electrons, the interaction of the electrons with the nuclei and the electron-electron interactions respectively.

Two underlying postulates of DFT were published by Pierre Hohenberg and Walter Kohn [32, 33]

The ground - state energy, E_0, from Schrödinger's equation is a unique functional of the electron density.

The electron density that minimises the energy of the overall functional is the true electron density corresponding to the full solution of the Schrödinger equation: $E_0[n] \leq E[n]$ [34, 35].

These postulates nevertheless provide a method to recast the 3N-dimensional Schrödinger equation to three spatial variables coordinates which makes calculations possible in real time.

2.5. CASTEP

The Cambridge Serial Total Energy Package (CASTEP) [36], written in FORTRAN90, is a DFT package created by Prof M. C. Payne. CASTEP is a program based on quantum mechanics, designed specifically for solid-state materials. The program involves the density functional theory plane - wave pseudopotential method, which allowes calculations that explore the properties of materials. Many of the results have been analysed using either Accelrys Materials Studio [37]. CASTEP allows to perform calculations in severals different tasks like: energy calculation, geometry optimization, molecular dynamics, transition state calculations and properties. Each calculation can have specified properties.

The geometry optimisation must be performed in order to determine the precise local minimum energy structure for a collection of atoms. The most common optimization approach is Broyden, Fletcher, Goldfarb and Shanno (BFGS) [33]. For bulk optimization the unit cell must be optimized like an internal structure. It is important to change the size of the Brillouin zone when the cell size is changed. Not accurate and not well - optimised calculations will affect the procces and will casue a systematic error which will appear in the calculation of the total energy and stress. The cell optimization is finished when the maximum stress component drops belowe a tolerance [34].

The classification of adsorption can be de divided into two classes. A week adsorbate - substrate interaction where the adsorption energy is less then 0.3 eV per atom is called physisorption, and when an adsorption energy is larger then 0.3 eV and where a chemical bond exist is a so-called chemisorption.

The adsorption energy per atom is different from the total energy of adsorbate. The total energy is called the potential - energy surface. This surface helps to find the global minimum for energy. This minimum of energy corresponds to the most stable configuration. The adsorption energy is described by:

$$E_{ads} = \frac{E_{cr+ads} - (E_{cr} + N_{ads} E_{ads})}{N_{ads}} \tag{2.14}$$

where E_{cr+ads} and E_{cr} are the total energies of a crystal with and without the adsorbed species present, N_{ads} is the number of adsorbed species and E_{ads} is the total energy of the species to be adsorbed, in its stable isolated conformation. Energy adsorption calculations are performed to find the most stable and favourable structure.

The easiest way to calculate surface energies is presented in this equation;

$$\gamma = \frac{E_{cr} - N_{cr} E_b}{A} \tag{2.15}$$

where E_b is the total energy associated with a single atom in the bulk and A is the total surface area of the crystal. It is very important to know that using n-single atom energies E_b will be less accurate in absolute terms then using a bulk slab total energy. Results present in chapter 4 are made by using n-sibgle atom energies approach but the relative energies are correct and do not change the results interpretation, which means that surface free energy can thus be used as a relative stability of surface structures. The energies should be compared at the same cutoff energies. In addition, atom adsorption at a stable site reduces the surface free energy [34, 35].

The work function W is the minimum energy required to remove an electron from a solid to the vaccum. It is defined as a depth of Fermi level seen from the vacuum energy, expressed as

$$W = -\Phi(V_{ac}) - E_F \tag{2.16}$$

where both Fermi energy E_F and $\Phi(V_{ac})$, the electrostatic potential at the lowest level inside the supercell. Work function depends on the orientation of the crystal and for different crystallography orientation surface, work function will be different and will be between 2 to 6 eV. Structure preparation for work function calculation is describe at CASTEP guide [38]. Figure 2.12 shows work function plot for $Pt_3Ti(111)$ surfaces.

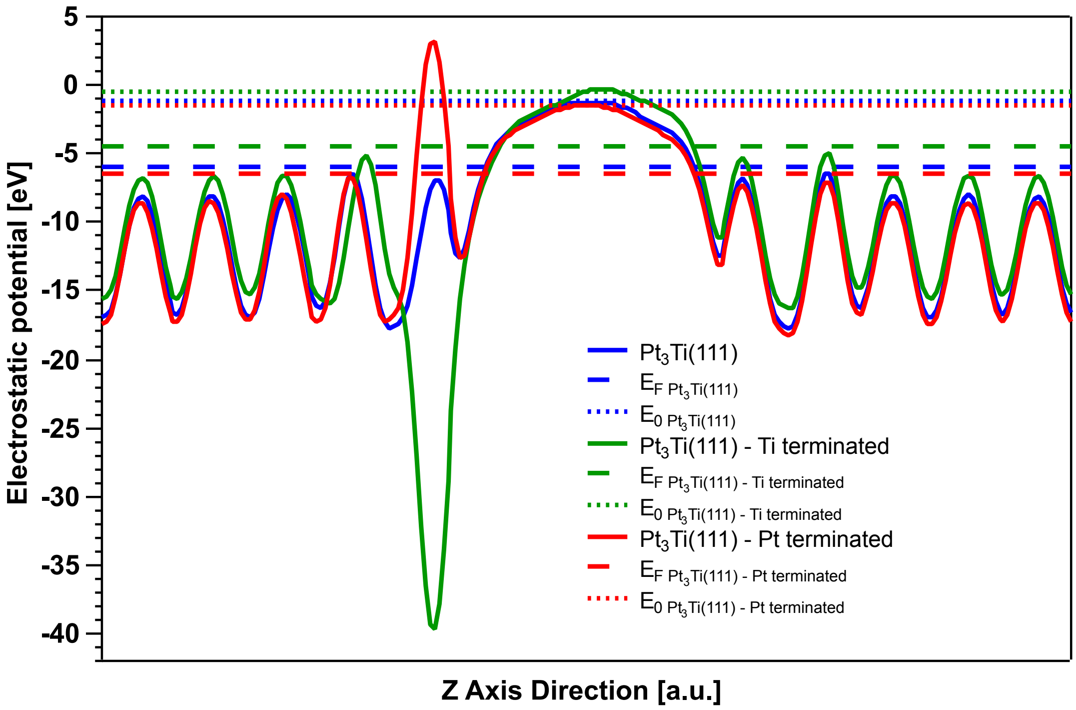

Figure 2.12. *General electrostatic potential profile for the clean Pt_3Ti, Ti and Pt terminated surface in average on yz-plane.*

References

[1] P.R. Willmott, J. R. Huber. Reviews of Modern Physics, **72** (2000) 315.

[2] G.J.H.M. Rijnders. The Initial Growth of Complex Oxides: Study and Manipulation. PhD thesis, University of T wente, 2001.

[3] M. Ohring. Material Science of Thin Films. Academic Press, 2nd edition, 2002.

[4] C.B. Samantaray , H. Sim, H. Hwang. Microelectronics Journal, **36** (2005) 725.

[5] CRC Handbook of Chemistry and Physics. CRC Press, 76th edition, 1996.

[6] J.F.Ready, Applied Physics Letters, **3** (1963) 11.

[7] R. Timm, P.R. Willmott, J.R. Huber, Journal of Applied Physics, **80** (1996) 1794.

[8] S. Proyer and E. Stangl. Applied Physics A, **60** (1995) 580.

[9] J.C. Vickerman, I. Gilmore, *Surface Analysis: The Principal Techniques* (Wiley, 2009).

[10] D. P. Woodruff, T. A. Delchar, *Modern Techniques of Surface Science* (Cambridge University Press, 1994).

[11] M.A. Van Hove, W.H. Weinberg, C.M. Chan, *Low-Energy Electron Diffraction: Experiment, Theory and Surface Structure Determination*, Springer Series in Surface Sciences (Springer London, Limited, 2011).

[12] J.B. Pendry, *Low Energy Electron Diffraction: The Theory and its Application to Determination of Surface Structure*, Techniques of Physics Series (Academic Press, 1974).

[13] M.G. Lagally, D.E. Savage, M.C. Tringides in *Reflection high energy electron diffraction and reflection electron imaging of surfaces*, P.K. Larsen and P.J. Dobson Eds. (Plenum Press, London, 1989), pp. 139–174 [14] T. Kawamura in *Reflection high energy electron diffraction and reflection electron imaging of surfaces*, P.K. Larsen and P.J. Dobson Eds. (Plenum Press, London, 1989), pp. 501-522

[15].H.J.W. Dam, McClure's Magazine, **6** (1896) 5.

[16] G. Binning, H. Rohrer, Helv. Phys. Acta **55** (1982) 726.

[17] G. Binnig, H. Rohrer, Ch. Gerber, Phys. Rev. Lett. **50** (1983) 120.

[18] D. Sarid, V. Elings, J. Vac. Sci. Technol. B, vol. **9** (1991) 431.

[19] P.K. Hansma, J. Tersoff, J. Appl. Phys. **61** (1987) R1.

[20] G. Binning, H. Rohrer, C. Gerber, E. Weibel, Phys. Rev. Lett., **49** (1982) 57 1982.

[21] U. Durig, J. Gimzewski, D.W. Pohl, Phys. Rev. Lett., **57** (1986) 2403.

[22] I. Giaever, Phys. Rev. Lett., **5** (1960) 147.

[23] R. Young, J.Ward, F. Scire, Phys.. Rev. Lett. **27** (1971) 922.

[24] R. Young, J. Ward, F. Scire, Rev. Sci. Instr. **43** (1982) 178.

[25] G. Binnig, H.Rohrer, Ch. Gerber, E. Weibel, Appl. Phys. Lett. **40** (1983) 178.

[26] R. Garcia, R. Perez, Surface Science Reports **47** (2002) 197.

[27] E. Meyer, H.J. Hug, R. Bennewitz "Scanning Probe Microscopy. The Lab on a Tip" Springer, ISSN 1439-2674, 2004.

[28] Y. Waseda. E. Matsubara, K. Shinoda "X-Ray diffraction crystallography. Introduction, examples andSolved Problems" Springer, ISBN 978-3-642-16635-8, 2011.

[29] K. Oura, V.G.Lifshits, A.A.Saranin, A.V.Zotov, M. Katayama, "Surface Science. An Introduction", Springer, ISSN 1439-2674, 2003

[30] Bert Voigtländer, „Scanning Probe Microscopy Atomic Force Microscopy and Scanning Tunneling Microscopy." ISSN 1434-4904, 2015

[31] M. Born, J. R. Oppenheimer, Annalen der Physik, **389** (1927) 457.

[32] W. Kohn, L.J. Sham, Phys. Rev., **140** (1965) A1133.

[33] P. Hohenberg, W. Kohn, Phys. Rev., **136** (1964) B864.

[34] Bradley, M. K. (Matthew K.) (2012) „*Density functional theory investigations of surface structure and surface stress in adsorbate layers on Cu, Pd and Ir surfaces.*" PhD thesis, University of Warwick.

[35] D. S. Sholl, J. A. Steckel, Density functional theory: A practical introduction, Wiley, 2009.

[36] S. J. Clark, M. D. Segall, C. J. Pickard, P. J. Hasnip, M. J. Probert, K. Refson, M. C. Payne, Zeitschrift fur Kristallographie, **220** (2005) 567.

[37] Accelrys Inc., San Diego, USA, http://accelrys.com/products/materialsstudio/

[38] "CASTEP guide Material Studio 8.0, BIOVIA Support 5005 Wateridge Vista Drive, San Diego, CA 92121 USA, 2014.

Chapter 3

Growth Optimization of TiO_2

3.1. Introduction

Thin films of TiO_2 can be formed on a wide variety of substrates including oxide surfaces such as: MgO [1], $SrTiO_3$ [1-2], and $LaAlO_3$ [1-3]. Different deposition methods such as reactive sputter deposition [4], oxygen plasma assisted molecular beam epitaxy (PAMBE) [2,5] or pulsed laser deposition (PLD) [3,6-12] have all been used to fabricate the anatase phase. Until now of the substrates examined, $LaAlO_3$ (LAO) gives the best coherency owing to its relatively small lattice mismatch with anatase. In the bulk phase, anatase TiO_2 has a tetragonal structure with lattice parameters a = 0.3776 nm and c = 0.9486 nm, while $LaAlO_3$ can be described as a pseudo-cubic perovskite with a lattice parameter a = 0.3792 nm, leading to a mismatch of only 0.4% when TiO_2 is grown epitaxially on the (001) surface of $LaAlO_3$ [13]. While most studies have focused on the bulk structure of the anatase films, studies have also investigated optimization of film growth to obtain good surface properties of anatase TiO_2(001), i.e. atomically smooth terraces with well-defined monoatomic step-structures. In oxygen plasma-assisted MBE, well defined surface structures were obtained for low growth rates (0.003–0.011 nm/s) at growth temperatures between 550 and 650 °C [14]. Under these conditions, a characteristic (4×1) reconstruction of the anatase TiO_2(001) surface [15-17] was observed in both reflection high-energy electron diffraction and low-energy electron diffraction measurements [18-19]. In one such study using low-energy ion emission [18], it was proposed that this reconstruction is based on (103) nano-facets of TiO_2, but later theoretical calculations of the surface energy for a range of surface orientations concluded that the (103) face is a high energy surface, and therefore rather unlikely [20].

The aim of the present study is the optimisation of the PLD growth parameters to generate smooth, flat surfaces and a well-defined interface between film and substrate. Bulk and surface characterization of the anatase-TiO_2(001)-(4×1) films on

$LaAlO_3(001)$ using RHEED, LEED, X-ray diffraction, atomic force microscopy (AFM), scanning tunnelling microscopy (STM), and scanning transmission electron microscopy (STEM).

3.2. Experimental Details

The thin films were prepared by pulsed laser deposition in an ultra-high vacuum (UHV) system with a base pressure 2×10^{-9} mbar, equipped with high-pressure RHEED and using a 248 nm KrF laser (Coherent, USA). TiO_2 ablation targets were made of anatase TiO_2 powder with 99.99% purity and mounted on a rotating carousel. During deposition, high purity oxygen was supplied to a pressure of 5.4×10^{-9} mbar, while the sample to target distance was around 4.7 cm. For the growth of anatase-$TiO_2(001)$ thin films, $LaAlO_3(001)$ substrates were used (Pi-KEM Ltd). The standard substrate preparation method involved ultrasonic cleaning, first in acetone and next in ethanol for 10 min each. Substrates were mounted side-by-side on tantalum plates and placed into the UHV deposition chamber through a load-lock. All substrates were pre-annealed immediately before growth at the deposition temperature in an oxygen atmosphere of 5.4×10^{-9} mbar for one hour. The structure of the as-grown films was evaluated in-situ by RHEED during and immediately following deposition, and ex-situ with X-ray diffraction (45eV, 40mA, X'Pret PANalytical). All XRD scans were performed between 20° and 120° with the step of 0.02°. The surface topography of the deposited films was studied in-air using AFM in non-contact mode. The LEED and STM measurements were carried out at room temperature in the second stainless steel ultra-high vacuum chamber with a base pressure of 5.0×10^{-11} mbar. $TiO_2/LaAlO_3(001)$ samples were transferred between PLD/RHEED and LEED/STM chambers without breaking UHV conditions with the use UHV suitcase. All STM measurements were performed with the use of electrochemically etched W (99.99%) tips (diameter 0.5 mm, length 3.5 mm) [21]. All STM images were recorded in constant current mode and processed by the WSXM image-processing software [22]. The electron transparent specimen was prepared using conventional cross-section sample preparation methodology. The material was back-thinned to approximately 100 μm before cleaved and mounted on a support grid. Afterwards it was mechanically thinned to approximately 20 μm and ion-milled to electron transparency using Ar^+ ions at 6 kV and a beam incidence angle of 3° (cooled). A final low-energy 'clean' of the sample at 2 kV was employed to minimize amorphous surface layers. The Annular Dark Field images were recorded using a double CEOS aberration-corrected Jeol ARM-200F operation at 200kV. A convergence semi-angle of 22 mrad was used with a JEOL ADF detector with inner and outer collection semi-angle of 45 and 180 mrad, respectively.

3.3. Results and Discussion

In order to evaluate the quality of the anatase thin film grown by PLD, a variety of different parameters were varied including: sample temperature; KrF laser energy and fluence; pulse frequency; and the sample-target distance (see Table 3.1). It was found that epitaxial anatase-TiO_2 thin film growth was observed for substrate temperatures between 620 and 700°C, and for oxygen partial pressures of $10^{-5} \leq p_{O2} \leq 10^{-2}$ mbar. Figure 3.1. demonstrates the quality of the anatase-TiO_2 thin films using in-situ RHEED, AFM, and XRD. The X-ray diffraction and high resolution X-ray diffraction (HRXRD) data were taken along the surface normal and rocking curve data experiments, respectively. The thicknesses of the TiO_2 films ranged from 7.64 nm to 100.26 nm as estimated by using rocking curves, X-ray reflectivity (XRR) and STEM methods, respectively (Table 3.1). The RHEED pattern in Figure 3.1.(a) for the KrF laser energy = 43 mJ shows three weak additional streaks between the primary (intensity) spots on the 0^{th} Laue circle. The diffraction spots become streakier, possible indicating a roughening of the surface and some kind of heterogeneous growth mode which often occurs in oxide films. That is consistent with the AFM data, Figure 3.1, where 3D TiO_2 clusters are observed (marked by arrows) as a result of the possible initial miss-matched growth of TiO_2 on the $LaAlO_3(001)$ substrate. The TiO_2 surface roughness in this case is equal to 1.65 nm. XRD scan shows two well defined peaks at 39.23° for (004) and 82.45° for (008) corresponding to the anatase phase. No fringe maxima were observed in HRXRD. In Figure 3.2 results for changed distance between sample and target are presented, Table 3.1. The RHEED pattern shows brighter than for the previous sample three additional streaks and diffraction spots corresponding to 3D clusters (observed in AFM). These diffraction spots can be visible

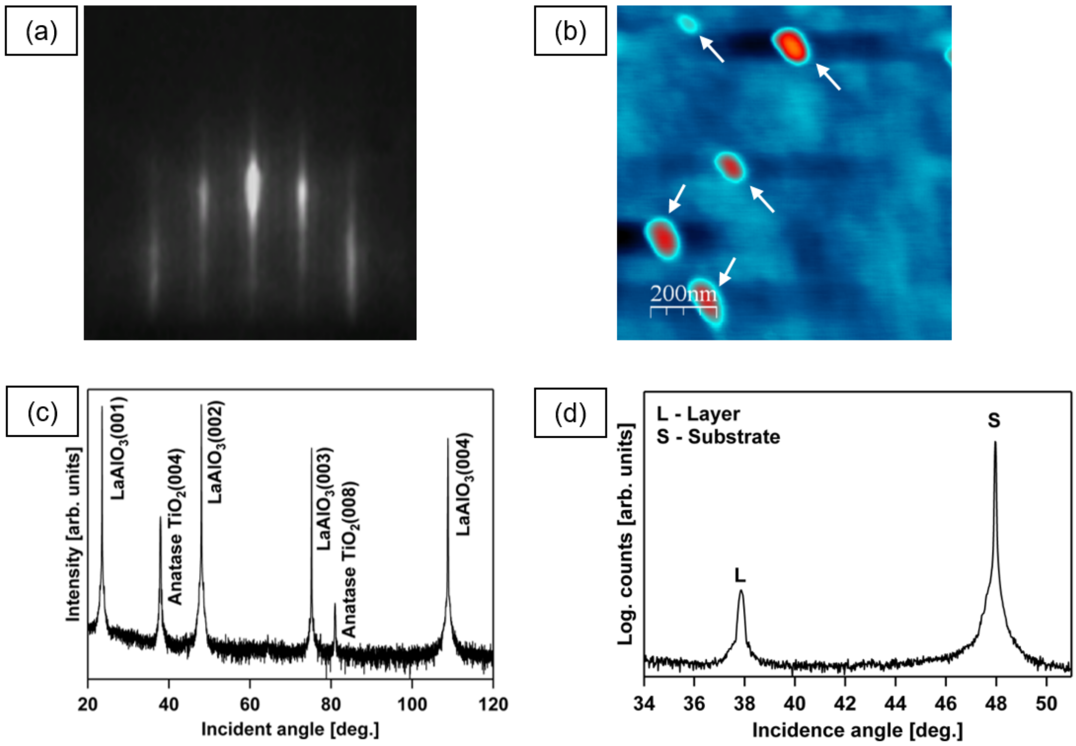

Figure 3.1. *Sample A – different laser energy. RHEED (a), AFM (b), XRD (c) and HRXRD (d) results of TiO_2 on $LaAlO_3(001)$.*

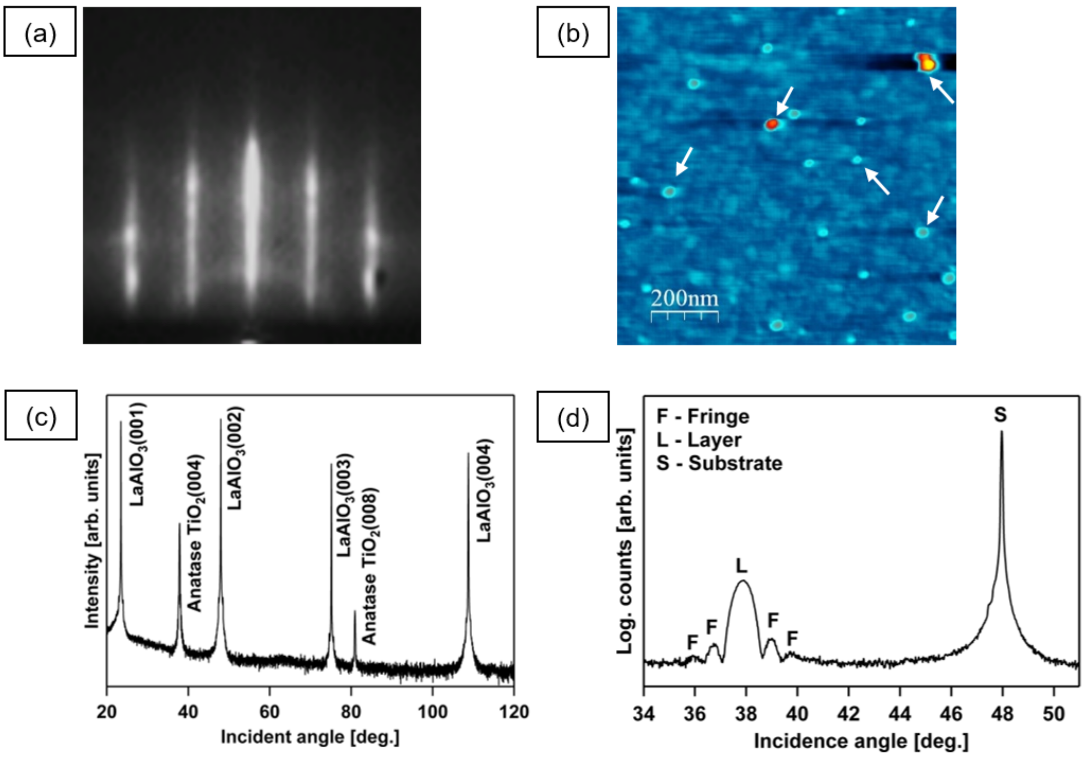

Figure 3.2. *Sample B – different sample-target distance. RHEED (a), AFM (b), XRD (c) and HRXRD (d) results of TiO_2 on $LaAlO_3(001)$.*

Sample	Sample Temperature [^{o}C]	Oxygen Pressure during annealing [mbar]	Laser Energy [mJ]	Laser Pulse Frequency [Hz]	Sample – Target Distance [mm]	TiO_2 Layer Thickness [nm]			TiO_2 Layer Roughness from AFM [nm]
						HRXRD	XRR	TEM	
A	680	5×10^{-4}	43	5	47	-	66.90	60.50	1.65
B	680	5×10^{-4}	44	5	57	9.00 ±0.70	8.80	10.70	0.72
C	680	1×10^{-1}	44	5	47	-	31.43	-	9.00
D	670	5×10^{-4}	44	5	47	-	46.92	47.60	3.40
E	690	5×10^{-4}	44	5	47	-	100.26	-	9.30
F	680	5×10^{-4}	44	8	47	-	7.64	-	7.20
G	680	5×10^{-4}	44	5	47	19.60 ±0.20	19.39	20.5	0.43

Table 3.1. *Growth parameters of TiO_2 thin films on $LaAlO_3$(001) surface.*

because the sample thickness is around 9.5 nm (Table 3.1), and it is possible that the bulk lattice parameters of substrate and film influence to the specular RHEED intensity. Figure 3.3 presents results of a sample which was annealed before growing

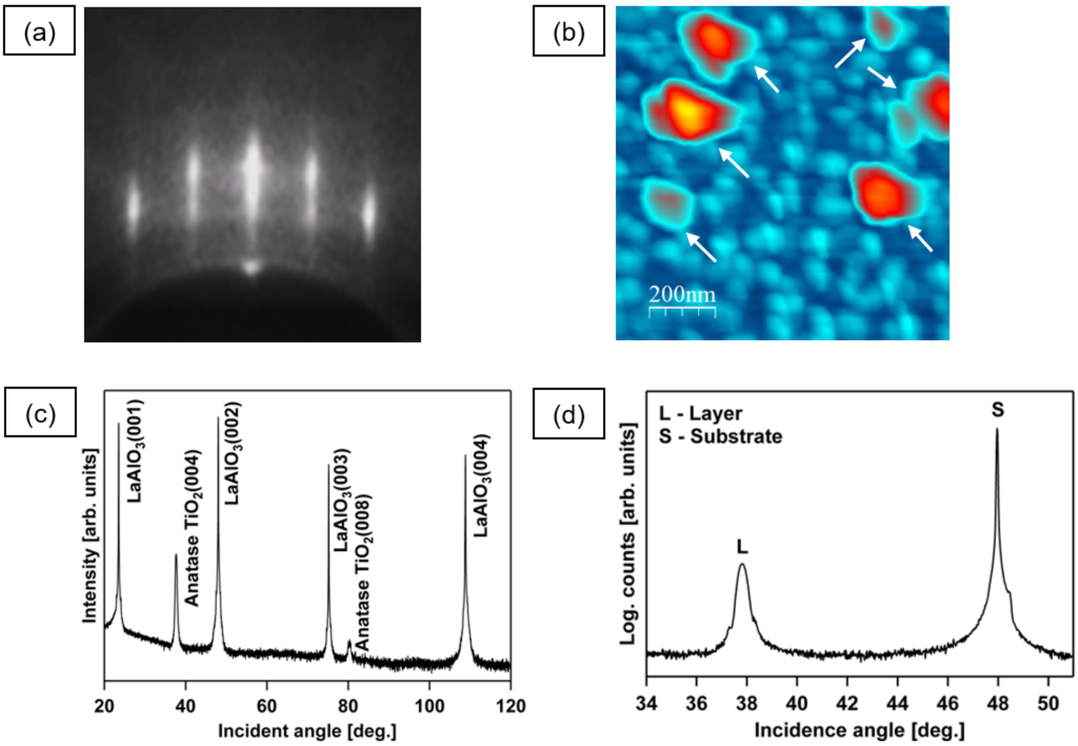

Figure 3.3. *Sample C – oxygen pressure changed during sample annealing. RHEED (a), AFM (b), XRD (c) and HRXRD (d) results of TiO_2 on $LaAlO_3(001)$.*

for different oxygen pressure = 0.1 mbar. RHEED reflection shows very weak streaks suggesting that the surface is mostly covered by an amorphous TiO_2 phase. Polycrystalline rings start to become visible in RHEED. However, distinct spots are still visible on some of the rings, which suggest that the growth of TiO_2 is not completely random. In that case, the largest 3D TiO_2 clusters were observed by AFM. Additional peak which is visible on the substrate peak is the results of not right and proper system alignment. The sample shown in Figure 3.4 was prepared with a substrate temperature of T = 670°C and further 3D islands were observed. However, the streaks in the RHEED are the weakest, which means that more of the surface is covered by the amorphous TiO_2 phase. Figure 3.5 shows a completely amorphous film with the 3D clusters grown on

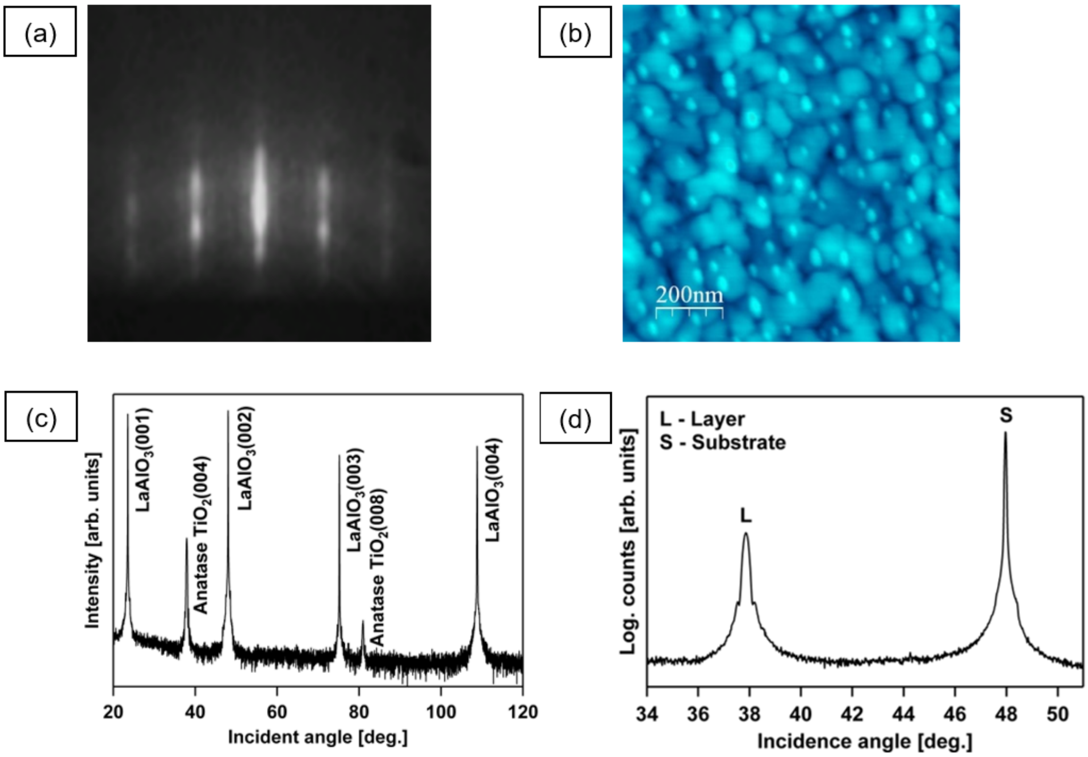

Figure 3.4. *Sample D – sample temperature during growth T = 670 °C. RHEED (a), AFM (b), XRD (c) and HRXRD (d) results of TiO_2 on $LaAlO_3(001)$.*

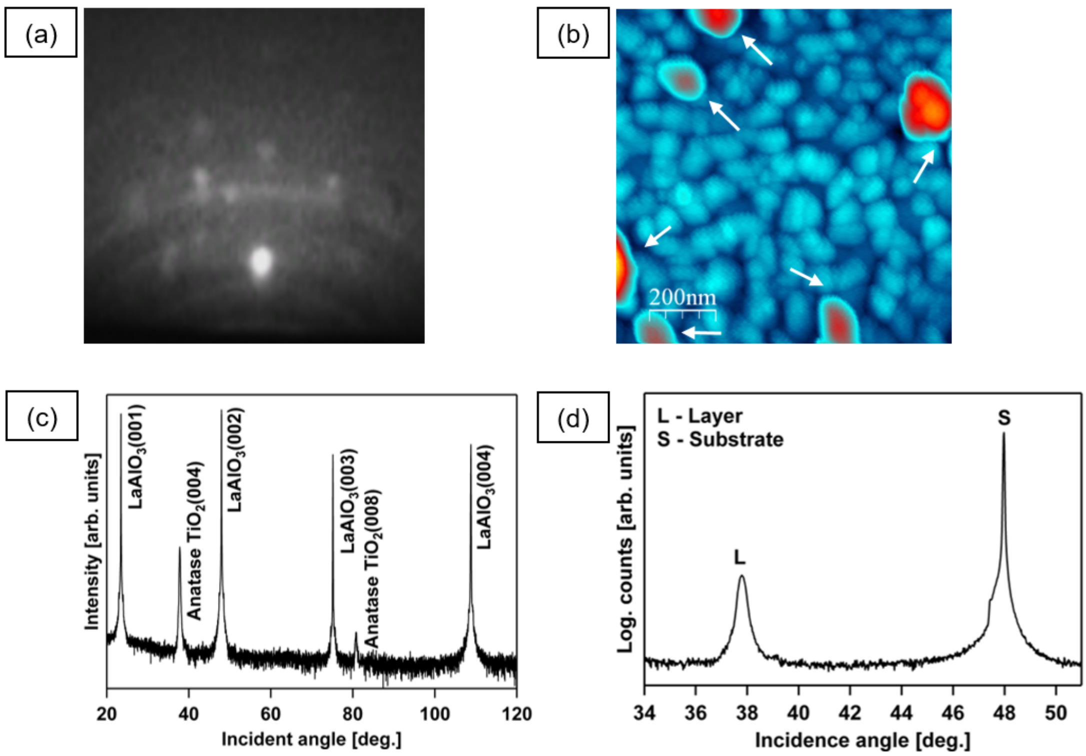

Figure 3.5. *Sample E – sample temperature during growth T = 690 °C. RHEED (a), AFM (b), XRD (c) and HRXRD (d) results of TiO_2 on $LaAlO_3(001)$.*

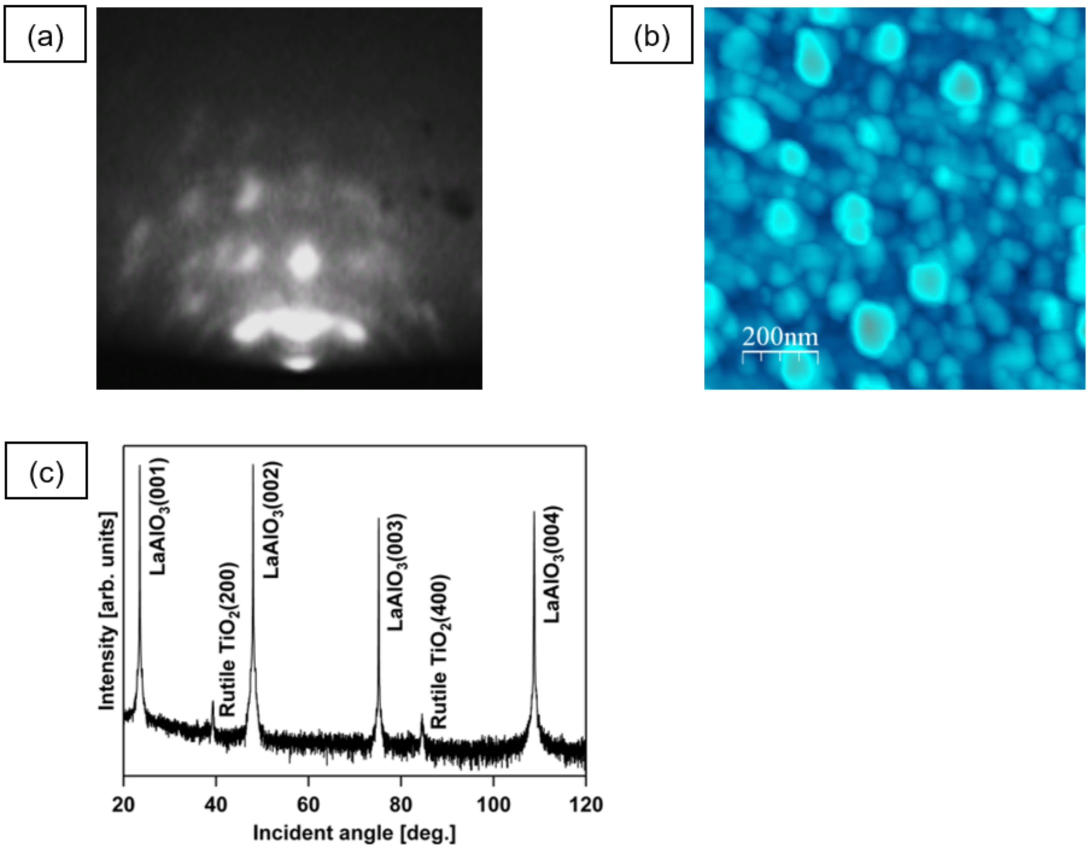

Figure 3.6. *Sample F – different laser pulse frequency. RHEED (a), AFM (b) and XRD (c) results of* TiO_2 *on* $LaAlO_3(001)$*.*

top. The measured film thickness and surface roughness were equal to 100.3 nm and 9.3 nm, respectively. In Figure 3.6 results of TiO_2 growth with a laser pulse frequency 8 Hz are shown. The XRD 2θ-θ scan shows no anatase peaks but instead two rutile peaks (200) and (400) at 39.18° and 84.26°, respectively. The best anatase-TiO_2(001)-(4×1) film on $LaAlO_3$(001) substrate with flat surface and well defined interface between film and substrate was obtained for sample temperature T = 680°C, oxygen pressure $p_{O2} = 5.0\times10^{-4}$ mbar, laser energy 44 mJ, laser pulse frequency 5 Hz, and sample target distance 47 mm (Figure 3.7 – Figure 3.10, Table 3.1- sample g). Figure 3.7.(a) shows a RHEED pattern of the anatase-TiO_2(001)-(4×1) surface taken along [100] azimuthal direction. The streakiness of the pattern suggests that the film surface is now well ordered and flat. Aside from the primary 1× RHEED diffraction pattern, weak 4× diffraction features consisting of three additional streaks within each 1× structure were also visible, suggesting that a 4× reconstruction occurred along [010] direction during the growth. The additional 1/4-order peaks in Fig. 3.7.(c) are

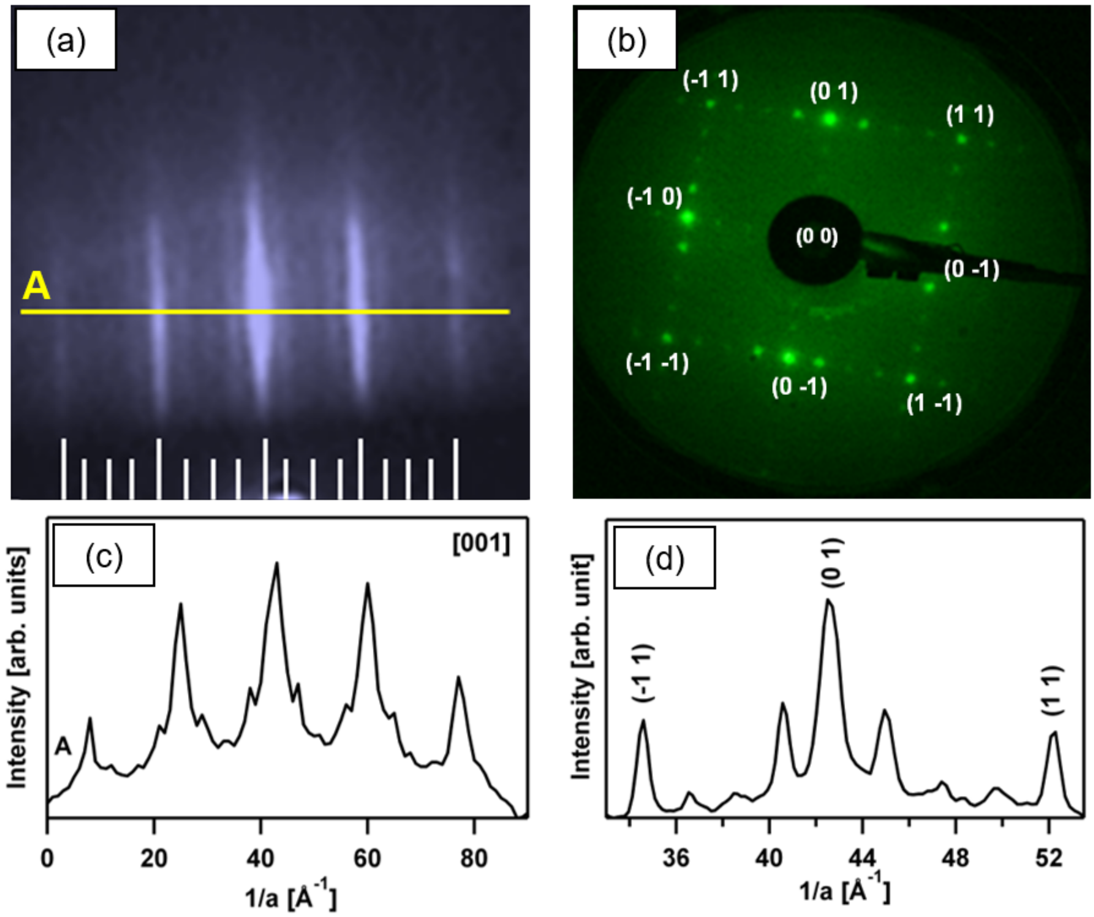

Figure 3.7. *Anatase TiO_2 on $LaAlO_3(001)$ - Sample G. (a) The RHEED pattern along [100] direction. In addition to the 1× diffraction features, a weak 4× diffraction pattern consisting of three additional lines within the 1× pattern are visible; (b) LEED patterns of a two-domain (4×1) reconstructed surface recorded at normal electron incidence for E = 90 eV, and T = 300 K; (c) profile along the line A in the RHEED (a) showing equally spaced 1/4-order peaks between the fundamental peaks; (d) line profile from LEED pattern along (-1 1) – (1 1) direction with maxima from the (1×4) and (4×1) reconstructions.*

symmetrically positioned, showing equal distances between each other and the fundamentals. Further, LEED was used to examine the anatase-TiO_2(001)-(4×1), Fig. 3.7.(b). A two domain structure, concerning of (1×4) and (4×1) of TiO_2 is clearly evident. The profile in Fig. 3.7.(d) represents the intensity of spots along (-1 1) – (1 1) direction with clearly visible maxima corresponding to (1×4) and (4×1) reconstruction. Similar TiO_2 reconstruction was observed on $SrTiO_3$ substrate [18, 23]. The XRD 2θ-θ scan in Figure 3.8 shows well defined sharp anatase (00*l*) peaks, indicating that a pure anatase film is formed, and that the film is preferentially aligned. The full width at half maximum (FWHM) of the (004) anatase peak rocking curve, Figure 3.9, is

0.34° while that of anatase film fabricated on $SrTiO_3(001)$ substrates is larger than 0.6° [24]. Thus the effect of lattice mismatch is

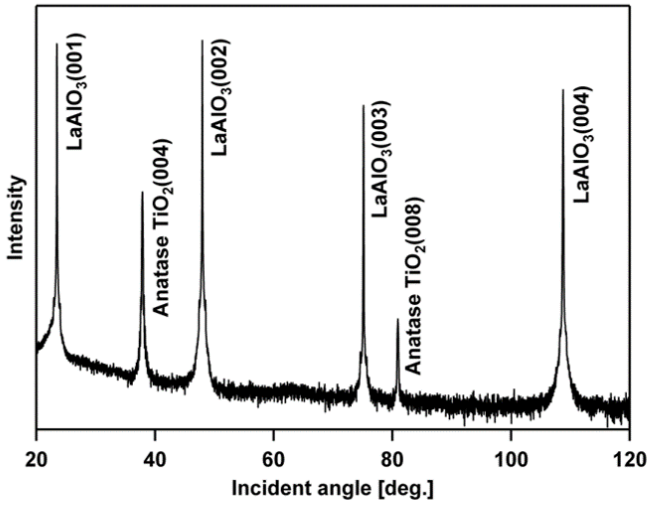

Figure 3.8. *The 2θ-θ scan for Sample G from anatase TiO_2 on $LaAlO_3(001)$.*

clearly reflected in the crystal quality. The difference between growth conditions for the sample in Figure 3.2 and the best grown sample in Figure 3.9 from rocking curve experiment has shown that in case of sample "Figure 3.2" FWHM = 0.57° and for sample "Figure 3.9" 0.34° as was reported above. Those differences could suggest that

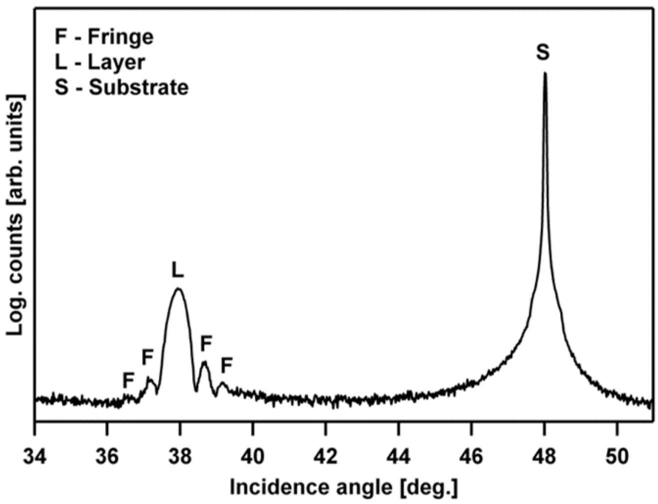

Figure 3.9. *The rocking curve scan for Sample G from anatase TiO_2 on $LaAlO_3(001)$.*

the anatase film in Figure 3.2 has some kind of microstrine. Only a near perfect crystal structure would produce very sharp peaks observed when the crystal is perfectly tilted. In addition, a decrease of the period of oscillation in the fringes diffraction intensity correlated with the film thickness increase was observed. The measured surface roughness from AFM image, Figure 3.10.(a), was found to be 0.43 nm. Hence, the TiO_2 film seems to uniformly cover the substrate.

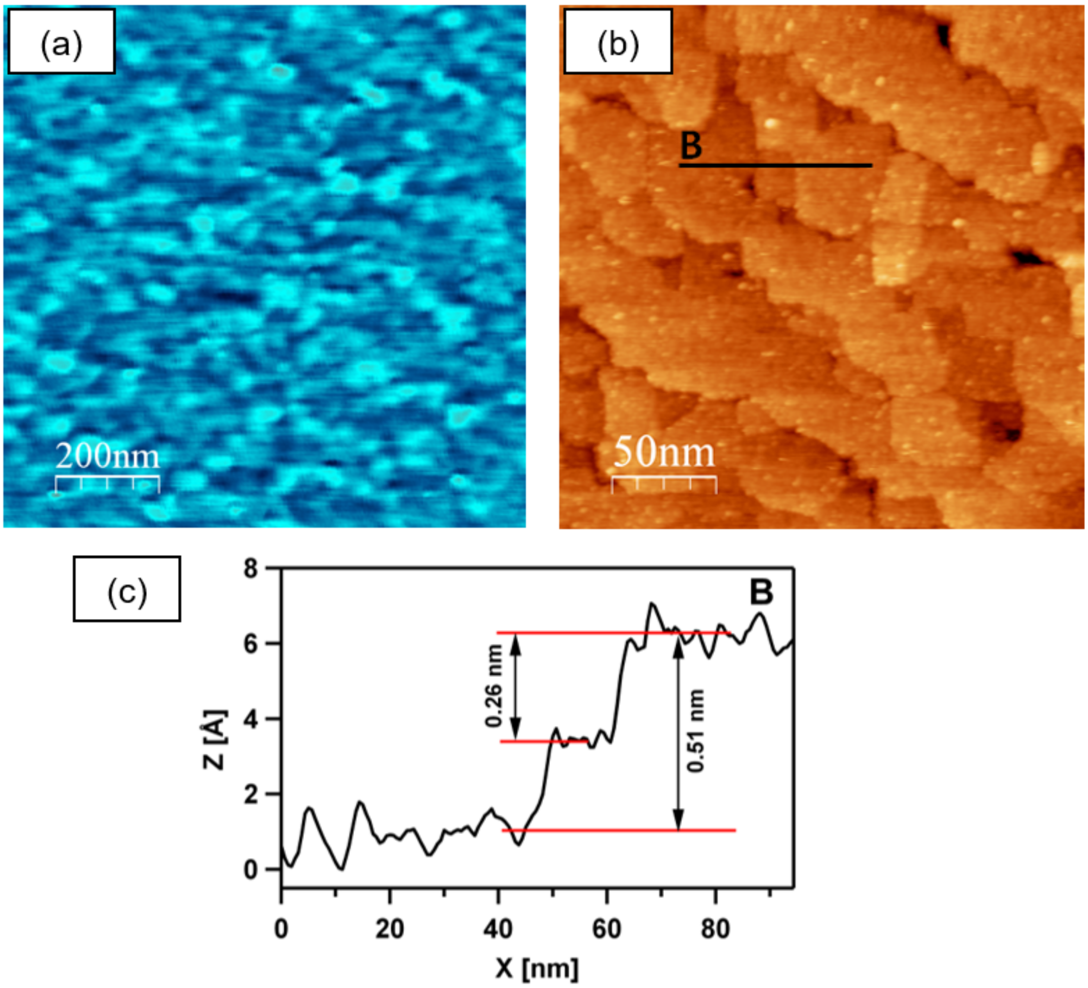

Figure 3.10. *Anatase TiO_2 on $LaAlO_3(001)$ - Sample G. (a) nc-AFM (10 000 Å × 10 000 Å); (b) STM image (2 500 Å × 2 500 Å, I_T = 0.5 nA, U_{bias} = 1.0 V) showing a continuous anatase film formed by the coalescence islands; (c) line scan along the line B from the image in (b) demonstrating that the height of the $TiO_2(001)$ layers corresponds to the height of 0.25 and 0.5 nm, respectively.*

The room temperature STM image of the anatase-TiO_2(001)-(4×1) surface, Figure 3.10.(b), shows a 2D surface with a stepped structure. Only two preferred step directions in the crystographically equivalent (100) and (010) directions were observed. The height of these steps on the TiO_2(001)-(4×1) surface was measured by STM in Figure 3.10.(c) to be 0.5 nm and 0.25 nm, respectively. These values correspond to two and one atomic-layer height steps and are in agreement with our

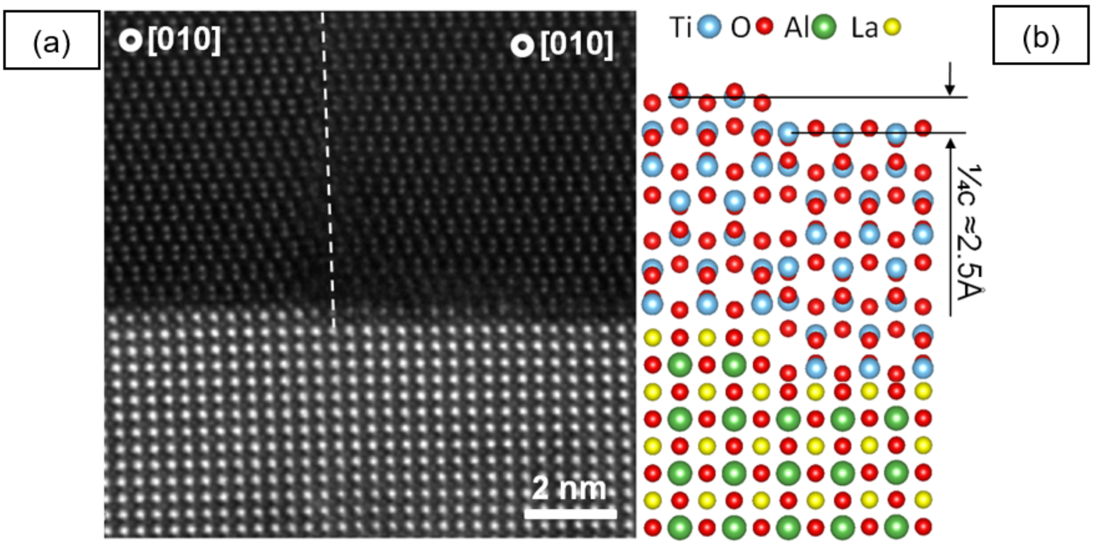

Figure 3.11. *Anatase TiO_2 on $LaAlO_3(001)$ - Sample G. (a) STEM image and (b) corresponding schematic of [010] boundary formed on step terrace with highest equal to 1/4c = 2.5 Å*

STEM results in Figure 3.11 [35]. Analysis of the frequent existence of steps with a single atomic-layer height suggests that the anatase-$TiO_2(001)$ surface exhibits two different surface truncations. It is expected, that these two truncations should have different surface structures as was observed for TiO_2 on $SrTiO_3(001)$ [15, 23, 26].

The quality of these data described above indicated that the TiO_2 thin film is a high-quality single crystal with an anatase structure. However, detailed STEM analysis revealed the presence of numerous domains in the thin film, indicating the existence of domain boundaries not only from the epitaxial growth either side of terrace steps but also within an individual terrace. Figures 3.11.(a) and 3.12.(a) correspond to Annular Dark Field (ADF) STEM images of the anatase-$TiO_2(001)$-(4×1) onto $LaAlO_3(001)$ substrate. The interface is determined based on the arrangement of atomic columns in bulk $LaAlO_3$ and TiO_2, confirms the formation of a clean and atomically abrupt interface between the two oxides, which means that the crystalline and epitaxial anatase TiO_2 phase on $LaAlO_3$ substrate was successfully produced. ADF images expose the chemical composition in the heteroepitaxy since the intensity of the atomic columns scales as approximately $Z^{1.7}$, where Z is the average atomic number. Therefore the contrast is dominated by the cations with higher atomic number, and the oxygen atoms are not visible. The interface in the system strongly indicates an LaO-terminated layer [27], where the layer of LaO makes direct contact to a TiO_2 layer with the interfacial Ti sitting above hollow sites of the surface unit of LaO for domain II

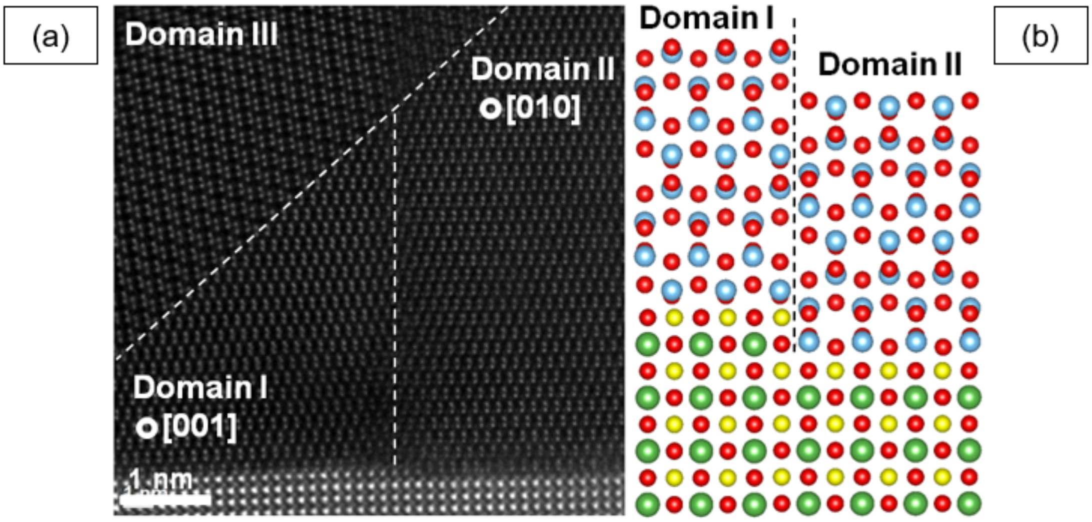

Figure 3.12. *Anatase TiO_2 on $LaAlO_3(001)$ - Sample G. (a) STEM image and (b) corresponding schematic of mixed type of domain I and II boundaries formed by 90° rotation plus a relative shift of α [001] $LaAlO_3$ due the substrate terrace and domain III which is not connected with the substrate.*

correspond to (001)[010]TiO_2//(001)[001] $LaAlO_3$ and above on top sites for domain I correspond to (001)[001]TiO_2//(001)[001] $LaAlO_3$. Those domains are related by a 90° rotation of the anatase and/or n/4 a[001] (=[010]) translation Figure 3.13.

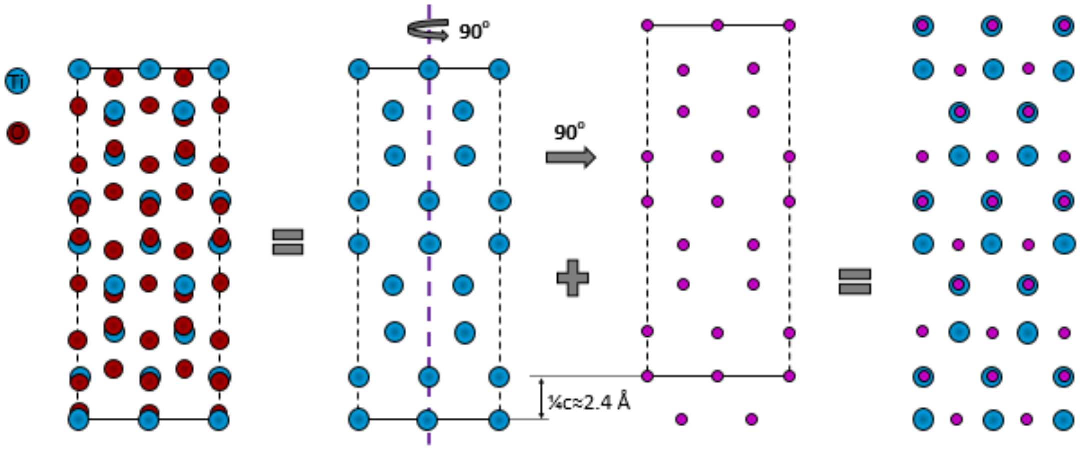

Figure 3.13. *The schamatic view of the domains I and II wich are related by 90 rotation.*

In Figure 4.12.(a) three types of domain boundaries that could be distinguished within the TiO_2 thin film based on the epitaxial growth relationship mentioned above are shown. Figure 3.11.(b) represents a structural model of the first type of domain, with the same orientation on the atomically flat LaO-terminated substrate surface with the substrate terraces observed in Figure 3.11.(a) [10]. No any changes in the first domain in the relationship to two different atomic steps were observed. From the STEM experiment, one atomic layer of TiO_2 along the c-axis corresponds to 1/4 of the unit cell, Figure 3.11.(b) [28, 26]. This result is in good agreement with our STM studies, shown in Figures 3.10.(b) and (c). The second domain can be described as 90° rotation plus a relative shift of a [001] $LaAlO_3$ (the terrace height), which is approximately equal to c3/8 [001] of TiO_2. An example is seen in the ADF-STEM image in Figure 3.12.(a), with its structural model in Figure 3.12.(b). The third additional observed domain boundary type in Figure 3.3.12(a) is not connected with the layer step from substrate but is the superposition of rotation and tilt of anatase phases. Those domains can also be preferential sites for the segregation of dopants, which can be similar to the role of grain boundaries in nano-crystalline anatase [29]. These domains appear to be common to all single-crystal anatase TiO_2 thin films grown on $LaAlO_3$, since all substrate have terraces and even without the presence of terrace steps, rotation domains are able to form inside the bulk crystal.

3.4. Conclusion

In summary, it has been shown that the degree of order of epitaxial anatase-TiO_2 thin films can be manipulated by varying growth parameters such as the sample temperature, sample to target distance, oxygen pressure, laser energy, and laser pulse frequency. Optimisation of the epitaxial growth of TiO_2 thin films on $LaAlO_3$(001) substrates was performed with the use of ultra-high vacuum PLD, and investigated by RHEED, LEED, XRD, AFM, STM, and STEM. The results obtained clearly demonstrate that the TiO_2 thin film, which covers the entire substrate, has a distinctly anatase phase, and can be atomically aligned and bonded to $LaAlO_3$(001) substrate. Anatase-TiO_2 thin films showed high crystalline quality, evidenced by RHEED, XRD, LEED, and atomic resolution STEM. Two, very well ordered domains (1×4) and (4×1) surface reconstruction of anatase were observed by RHEED and LEED. An analysis of the STM measurements indicates the coexistence of atomic steps of both 2.5 Å and 5 Å, confirming the existence of two TiO_2 domains. The STEM images also reveal that the interface is most likely terminated with a LaO layer.

References

[1] V. F. Silva, V. Bouquet, S. Deputier, S. Boursicot, S. Ollivier, I. T. Weber, V. L. Silva, I. M. G. Santos, M. Guilloux-Viry, A. Perrin, J. Appl. Crystallogr. **43** (2010) 1502.

[2] A. Lotnyk, S. Senz, D. Hesse, Thin Solid Films, **515** (2007) 3439.

[3] B.H. Park, J.Y. Huang, L.S. Li, Q.X. Jia, Appl. Phys. Lett. **80** (2002) 1174.

[4] B.S. Jeong, J.D. Budai, D.P. Norton, Thin Solid Films, **422** (2002) 166.

[5] X. Weng, P. Fisher, M. Skorwronski, P.A. Salvador, O. Maksimov, J. Cryst. Growth, **310** (2008) 545.

[6] J.Y. Huang, B.H. Park, D. Jan, X.Q. Pan, Y.T. Zhu, Q.X. Jia, Phil. Mag. A, **82** (2002) 735.

[7] M. Murakami, Y. Matsumoto, K. Nakajima, T. Makino, Y. Segawa, T. Chikyow, P. Ahmet, M. Kawasaki, H. Koinuma, Appl. Phys. Lett. **78** (2001) 2664.

[8] M. Zhu, T. Chikyow, P. Ahmet, T. Naruke, M. Murakami, Y. Matsumoto, H. Koinuma, Thin Solid Films, **441** (2003) 140.

[9] H. Sakama, G. Osada, M. Tsukamoto, A. Tanokura, N. Ichikawa, Thin Solid Films, **515** (2006) 535.

[10] S. Zheng, C.A.J. Fisher, T. kato, Y. Nagao, H. Ohta, Y. Ikuhara, Appl. Phys. Lett. **101** (2012) 191602.

[11] R. Ciancio, A. Vittadini, A. Selloni, R. Arpaia, C. Aruta, F.M. Granozio, U.S. di Uccio, G. Rossi, E. Carlino, J. Nanopart. Res. **15** (2013) 1735.

[12] S. Yamamoto, T. Sumita, T. Yamaki, A. Miyashita, H. Naramoto, J. Cryst. Growth, **237** (2002) 569.

[13] S. Kitazawa, Y. Choi, S. Yamamoto, T. Yamaki, Thin Solid Films, **515** (2006) 1901.

[14] S.A. Chambers, C.M. Wang, S. Thevuthasan, T. Droubay, D.E. McCready, A.S. Lea, V. Shutthanandan, C.F. Windisch Jr., Thin Solid Films, **418** (2002) 197.

[15] Y. Liang, S.P. Gan, S.A. Chambers, E.I. Altman, Phys. Rev. B, **63** (2001) 235402.

[16] M. Lazzeri, A. Selloni, Phys. Rev. Lett. **87** (2001) 266105.

[17] Y. Wang, H.J. Sun, S.J. Tan, H. Feng, Z.W. Cheng, J. Zhao, A.D. Zhao, B. Wang, Y. Luo, J.L. Yang, J.G. Hou, Nature Comm. **4** (2013) 2214.

[18] G.S. Herman, M.R. Sievers, Y. Gao, Phys. Rev. Lett. **84** (2000) 3354.

[19] R. Hengerer, B. Bolliger, M. Erbudak, M. Gratzel, Surf. Sci. **460** (2000) 162.

[20] M. Lazzeri, A. Vittadini, A. Selloni, Phys. Rev. B **63** (2001) 155409.

[21] K.J. Krupski, M. Moors, P. Jóźwik, T. Kobiela, A.R. Krupski, Materials **8** (2015) 2935.

[22] I. Horcas, R. Fernández, J.M. Gómez-Rodríguez, J. Colchero, G. Herrero, A.M. Baro, Rev. Sci. Instrum. **78** (2007) 013705.

[23] M. Radovic, M. Salluzzo, Z. Ristic, R. Di Capua, N. Lampis, R. Vagilo, F. Mietto Granozio, J. Chem. Phys. **135** (2011) 034705.

[24] A. Lotnyk , S. Senz, D. Hesse, Thin Solid Films, **515** (2007) 3439.

[25] T. Luttrell, S. Halpegamage, E. Sutter, M. Batzill, Thin Solid Films **564** (2014) 146.

[26] Y. Du, D.J. Kim, T.C. Kaspar, S.E. Chamberlin, I. Lyubinetsky, S.A. Chambers, Surf. Sci. **606** (2012) 1443.

[27] Z. Wang, W. Zeng, L. Gu, M. Satio, S. Tsukimoto, Y. Ikuhara, J. Appl. Phys. **108** (2010) 113701.

[28] M. Murakami, Y. Matsumoto, K. Nakajima, Appl. Phys. Lett. **78** (2001) 2664.

[29] B.P. Uberuaga, X.M. Bai, J. Phys: Condens. Matter, **23** (2011) 435004.

Chapter 4

Structure Determination of Au on Pt(111) Surface

4.1. Introduction

Properties of ultrathin gold layers deposited on the Pt(111) face were investigated in a number of works [1-12]. Studies on single crystalline Au-Pt(111) model surfaces, for instance, have provided detailed information on the catalytic properties of these surfaces [1-3]. Davies *et al.* [1] studied the growth and chemisorptive properties of gold and silver monolayers on platinum (111) and (553) single crystal surfaces using Auger electron spectroscopy (AES), LEED, and temperature-programmed desorption (TPD). The AES results suggested that the growth of Au proceeds via a Stranski-Krastanov mechanism at room temperature, and that at temperatures above 800 K gold dissolves into the Pt crystal bulk. No extra LEED order spots or spot streaking was observed. In contrast, Shatler *et al.* [2] with the use of AES, LEED, and TPD found that deposition of gold on Pt(111) near T = 300 K indicates a layer-by-layer (Frank-van der Merwe) growth mechanism up to three gold monolayers. The analysis of AES measurements showed that two-dimensional islands growth below one monolayer took place. Furthermore, with increasing coverage, the gold islands grew until the monolayer is completed, before the second layer begins to form. In additional studies by Sachtler *et al.* [3], the activity for conversion of n-hexane as a function of Au surface concentration on Pt(111) was monitored. The Au-covered crystal was then annealed at elevated temperatures to allow Au intermixing with the Pt substrate. The formed Au-Pt(111) surface alloy showed a much higher activity for n-hexane isomerization than pure Pt. Moreover, it has been reported that Au in a dispersed state exhibits a high activity for some reactions at low temperatures (e.g., CO oxidation) [5] and that this feature depends on the preparation conditions, size and shape of the Au nanostructures [6]. Adsorption experiments with CO as a titration agent showed a significantly lower affinity of the Au-Pt surface alloy in comparison to the clean Pt surface [7]. Salmeron *et al.* [8] used photoelectron spectroscopy techniques (UPS (ultraviolet) and XPS (X-ray)), LEED and AES to study the electronic structure of Au and Ag overlayers deposited on Pt(111), Pt(100), and Pt(997). Between 0 and 1 monolayer, the valence bands of Au and Ag show changes in the form of shifts of the most tightly bound peaks and the appearance of the new structures around a coverage (θ_{Au}) of one monolayer. The Au $5d_{3/2}$ peak shifts 0.6 eV towards higher binding energies when coverage varies from 0.1 to 1 monolayer and 0.5 eV more when coverage varies from one to six monolayers. These shifts are explained as due to the changing contributions of the Au atoms in island edges for surface ($\theta_{Au} < 1$) monolayer and bulk ($\theta_{Au} > 1$) coordination positions. Using AES, they found that gold on Pt(111) grows layer-by-layer. Below $\theta_{Au} < 1$, no extra LEED spots were observed. In addition, the work function decreased upon gold deposition from its initial value of 6.08 ± 0.15 eV for clean Pt(111) down to 5.8 ± 0.15 eV. That value was reached at the monolayer and remained constant thereafter up to five monolayers and is clearly larger than the 5.31 eV value reported by Potter *et al.* [13] for bulk Au(111). The work function for the Pt(111) surface compares only fairly with that reported by Ertl *et al.* [14] of 6.40 eV. Its smaller value might reflect a less perfect surface with larger number of residual steps. It should be pointed out here that Pt(111) surface presents the highest work function value among other metals surfaces. Vogt *et al.* [9] studied Au/Pt(111) system by spin-, angle- and energy-resolved photoemission with normal incident circularly polarized synchrotron radiation of BESSY and normal photoelectron emission for different Au coverages. The prepared layers were characterized by AES and LEED and turned out to grow up two-dimensionally and epitaxially. LEED spots did not show any changes in geometry during the evaporation time up to the coverage of a thick Au layer [9]. Later, the electrodeposition of Au on Pt(111) from electrolytes containing μM concentrations of $AuCl_4^-$ was investigated by *in situ* electrochemical scanning tunneling microscopy (EC-STM) by Sibert *et al.* [11,12]. Under conditions of high Au surface mobility, multilayer growth proceeds via a typical Stranski-Krastanov growth mode, with layer-by-layer growth of a pseudomorphic Au film up to two monolayers and three-dimensional growth of structurally relaxed islands at higher coverage, indicating thermodynamic control under these conditions.

In the present work, in order to study the structural and electronic properties during the initial adsorption process of gold on Pt(111) surface at room temperature, we have performed low-energy electron diffraction, scanning tunneling microscopy measurements in ultrahigh vacuum and density functional theory calculations with the use of CASTEP code.

4.2. Experimental Details

The measurements were carried out in a stainless steel ultra-high vacuum chamber with a base pressure of 2.0×10^{-8} Pa. The chamber was equipped with a reverse-view LEED optics, which was used for low-energy electron diffraction measurements, and also with a variable-temperature scanning tunneling microscopy stage. The Pt(111) single crystal was supplied by MaTeck [15]. The surface of the Pt(111) single crystal was cleaned by repeated cycles of sputtering with 3 keV Argon ions at T = 300 K and annealing at T = 1100 K. After annealing at 1100 K, the residual carbon was removed in 7.0×10^{-4} Pa of oxygen, followed by desorption of any remaining oxygen at 1200 K. This procedure was repeated until the LEED pattern of a clean Pt(111) surface with sharp spots and low background was obtained. The deposition of Au (99.999%) on the Pt(111) sample was achieved by vaporization from a Knudsen cell and the coverage of gold was determined via STM. Film coverages are described in monolayers (ML), where a 1 ML Pt(111) film corresponds to an atomic packing density of 1.503×10^{15} atoms/cm^2 obtained from a bulk lattice constant a_{Pt} = 3.9239 Å [16] (for comparison the atomic packing density of Au(111) equals 1.387×10^{15} atoms/cm^2 for a_{Au} = 4.0785 Å [46]). This cell had been constructed from an Al_2O_3 crucible from Friatec [17] with a diameter of 5 mm. It was filled with a 0.5 mm thick Au wire from Goodfellow [18] and closed by a two-hole ceramic. The Knudsen cell was heated by a tungsten wire from Goodfellow (diameter 0.3 mm) wound around the crucible and thermally shielded by a water-cooled jacket. In order to control the deposition time, a rotatable shutter was placed in front of the cell opening. The working pressure during Au deposition was below 1.0×10^{-7} Pa.

All STM measurements were performed with the use of electrochemically etched W (99.99%) tips (diameter 0.5 mm, length 3.5 mm). For the potassium hydroxide electrolyte, a 4 V_{p-p} square wave voltage (f = 100 Hz) was applied to the tip. In the electrochemical cell, a tungsten wire is used as the working electrode (anode) and a Pt (99.999%) loop (diameter 10 mm) is used as the counter electrode (cathode). A 3 M KOH solution from Sigma Aldrich [19] is used as the electrolyte. The following reactions take place:

Cathode Pt (Reduction Reaction):

$$6e^{-} + 6K^{+} + 6H_2O + Pt_{CATALYSTS} \rightarrow 6KOH + 3H_2 + Pt_{CATALYSTS} \quad (4.1)$$

Anode W (Oxidation Reaction):

$$W \rightarrow W^{6+} + 6e^{-} \quad (4.2)$$

$$W^{6+} + 6KOH \rightarrow W(OH)_6 + 6K^{+} \quad (4.3)$$

Total Reaction:

$$W + 6H_2O + 6KOH + Pt_{CATALYSTS} \rightarrow W(OH)_6 + 3H_2 + 6KOH + Pt_{CATALYSTS} \quad (4.4)$$

All presented STM images were recorded in constant current mode and processed by the WSXM image-processing software [20]. Before starting experimental investigations of the Pt(111) and Au-Pt(111) surfaces, the experimental system was calibrated with the use of well know Si(111)-(7 × 7) reconstructed surface [21–24] (Figure 4.1).

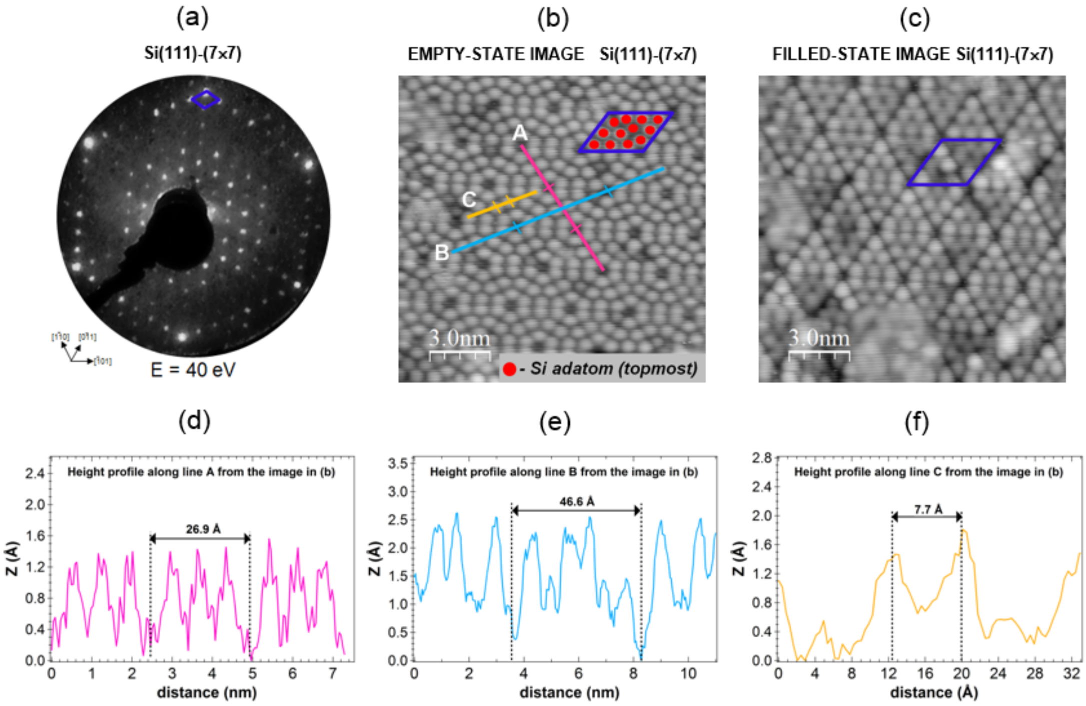

Figure 4.1. *Si(111)-(7 × 7) surface at T = 300 K: (a) LEED patterns recorded at normal electron incidence for E = 40 eV; (b) STM image of empty states (150 Å × 150 Å, I_T = 0.5 nA, U_{bias} = +1.6 V); and (c) STM image of filled states (150 Å × 150 Å, I_T = 0.5 nA, U_{bias} = −1.6 V). Au deposited on Pt(111) at T = 300 K at a coverage $\theta_{Au} \leq 1.0$ ML: (a) $\theta_{Au} \approx 0.8$ ML (5000 Å × 5000 Å, I_T = 4.0 nA, U_{bias} = 1.0 V); (d–f) line scans along the lines A, B, and C from the image in (b). The unit cell is indicated by the blue diamond (diagonals: a_1 = 46.6 Å, a_2 = 26.9 Å). Si adatoms (12 per surface unit cell) cell are marked as red dots.*

Si(111)-(7 × 7) surface was prepared by twice direct current flashing (I = 4.0 A) an *p*-type Si(111) substrate (size: 1 × 10 × 0.5 mm, resistivity ρ ≈ 1–10 Ω cm) at 1220 K, after degassing at 970 K for two hours by joule heating with a current of 1 A. Atomically resolved STM images of the empty and filed states of Si(111)-(7 × 7) are presented in Figure 4.1.(b),(c), respectively. The measured surface unit cell is characterized by two diagonals of the diamond (a_1 = 46.6 Å and a_2 = 26.9 Å). Silicon adatoms (12 per unit cell) are marked in red in Figure 4.1.(b), and they occur as bright "dots" in empty-state STM image. Visible in STM images deep holes (depth ~ 2 Å) are called corner hols

4.3. Calculation Details

All calculations were performed based on the pseudo-potential plane-wave within the density functional theory [25,26], using the Cambridge serial total energy package (CASTEP) [27]. The effects of exchange correlation interaction are treated with the generalized gradient approximation (GGA) of Perdew-Burke-Ernzerhof (PBE) [28,29]. The ultra-soft pseudo-potentials [30] describe this electron-ion interaction system to high accuracy with a plane wave energy cutoff of 600 eV. The energy calculations in the first irreducible Brillouin-zone were conducted by using the (4×4×1) k-point grid of the Monkhorst-Pack scheme [31]. Spin polarization of platinum was included in the calculations to correctly account for its magnetic properties. All atomic positions have been relaxed according to the total energy and force using the BFGS scheme [32] based on the cell optimization criterion RMS force of 0.03 eV/Å, stress of 0.05 GPa, and displacement of 0.001 Å. The calculation of total energy and electronic structure is followed by cell optimization with SCF tolerance of 1×10^{-6} eV/atom. The Pt(111) surface was modeled using a slab containing 7 (=15.84 Å) and 10 (=22.63 Å) layers of Pt atoms with a vacuum gap in the [111] direction equal to 20.57 Å and 30.37 Å, respectively. Full slab relaxation was performed in both cases.

4.4. Results and Discussion

4.4.1. LEED and STM

Gold atoms on the Pt(111) face form an ordered structure after evaporation onto the crystal face. Typical LEED pattern observed before and after deposition of gold on the Pt(111) face in normal electron incidence are shown in Figure 4.2. In this figure, the unit cell of the platinum lattice is indicated. The lattice constant of the platinum surface unit cell is 2.775 Å (primitive *fcc* (111) unit cell) [63]. The patterns are shown to demonstrate the quality of the structural order at the surface. It should be pointed out that the positions of the LEED spots associated with the Pt(111) substrate remains unchanged during the gold deposition at 300 K (Figure 4.2.(c)), as was previously reported by Sachtler and Samorjai [32] and Vogt *et al.* [40]. Thus, the lattice constant of the first substrate layer remains constant, too, and suggests a two-dimensional growth of the first gold layer.

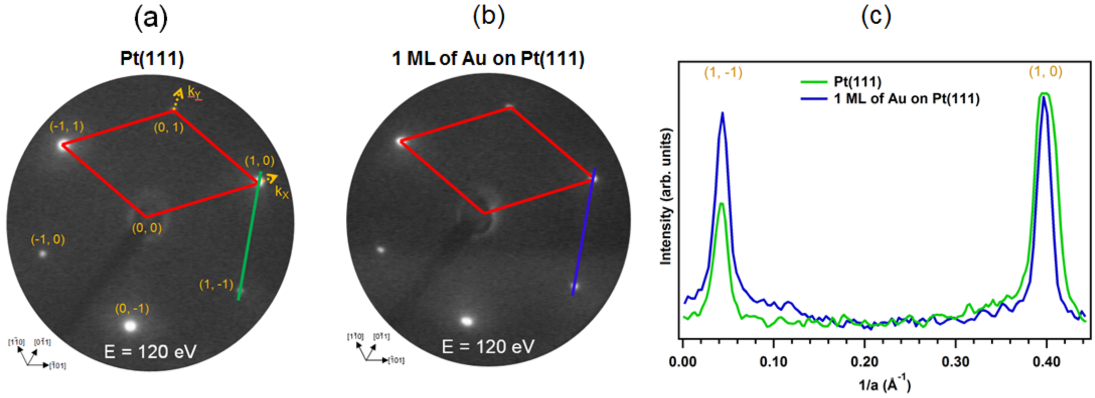

Figure 4.2. *LEED patterns observed during the growth of Au on the Pt(111) surface recorded at normal electron incidence for E = 120 eV, and T = 300 K: (a) clean Pt(111) for E = 120 eV.* k_X *and* k_Y *denote axes in the reciprocal lattice; (b) 1 ML of Au on Pt(111); and (c) line profile along the lines from the image in (a,b) demonstrating that the position of LEED spots remain unchanged after gold deposition. The unit cell is outlined.*

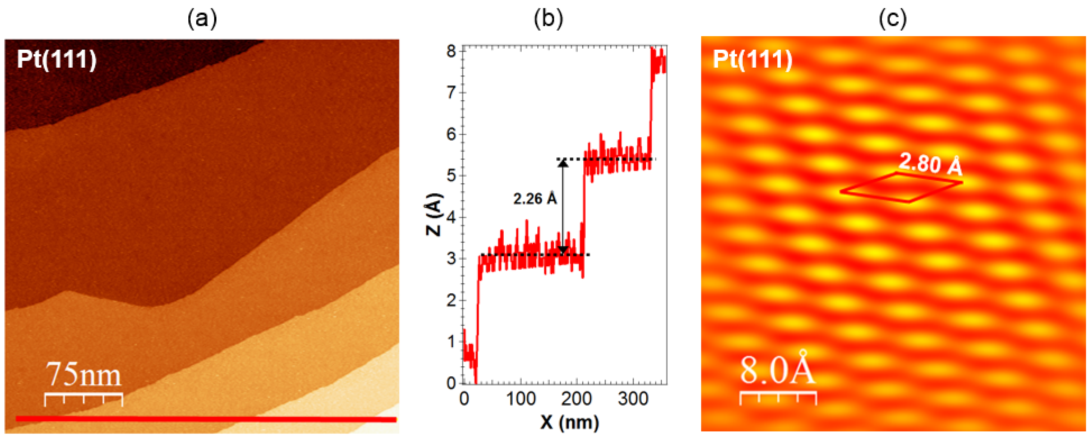

Figure 4.3. *STM images of the clean Pt(111) surface: (a) T = 25 K (3734 Å × 3734 Å,* I_T *= 141 pA,* U_{bias} *= +50 mV); (b) line-scan corresponding to line drawn in (a); and (c) T = 300 K (40 Å × 40 Å,* I_T *= 49 pA,* U_{bias} *= +48 mV). The unit cell is outlined. STM image evidences a hexagonal lattice arrangement of Pt atoms with measured nearest neighbor distance of 2.80 Å.*

The results of our STM measurements on the clean Pt(111) surface are presented in Figure 4.3. Figure 5.3.(a) displays an STM image, taken on a low-index Pt(111) substrate with terraces between 100 and 300 nm width separated by monoatomic steps.

The height of the steps on the Pt(111) surface was measured by STM to be 2.26 ± 0.3 Å (Figure 4.3.(b)). However, one need to remember that the observed by STM step height includes geometric and electronic factors. Figure 4.3.(c) presents atomic resolution of the Pt(111) face. The obtained topography shows a hexagonal lattice arrangement of Pt atoms with the nearest neighbor distance of 2.80 Å. This value describes the dimension of the surface unit cell and is 0.90% higher compared to the literature value (=2.775 Å) [33]. Figure 4.3.(c) demonstrates that the surface structure seen in the obtained STM image has a clear long-range character. Figure 4.4 shows STM images of the Pt(111) surface with varying Au coverage in order to illustrate the morphology of the Au layers deposited on Pt at room temperature. Figure 4.4.(a) shows a typical STM image corresponding to a submonolayer coverage of $\theta_{Au} \approx 0.8$ ML. An analysis of the STM measurements indicates that for coverage less than 1 ML, two-dimensional growth of the gold layer is observed. This is in agreement with photoelectron spectroscopy [8] and our present and previous AES/LEED measurements [2,9]. The darker features in Figure 4.4.a represent the still visible platinum substrate as predicted in the previous studies [2]. Similar to the results observed by us, the two-dimensional gold monolayer was obtained by electrodeposition of Au on Pt(111) from electrolytes containing μM concentrations of of $AuCl_4^-$ [12]. The line scan in Figure 4.4.(b) shows that the height of the first gold layer corresponds to the height of a single Pt step height equal to 2.26 Å. As the Au coverage is close to 1 ML, Au wets the Pt(111) surface completely, as can be seen in Figure 4.4.(c). This is not easy to confirm with STM, whether the surface is wetted or not. However, the reason for the perfect wetting is because of the high-specific surface free energy of the Pt(111) surface (2.299 J/m^2 < $\gamma_{Pt(111)}$ < 2.489 J/m^2) [34–38] as compared with that of the Au(111) surface (1.283 J/m^2 < $\gamma_{Au(111)}$ < 1.506 J/m^2) [34–38]. Since the total specific surface free energy should be minimized, a covered Pt(111) surface is favored [69]. Closer view of the STM image topography in Figure 5.4.(d) reveals the presence of well-ordered gold structures. STM images indicate a long-range order in the surface system. The obtained topography shows a hexagonal lattice arrangement of Au atoms with a nearest neighbor distance of 2.80 Å, which is exactly the same value as mentioned above in the case of Pt atoms. The same value of the surface unit cell after adsorption of gold could suggest that the gold atoms are adsorbed in sites (hollow *fcc* or *hcp*), which are a direct continuation of the Pt lattice *ABCABCA*. This is in good agreement with the supposition from the spin-resolved photoemission studies of Au-Pt(111) system [10], where the best fit of experimental results and theoretical model was achieved on that basis.

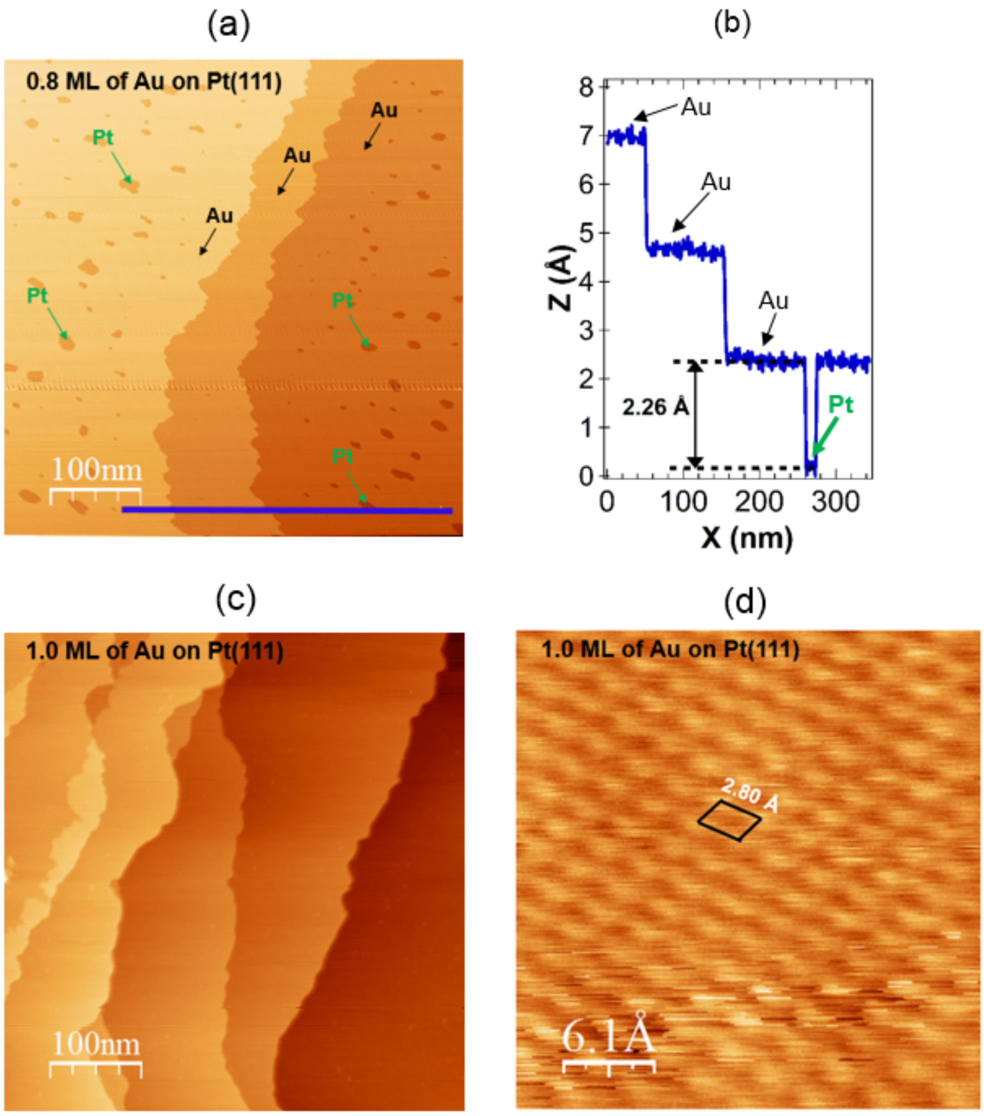

Figure 4.4. *STM images of Au deposited on Pt(111) at T = 300 K at a coverage* $\theta_{Au} \leq$ *1.0 ML: (a)* $\theta_{Au} \approx 0.8$ *ML (5000 Å × 5000 Å,* $I_T = 4.0$ *nA,* $U_{bias} = +1.0$ *V); (b) line scan along the line from the image in (a) demonstrating that the height of the gold layer corresponds to the height of a single Pt step height; (c)* $\theta_{Au} \approx 1.0$ *ML (5000 Å × 5000 Å,* $I_T = 2.0$ *nA,* $U_{bias} = +1.0$ *V); and (d) (30 Å × 30 Å,* $I_T = 4.65$ *nA,* $U_{bias} = +159$ *mV). The unit cell is outlined. STM image evidences a hexagonal lattice arrangement of Au atoms with measured nearest neighbor distance of 2.80 Å.*

4.4.2. DFT

4.4.2.1. Structure of Clean Pt(111)

In the theoretical part of our work, we have calculated multilayer relaxations of the Pt(111) system using the slab with 7 and 10 atomic layers. Figure 4.5.(a) shows the schematic view of relaxed slab structure for the seven platinum layers. The platinum low-index surface was modeled by repeated slabs with a (1×1) surface unit cell with four atoms in each layer. The calculated atomic layer distances for seven and ten planes are shown in Table 5.5. d_{i-j}^{X-Y} defines the distance along the surface normal direction between the *X* atom at the *i* atomic layer and the *Y* atom at the *j* atomic layer. Surface relaxation Δd_{i-j}^{X-Y} is characterized as the percent of change of the spacing between layers *i* and *j versus* the bulk layer spacing (d^0). Bulk value (d_0) is taken from our GGA calculations and describes average distance between atomic planes of seven (=2.30 Å) and ten (=2.29 Å) platinum layers, respectively. Further calculations of gold adsorption on Pt(111) surface has been performed on seven platinum layers.

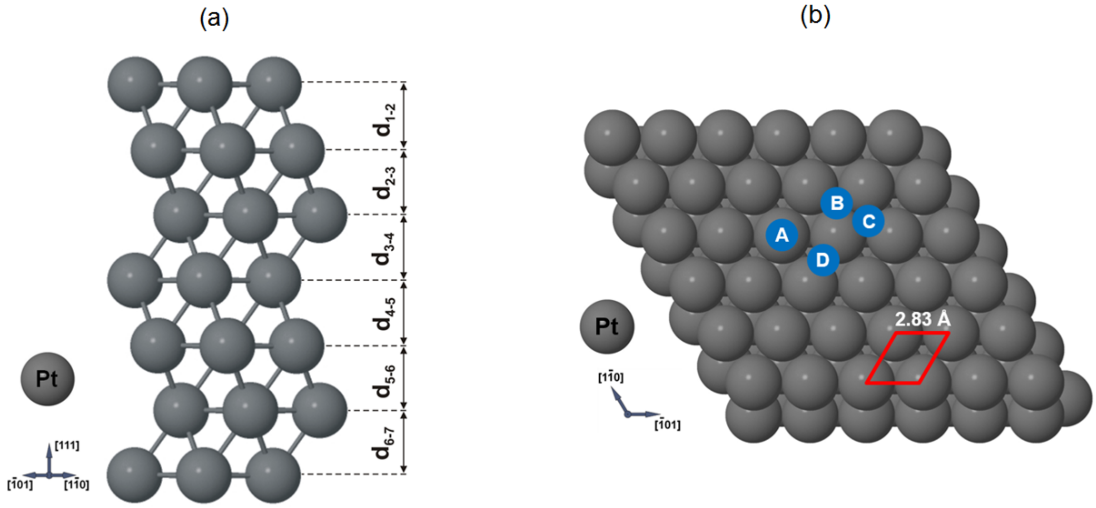

Figure 4.5. (*a) Side view of the relaxed Pt(111) surface for seven layers. Values of denoted characteristic inter plane distances are given in Table 1. (b) Considered positions of Au adsorption on the Pt(111) surface: A—on top; B—hollow fcc; C—hollow hcp; and D—bridge. The unit cell is outlined. The nearest neighbor Pt-Pt distance of 2.83 Å is obtained from our theoretical calculations.*

Our calculations for the clean Pt(111) show very good agreement with the above-presented STM results and with the other experimental and theoretical literature studies [40,41,49-57] presented in Table 4.1. Obtained lateral geometrical properties of Pt(111) surface and distances between the nearest Pt atoms in the

	Present work GGA *(CASTEP)*				Previous DFT study		LEED	SXRD[g]	
d_{i-j}^{X-Y} (Å)	7 layers	Δd_{i-j}^{X-Y} (%)	10 layers	Δd_{i-j}^{X-Y} (%)	d_{i-j}^{X-Y} (Å)	Δd_{i-j}^{X-Y} (%)	d_{i-j}^{X-Y} (Å)	d_{i-j}^{X-Y} (Å)	Δd_{i-j}^{X-Y} (%)
d_{1-2}^{Pt-Pt}	2.32	+0.87	2.33	+1.75	2.766[h] (LDA)	+0.44[h] (LDA) +0.85[i] (GGA) +1.14[j] (LDA) +0.85[j] (LDA)	2.26[a] 2.29 ± 0.1[b] 2.2713[c] 2.26 ± 0.05[d] 2.2655 ± 0.025[e] 2.29 ± 0.001[f]	2.31 ± 0.005	+2.0
d_{2-3}^{Pt-Pt}	2.29	-0.43	2.29	-	2.746[h] (LDA)	-0.31[h] (LDA) -0.56[i] (GGA) -0.29[j] (LDA) -0.22[j] (LDA)	2.26[a] 2.2405 ± 0.025[e] 2.27 ± 0.003[f]		
d_{3-4}^{Pt-Pt}	2.30	-	2.29	-		-0.15[i] (GGA) -0.21[j] (LDA) -0.17[j] (LDA)	2.26[a] 2.2655 ± 0.05[e]		
d_{4-5}^{Pt-Pt}	2.30	-	2.30	+0.43			2.26[a]		
d_{5-6}^{Pt-Pt}	2.29	-0.43	2.29	-					
d_{6-7}^{Pt-Pt}	2.30	-	2.30	+0.43					
d_{7-8}^{Pt-Pt}			2.29	-					
d_{8-9}^{Pt-Pt}			2.29	-					
d_{9-10}^{Pt-Pt}			2.30	+0.43					
d_0 (Å)	2.30		2.29		2.75[h] (LDA)		2.26[c] 2.2655[e] 2.265[f]	2.26	
a_0 (Å)	3.99		3.99		3.99[i] (GGA) 3.97[j] (GGA) 3.89[j] (LDA)	3.92[k] (EXP)	3.92[a] 3.9231[d]		

[a] Ref. [49-50]; [b] Ref. [51]; [c] Ref. [52]; [d] Ref. [53]; [e] Ref. [54]; [f] Ref. [55]; [g] Ref. [56]; [h] Ref. [57]; [i] Ref. [40]; [j] Ref. [41]; [k] Ref. [42].

Table 4.1. *Distances ($\mathbf{d}_{i-j}^{X-Y}$) between the atomic planes of the relaxed Pt(111) system, and their percentage changes ($\Delta\mathbf{d}_{i-j}^{X-Y}$) with respect to the bulk value (d_0), calculated for the slab with 7 and 10 atomic layers and compared with experimental [42, 49-56] and theoretical [40,41,57] literature data. Notation of inter-plane distances are the same as in Figure 1. $\mathbf{d}_{i-j}^{X-Y}$ denotes the interlayer spacing between layers i and j for the X and Y atoms type. d_0—average distance between atomic planes of seven and ten layers, respectively. a_0—lattice constant of Pt. GGA—generalized gradient approximation, LDA—local density approximation, LEED—low energy electron diffraction, SXRD—surface X-ray diffraction.*

structure (=2.83 Å) are very close to STM measurements (=2.80 Å), with the difference about 1%. The first and second interlayer spacings of the clean Pt(111) surface were determined to be 2.32 Å and 2.29 Å, respectively, in case of calculated slab with seven atomic layers. This corresponds to a +0.87% expansion and −0.43% contraction of the first and second metal layer spacings of the ideally terminated Pt(111) clean surface (=2.30 Å), respectively. These values and the value obtained in our calculations of lattice constant of the bulk Pt (=3.99 Å) are in excellent agreement with the previous GGA calculations [70] and surface X-ray diffraction results [56] (Table 4.1). However, comparison of our calculations to the quantitative low-energy electron diffraction value of the first interlayer spacing shows that our theoretical value (=2.32 Å) is slightly larger (+2%) then the average value of 2.27 Å observed experimentally [49-55].

4.4.2.2. Structure of the Au/Pt(111) System

Figure 4.5.(b) shows the four possible gold adsorption sites on the Pt(111) surface with one on-top site (labeled as A), two hollow sites: hollow *fcc* (labeled as B), hollow *hcp* (labeled as C), and one bridge site (labeled as D), In our calculations, we define one monolayer of adsorbed Au atoms corresponding to the same atoms as the atomic sites in the surface layer. One Au atom adsorbing on the Pt(111) surface corresponds to an adsorption coverage of 0.25 ML. The minimum adsorption energy (E_{ads}) was calculated by means of the following total energy difference:

$$E_{ads} = E_T\left(\frac{Au}{Pt(111)}\right) - E_T(Au) - E_T(Pt(111)) \qquad (4.5)$$

where E_T is the total energy of the system and $\frac{Au}{Pt(111)}$, Au, and $Pt(111)$ refer to the atom-on-metal system, the free Au atom, and the bare Pt surface, respectively.

Table 4.2 displays the predicted adsorption energies of Au on the Pt(111) surface and the distance between the Au atom and its nearest (r_{NN}) and next nearest neighbors

(111)	Site	E_{ads} (eV)	r_{NN} (Å)	r_{NNN} (Å)
Au on top	A	+0.580	2.58	3.76
Hollow *fcc*	B	−0.578	2.74	3.89
Hollow *hcp*	C	−0.518	2.75	3.92
Bridge	D → B	−0.578	2.74	3.89

Table 4.2. *Calculation results of one Au atom adsorption on the Pt(111) surface. E_{ads}—adsorption energy; r_{NN} and r_{NNN} describe the distance to the nearest (NN) and next-nearest (NNN) neighbors. D → B means that after calculations gold atom has moved from the bridge position D towards the most favorable hollow fcc position B.*

(r_{NNN}). A, B, C and D describe positions of Au atom on the Pt(111) surface before starting calculations. As one can see, only in the case of bridge position D displacement of gold atom towards hollow *fcc* position B is observed, while the other gold adsorption positions described as A, B and C remain unchanged. Results for the atom in an A position sugest that the wrong settings was choisen during the calculations. Thos settings not alloved to move atom to the most stable position. The comparison of the calculated adsorption energies reveals that the preferred position of the Au on the Pt(111) surface is the hollow *fcc* with the E_{ads} = −0.578 eV. At this favorable position, the nearest to the nearest (NN) and next-nearest (NNN) neighbor distance is equal to 2.74 Å and 3.76 Å, respectively (chapter 4.4.1). The adsorption energy of one gold atom in hollow *fcc* site is negative, which indicates in addition that this adsorption position is the most stable. Similar conclusion was obtained in case of a quantitative LEED analysis of the structure of Pt(111) (√3 × √3) R30°-S, where the best agreement between experiment and theory has been found for a model with a sulfur atom in the three-fold hollow *fcc* site [49]. Moreover, our theoretical studies are in agreement with the spin-resolved photoemission predictions where the Au is adsorbed in sites, which are a direct continuation of the Pt lattice [10]. In contrast to very stable hollow *fcc* site, the on-top adsorption position is the most unstable place with E_{ads} = +0.580 eV. Next, taking into account our experimental STM results, we have considered structural model of the Au/Pt(111) surface reproducing in the best way the topography of the obtained STM images. Structural relaxation has shown that such a model is stable. The lateral positions of all gold atoms in the relaxed structure remained the same as in the starting configuration. This model assumes that the gold structure is built up by Au hollow *fcc* and hollow *hcp* atoms (Figure 4.6). The obtained lateral geometrical properties of this

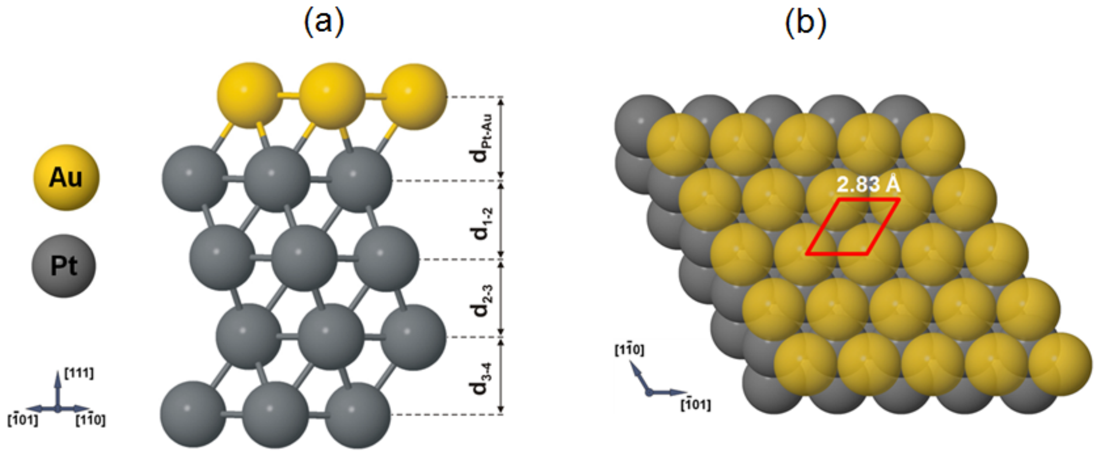

Figure 4.6. *(a) Side view of the calculated most stable hollow fcc position of a relaxed Au atom on the Pt(111) surface; (b) top view of the calculated Au/Pt(111) surface. The unit cell is outlined. The nearest neighbor Au-Au distance of 2.83 Å is obtained from our theoretical calculations.*

Au/Pt(111) model and distances between the nearest gold atoms in the structure (=2.83 Å) are almost the same as those following STM measurements (=2.80 Å) with the difference close to 1%. Table 4.3 presents obtained changes in the Pt(111) geometry

d_{i-j}^{X-Y} (Å)	**Adsorption Site B 8 Layers**	Δd_{i-j}^{X-Y} **(%)**
$d_{\cdot}^{Pt-Au}$	2.36	+2.16
d_{1-2}^{Pt-Pt}	2.34	+1.30
d_{2-3}^{Pt-Pt}	2.31	-
d_{3-4}^{Pt-Pt}	2.32	+0.43
d_{4-5}^{Pt-Pt}	2.31	-
d_{5-6}^{Pt-Pt}	2.30	−0.43
d_{6-7}^{Pt-Pt}	2.33	+0.86
d_0	2.31	

Table 4.3. *Calculated distances (d_{i-j}^{X-Y}) between the atomic planes of the relaxed Au-Pt(111) system, and their percentage changes (Δd_{i-j}^{X-Y}) with respect to the ideal Pt bulk value (d_0), for the slab with eight atomic layers (see slab and top view of the considered structure in Figure 5.6).*

induced by the presence of a two-dimensional gold layer. Namely, we find the top interlayer spacing $d_{\cdot}^{Pt-Au}$ noticeably expanded by +2.16% with respect to the ideal platinum bulk value (=2.31 Å). The calculated value of the surface free energy of gold layer equals to γ_{Au} = 1.481 J/m^2, and it is in very good agreement with the value of the surface free energy of Au(111) mentioned in literature (1.283 J/m^2 < $\gamma_{Au(111)}$ < 1.506 J/m^2) [34–38].

4.4.2.3. Density of States

The calculated electronic structure (density of states—DOS) for the studied adsorption system is presented in Figure 4.7. The DOS curve for bare Pt(111) and Pt(111) covered

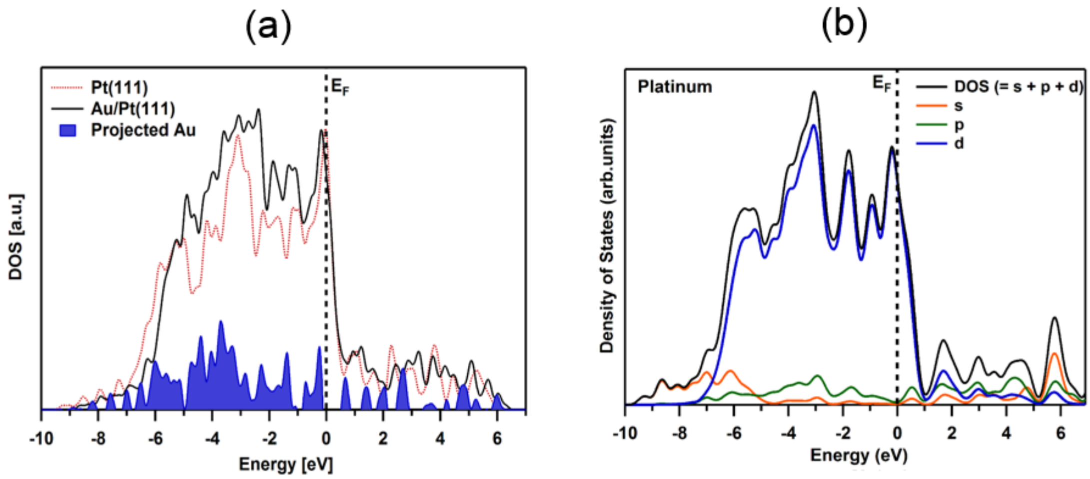

Figure 4.7. *Density of states curves for gold on Pt(111): (a) Clean Pt(111) (red dotted line); 1 ML of Au on Pt(111) (black line). The projection of the adsorbed gold density of states is shaded in blue. (b) Clean bulk platinum (black line) and its components associated with s (orange line), p (green line) and d (blue line) orbitals. E_F denotes Fermi level.*

by Au is displayed in Figure 4.7.(a) as red dotted and black line, respectively. In case of Au/Pt(111) surface, the DOS curve was obtained by considering gold atoms sitting in the most stable hollow *fcc* positions. Density of states distributions of Pt(111) and Au/Pt(111) systems were calculated for seven (clean platinum) and eight (one gold monolayer on platinum) atomic layers, respectively. In the case of density of states for clean Pt(111) surface, our results are in very good agreement with previous theoretical studies [43,44,49–51]. Changes in the electronic properties of our Au/Pt(111) system, compared to Pt(111), are visible. In particular, noticeable increase in the intensity of occupied states in the energy range between −5 and −1 eV, and slight change of the DOS shape after including of one gold layer into calculations. On the other hand, adding of the gold layer did not increased the intensity as much as it could be expected for the d metal like gold [58]. The presented result suggest that further theoretical studies are required for better understanding of the adsorption process of gold on the Pt(111) surface. Both alterations, mainly attributed to the interaction of Au atoms with

Pt(111) surface [9,10], are represented by the projection of the adsorbed gold density of states in Figure 4.7.(a). Density of states distribution calculated for the bulk platinum presented in Figure 4.7.(b), confirms well that the electronic structure of platinum is dominated by d state within the whole considered energy range.

4.5. Conclusion

In this work, experimental and theoretical studies of the geometrical and electronic properties of (111) surface of the ordered Au-Pt adsorption system have been presented. The analysis of LEED and STM measurements indicates that for a coverage below 1 ML, two-dimensional growth of the first Au monolayer takes place. Based on LEED results, no change of the lattice constant after gold adsorption was observed. The topography of the obtained STM images of Pt(111) and Au/Pt(111) surfaces on the level of the atomic resolution demonstrate that the surface structures have hexagonal arrangement of atoms and that the surface lattice constant is equal to the distance between the nearest platinum surface atoms (=2.80 Å). This is in very good agreement (close to 1%) with our presented DFT calculations, where the distances between the nearest atoms in the case of bare Pt(111) and Au/Pt(111) surface equal to 2.83 Å. It was shown that the first and second interlayer spacings of the clean Pt(111) surface were determined to be expanded by +0.87% and contracted by −0.43%, respectively. The calculated adsorption energy of the Au atom on the Pt(111) surface is dependent on the adsorption site, and there is a preference for a hollow *fcc* site (E_{ads} = −0.578 eV). In the presence of gold layer on the Pt(111) surface, the top interlayer spacing was found expanded by +2.16% with respect to the ideal bulk value. Density of states for the Pt(111) surface present very good agreement with previous literature studies, while observed changes in the electronic properties of the Au/Pt(111) system below the Fermi level are mainly connected to the interaction of Au atoms with Pt(111) surface.

References

[1] P.W. Davies, M.A. Quinlan, G.A. Samorjai, *Surf. Sci.* **121** (1982) 290.

[2] J.W.A. Sachtler, G.A. Somorjai, *J. Catal.* **81** (1983) 77.

[3] J.W.A. Sachtler, G.A. Somorjai, *J. Catal.***89** (1984**)** 35.

[4] R.C. Yeates, G.A. Somorjai *J. Catal.***103** (1987) 208.

[5] R. Meyer, C. Lemire, S.K. Shaikhutdinov, H.J. Freund, *Gold Bull.* **37** (2004) 72.

[6] T. Kobiela, Z. Kaszkur, R. Duś *Thin Solid Films* **78** (2005) 152.

[7] T. Kobiela, M. Moors, W. Linhart, I. Cebula, A. Krupski, C. Becker, K. Wandelt, *Thin Solid Films* **518** (2010) 3650.

[8] M. Salmeron, S. Ferrer, M. Jazzar, G.A. Samorjai, *Phys. Rev. B* **28** (1983) 6758.

[9] B. Vogt, B. Schmiedeskamp, U. Heinzmann, *Z. Phys. B Condens. Matter* **80** (1990) 359.

[10] P. Stoppmanns, B. Heidemann, N. Irmer, N. Mueller, B. Vogt, B. Schmiedeskamp, U. Heinzmann, E. Tamura, R. Feder, *Phys. Rev. Lett.* **66** (1991) 2645.

[11] E. Sibert, F. Ozanam, F. Maroun, O.M. Magnussen, R.J. Behm, *Phys. Rev. Lett.* **90** (2003) 0561021.

[12] E. Sibert, F. Ozanam, F. Maroun, R.J. Behm, O.M. Magnussen, *Surf. Sci.* **572** (2004) 115.

[13] H.C. Potter, J.M. Blakely, *J. Vac. Sci. Technol.* **12** (1975) 635.

[14] J. Hulse, J. Kueppers, K. Wandelt, G. Ertl, *Appl. Surf. Sci.* **6** (1980) 453.

[15] MaTeck. Available online: http://www.mateck.com/ (accessed on 27 April 2015).

[16] S.M. Foiles, M.I. Baskes, M.S. Daw, *Phys. Rev. B* **33** (1986) 7983.

[17] Friatec. Available online: http://www.friatec.de/ (accessed on 27 April 2015).

[18] Goodfellow. Available online: http://www.goodfellow.com/ (accessed on 27 January 2015).

[19] SigmaAldrich. Available online: http://www.sigmaaldrich.com (accessed on 27 January 2015).

[20] I. Horcas, R. Fernández, J.M. Gómez-Rodríguez, J. Colchero, J. Gómez-Herrero, A.M. Baro, *Rev. Sci. Instrum.* **78** (2007) 013705.

[21] Ph. Avouris, R. Wolkow, *Phys. Rev. B* **39** (1989) 5091.

[22] M.N. Piancastelli, N. Motta, A. Sgarlata, A. Balzarotti, M. de Crescenzi, *Phys. Rev. B* **48** (1993) 17892.

[23] F.J. Giessibl, *Science* **267** (1995) 68.

[24] H. Neddermeyer, *Rep. Prog. Phys.* **59** (1996) 701.

[25] W. Kohn, L.J. Sham, *Phys. Rev. A* **140** (1965) 1133.

[26] P. Hohenberg, W. Kohn, *Phys. Rev. B* **136** (1964)

[27] M.D. Segall, P.J.D. Lindan, M.J. Probert, C.J. Pichard, P.J. Hasnip, S.J. Clark, M.C. Payne. *J. Phys. Condens. Matter* **14** *(*2002), 2717.

[28] J.P. Perdew, J.A. Chevary, S.H. Vosko, K.A. Jackson, M.R. Pederson, D.J. Singh, C. Fiolhais *Phys. Rev. B* **46** (1992) 6671.

[29] J.P. Perdew, K. Burke, M. Ernzerhof, *Phys. Rev. Lett.* **77 (**1996) 3865.

[30] D. Vanderbilt, *Phys. Rev. B* **41** (1990) 7892.

[31] H.J. Monkhorst, J.D. Pack. *Phys. Rev. B* **13** (1976) 5188.

[32] T.H. Fischer, J.J. Almlof, *J. Phys. Chem.* **96** (1992) 9768.

[33] W.B. Pearson, *A Handbook of Lattice Spacings and Structures of Metals and Alloys*; Pergamon Press: New York, NY, USA, 1967; Volume 2.

[34] E. Bauer, *Appl. Surf. Sci.* **11/12** (1982) 479.

[35] J. Tersoff, *Phys. Rev. Lett.* **74** (1995) 434.

[36] L. Vitos, A.V. Ruban, H.L. Skriver, J. Kollar, *Surf. Sci.* **411** (1998) 186.

[37] W.R. Tyson, W.A. Miller, *Surf. Sci.* **62** (1977) 267.

[38] F.R. De Boer, R. Boom, W.C.M. Mattens, A.R. Miedema, A.K. Niessen, *Cohesion in Metals*; North-Holland: Amsterdam, The Netherlands, 1988.

[39] C.T. Campbell,. *Annu. Rev. Phys. Chem.* **41** (1990) 775.

[40] N.E. Sinhg-Miller, N. Marzari, *Phys. Rev. B* **80** (2009) 2354071.

[41] J.L.F. Da Silva, C. Stampft, M. Scheffler, *Surf. Sci.* **600** (2006) 703.

[42] C. Kittel, *Introduction to Solid State Physics*, 7th ed.; Wiley: New York, NY, USA, 1996.

[43] J.R. Kitchin, J.K. Norskov, M.A. Barteau, J.G. Chen, *J. Chem. Phys.* **120** (2004) 10240.

[44] L. Schminka, J. Harl, A. Stroppa, A. Grueneis, M. Marsman, F. Mittendorfer, G. Kresse, *Nat. Mater.* **9** (2010) 741.

[45] F. Behafarid, L.K. Ono, S. Mostafa, J.R. Croy, G. Shafai, S. Hong, T.S. Rahman, S.R. Bare, B.R. Cuenya, *Phys. Chem. Chem. Phys.* **14** (2012) 11766.

[46] X. Liu, Y. Sui, T. Duan, Ch. Meng, Y. Han, *Phys. Chem. Chem. Phys.* **16** (2014) 23584.

[47] E. German, I. Lopez-Corral, S. Pirillo, A. Juan, G. Brizuela, *Appl. Surf. Sci.* **303** (2014) 324.

[48] PL-Grid. Available online: http://www.plgrid.pl/en (accessed on 27 January 2015).

[49] L.L. Kesmodel, G.A. Samorjai, *Phys. Rev. B* **11** (1975) 630.

[50] L.L. Kesmodel, P.C. Stair, G.A. Somorjai, *Surf. Sci.* **64** (1975) 342.

[51] D.L. Adams, H.B. Nielsen, M.A. van Hove, *Phys. Rev. B* **20** (1979) 4789.

[52] R. Feder, H. Pleyer, P. Bauer, N. Mueller, *Surf. Sci.* **109** (1981) 419.

[53] K. Hayek, H. Glassl, A. Gutmann, H. Leohard, *Surf. Sci.* **152–153** (1985) 419.

[54] D.F. Ogletree, M.A. van Hove, G.A. Samorjai, *Surf. Sci.* **173** (1986) 351.

[55] N. Materer, U. Starke, A. Barbieri, R. Doell, K. Heinz, M.A. van Hove, G.A. Samorjai, *Surf. Sci.* **325** (1995) 207.

[56] R. Felici, M. Pedio, F. Borgatti, S. Iannotta, M. Capozi, G. Ciullo, A. Stierle, *Nat. Mater.* **4** (2005) 688.

[57] P.J. Feibelman, *Phys. Rev. B* **56** (1997) 2175.

[58] A. Dhouib, H. Guesmi, *Chem. Phys. Lett.* **521** (2012) 98

Chapter 5

Surface termination of $Pt_3Ti(111)$

5.1. Introduction

Hydrogen based energy systems seem to be a very good approach for the future as the expansion of the clean energy storage and production technicues. At this point that is challenging issues of ongoing scientific studies. Presently, there is need for making better platinum based cathode catalysts for the oxygen reduction reaction. It could help to the platinum loading reduction [1]. One of the methods to achieve high-effective electro catalysts is combining two or more metals togheter. Such procedure may lead to new surface phenomena, which can be interesting for their catalytic properties. For example, using Pt-alloys with the 3d and 4d-transition metals (e.g. Ni, Co, Ti, V, Zr, Fe) results in electro catalytic research [2-4] called 'volcano-type.' It seems, that for the Pt_3M alloys the maximum in the catalytic activity is casued by the interaction between the adsorption of rective intermediates and the efficiency of the electron transfer to adsorbates. It means, if the cathode catalysts bind oxygen to strongly then the oxygen reduction reaction is minimized by the desorption ratio. Differently, the oxygen reduction reaction is limited by the electron transfer rate to the oxygen moleculer. For the Pt_3M alloys the catalytic activity could be connected with the electronic structure of materials [2-4]. Because interaction between adsorbate and metal depends on the 0_2 2p-states and the metal d-states, the d-band center corresponds exactly as the chemisorption energy to the kinetic of the oxygen reduction reaction and that is why it can be applied as a measure of the catalytic activity for the platinum alloy. The rules of the development of the efficient electro cataysts based on calculated as well as experimental sets of results seem to be reasonable [2-5]. Namely, the d-band center of an perfect electro catalyst should be shifted around -0.2 eV relative to the one of platinum and the catalyst should bind the O_2 about 0.2 eV weaker than platinum atoms. On the other hand, the production of a perfect electro catalyst is experimentaly complex, even if the influence of the 3d and 4d- transition metals on the oxygen reduction reaction rate. One of the main problems is the enhanced dissolution of the transition metal in aqueous solutions with respect to platinum. Because it could cause an increase of platinum in the surface area [6]. The other important point is the surface segregation processes which can depend on the composition of the considered system. The segregation process turns out to be a source of changes in the surface electronic structure of Pt_3M alloys [2,5]. It was shown theoretically [5] that a strong platinum segregation to the outermost layer occurs in alloys, especially Pt_3Ti, whose platinum concentration is above 75%. With the use of low-enery electron diffraction and low-energy ion-scattering measurements, and after the usual preparing conditions of the Pt_3M-crystals, a platinum skin covers the atomic layers underneath and in addition acts as protective layer [2–4,7-8]. The described properties are especially of importance with respect to a high corrosion resistance of the alloy. It should be pointed out, that at the present state it is still not clear whether the Pt3M layer beneath the Platinum-skin is Platinum depleted or not [4-5,9-11].

5.2. Experimental Details

The UHV system was equipped with a Createc low temperature STM, a combined MCP-LEED/Auger spectrometer, a sputter gun for surface preparation and a mass spectrometer for rest gas analysis. Base working pressure was 1 x 10^{-10} mbar. The $Pt_3Ti(111)$ crystal was purchased from MaTecK and has been prepared under UHV conditions by several cycles of ion sputtering with neon gas (beam energy of 1 keV; sample current of 3 - 4 μA). Next, in order to decrease number of dislocations and to reestablish the surface stoichiometry the sample was annealed up to 1200 K after each sputter cycle. The surface quality has been checked by AES and LEED. All STM measurements were performed under LN_2 cooling with the use of mechanically cut Pt-Ir tip.

5.3. Theoretical Details

All calculations were performed based on the pseudo-potential plane-wave within the density functional theory [12,13], using the Cambridge serial total energy package (CASTEP) [14]. The effects of exchange correlation interaction are treated with the generalized gradient approximation (GGA) of Perdew-Burke-Ernzerhof (PBE) [15,16]. The ultra-soft pseudo-potentials [17] describe this electron-ion interaction system to high accuracy with a plane wave energy cutoff of 600 eV. The energy calculations in the first irreducible Brillouin-zone were conducted by using the (4×4×1) k-point grid of the Monkhorst-Pack scheme [18]. Spin polarization of platinum was included in the calculations to correctly account for its magnetic properties. All atomic positions have been relaxed according to the total energy and force using the BFGS scheme [19] based on the cell optimization criterion RMS force of 0.03 eV/Å, stress of 0.05 GPa, and displacement of 0.001 Å. The calculation of total energy and electronic structure is followed by cell optimization with SCF tolerance of 1×10^{-6} eV/atom. The Pt(111) surface was modeled using a slab containing 7 (=16.02 Å) and 10 (=22.88 Å) layers of Pt atoms with a vacuum gap in the [111] direction equal to 20.8 Å and 30.71 Å, respectively. Full slab relaxation was performed in both cases.

5.4. Results and Discussion

First of all, the LEED pattern of the clean $Pt_3Ti(111)$ surface at E=180 eV electron beam energy after Ne gas sputtering surface cleaning and thereafter annealing cycles (Figure 5.1.(a)) has been taken.

Typically, metal alloys with structure like Cu_3Au structure are expected to be created by ABCABC… stacking layers. All of them should consist of three platinum atoms and one titanium atom per unit cell. It means, that titanium atoms form a p(2×2) superlattice with respect to the p(1×1) lattice of a Pt(111) surface.

The expected p(2×2) superstructure spots are visible (Figure 5.1.a) and the dedicated vectors for unit cell are 5.54 Å and 2.76 Å. The collected LEED images suggest that the crystal surface is well-ordered in the surface region. However, the LEED images do not provide any information about the composition of the topmost surface layers.

Figure 5.1.(b) presents a typical STM image of the $Pt_3Ti(111)$ surface with true atomic layer step and dislocations. Such dislocations are characteristic for the Pt(111) surfaces. The observed step height around 2.3 ± 0.3 Å (Figure 5.1.(c)) is in good agreement with the crystallographic data.

The atomic resolution STM image of the $Pt_3Ti(111)$ surface is shown in Figure 5.1.(d). One can see very evidently the hexagonal symmetry with long-range character of the $Pt_3Ti(111)$ single crystal surface. The observed unit cell of the titanium is related to the p(2×2) superstructure with a unit cell constant of 5.6 Å. The atomically resolved STM image of the $Pt_3Ti(111)$ surface reveals three positions wth equivalent electron density forming a triangle and one position which seems to be isolated [21]. This discussed above platinum-skin surface could also show the same symmetry as a result from the surface electronic structure due to the bulk structure.

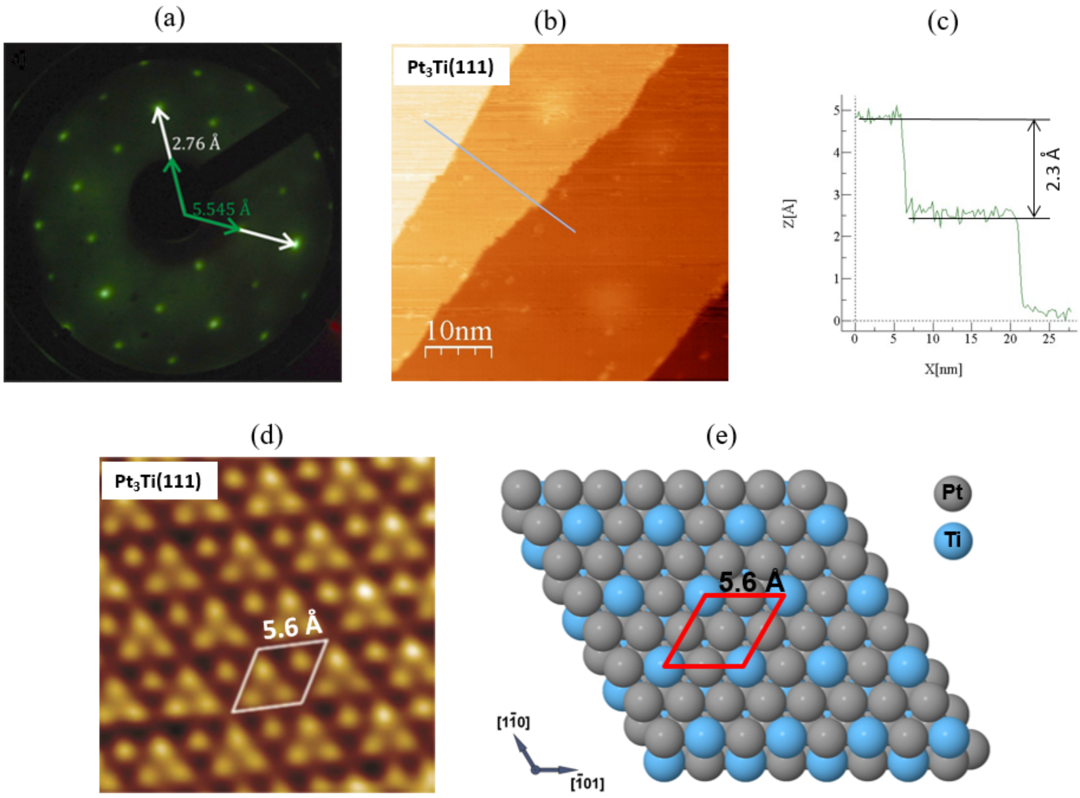

Figure 5.1. *(a) LEED patterns for a clean $Pt_3Ti(111)$ surface recorded at normal electron incidence for E = 180 eV, and T = 300 K; (b) T = 25 K (578 Å × 578 Å, I_T = 100 pA, U_{bias} = +23 mV); (c) line-scan corresponding to line drawn in (b); (d) UHV-STM of the Pt_3Ti surface after repeated cleaning cycles with atomic resolution (2500 Å × 2500 Å, 0.006 V, 7.9 nA, (low pass filtered)[21] - the unit cell is outlined; and (e) theoretical model of $Pt_3Ti(111)$.*

Until now, the STM studies of the $Pt_3Ti(111)$ surface show the recurrence of the bulk crystal. On the other hand, since STM results present a connection of the electronic structure and morphology this does not prove that the Pt_3Ti crystal has a bulk-like termination. Furthermore, if we take into account the noticable sublayer dependence of the binding energies of adsorbates [10,20] then it means that the d-band center and the electronic structure of the probed surface depends at least on the topmost layer.

The theoretical part of presented work covers the calculations of multilayer relaxations of the $Pt_3Ti(111)$, $Pt_3Ti(111)$-Pt terminated (Pt_3Ti-Pt) and $Pt_3Ti(111)$-Ti terminated

(Pt_3Ti-Ti) systems using the slab with 7 atomic layers. Figure 5.2 shows the schematic view

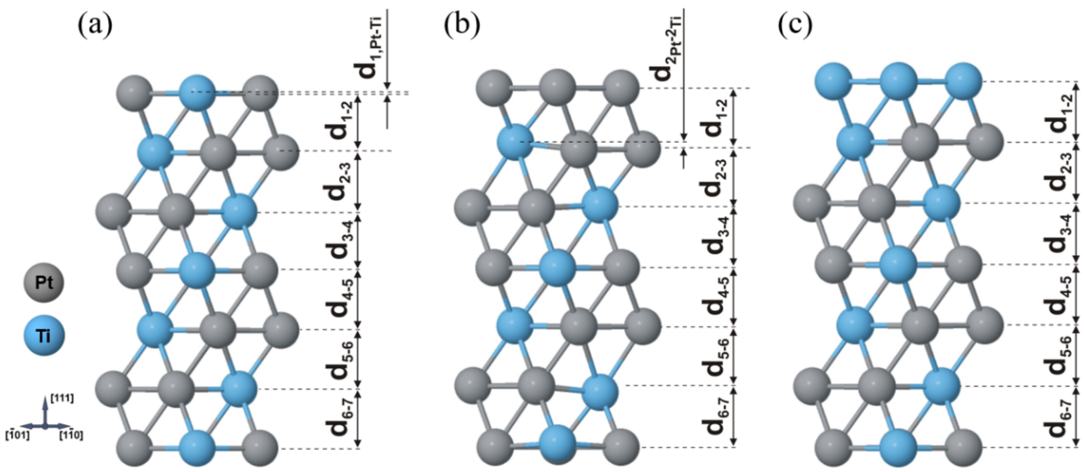

Figure 5.2. *Side view of the relaxed $Pt_3Ti(111)$ Surface: (a) $Pt_3Ti(111)$-Pt terminated Surface; (b) $Pt_3Ti(111)$-Ti terminated surface (c) for seven layers. Values of denoted characteristic inter plane distances are given in Table 6.1-3.*

of relaxed slabs structure for the seven layers of Pt_3Ti (Figure 5.2.(a)), Pt_3Ti-Pt (Figure 5.2.(b)), and Pt_3Ti-Ti (Figure 5.2.(c)). The platinum low-index surface was modeled by repeated slabs with a (1×1) surface unit cell with one Ti atom and three Pt atoms in each layer for Pt_3Ti, four Pt atoms in the top layer in Pt_3Ti-Pt and four Ti atoms in the top layer of Pt_3Ti-Ti. The calculated atomic layer distances for seven planes are shown in Table 5.1 for Pt_3Ti, Table 5.2 for Pt_3Ti-Pt and Table 5.3 for Pt_3Ti-Ti. d_{i-j}^{X-Y} defines the distance along the surface normal direction between the *X* atom at the *i* atomic layer and the *Y* atom at the *j* atomic layer. Surface relaxation Δd_{i-j}^{X-Y} is defined as the percent of change of the spacing between layers *i* and *j versus* the bulk layer spacing (d^0). The bulk value (d_0) is taken from our GGA calculations and describes average distance between atomic planes of seven (=2.27 Å) for Pt_3Ti and Pt_3Ti-Pt and (=2.29) for Pt_3Ti-Ti are almost the same as those following STM measurements (=2.30 Å) with the difference close to 1%. The calculated value of the surface free energy for γ_{Pt3Ti} = 1.74 J/m^2, $\gamma_{Pt3Ti\text{-}Pt}$ = 1.49 J/m^2 and $\gamma_{Pt3Ti\text{-}Ti}$ = 2.55 J/m^2 where the surface free energy of the Pt(111) surface (2.299 J/m^2 < $\gamma_{Pt(111)}$ < 2.489 J/m^2) [22-26]. The calculated value of the work function for the Φ_{Pt3Ti}=4.723eV, $\Phi_{Pt3Ti\text{-}Pt}$=4.935eV and $\Phi_{Pt3Ti\text{-}Ti}$=4.042eV and it is in very good agreement for Pt terminated surface with the experimental value of the work function Φ_{Pt3Ti}=5.02eV [27] measured by UPS for the clean surface of the $Pt_3Ti(111)$ face. According to the theoretical calculations [21], and predictions of

Duan's *et al.* this could make surface segregation processes up to a Pt outermost layer [5]. Number of times the $Pt_3Ti(111)$ sample was sputter suggest the termination of the $Pt_3Ti(111)$ single crystal, i.e. termination by a monolayer of Pt (Pt_3Ti-Pt).

d_{i-j}^{X-Y}(Å)	CASTEP *7 layers*	d_{i-j}^{X-Y}(Å)	CASTEP *7 layers*
Bulk value	2.27	d_{3-4}^{Pt-Ti}	2.22
d_{1-1}^{Ti-Pt}	-0.18	d_{4-5}^{Pt-Pt}	2.28
d_{1-2}^{Pt-Pt}	2.33	d_{4-5}^{Ti-Ti}	2.34
d_{1-2}^{Ti-Ti}	1.89	d_{4-5}^{Ti-Pt}	2.34
d_{1-2}^{Ti-Pt}	2.16	d_{4-5}^{Pt-Ti}	2.28
d_{1-2}^{Pt-Ti}	2.07	d_{5-6}^{Pt-Pt}	2.28
d_{2-3}^{Pt-Pt}	2.27	d_{5-6}^{Ti-Ti}	2.28
d_{2-3}^{Ti-Ti}	2.53	d_{5-6}^{Ti-Pt}	2.28
d_{2-3}^{Ti-Pt}	2.53	d_{5-6}^{Pt-Ti}	2.28
d_{2-3}^{Pt-Ti}	2.27	d_{6-7}^{Pt-Pt}	2.28
d_{3-4}^{Pt-Pt}	2.27	d_{6-7}^{Ti-Ti}	2.34
d_{3-4}^{Ti-Ti}	2.22	d_{6-7}^{Ti-Pt}	2.28
d_{3-4}^{Ti-Pt}	2.28	d_{6-7}^{Pt-Ti}	2.34

Table 5.1. *Calculated distances ($\mathbf{d_{i-j}^{X-Y}}$) between the atomic planes of the relaxed $Pt_3Ti(111)$ system for the slab with seven atomic layers.*

d_{i-j}^{X-Y}(Å)	CASTEP *7 layers*	d_{i-j}^{X-Y}(Å)	CASTEP *7 layers*
Bulk value	2.27	d_{4-5}^{Pt-Pt}	2.26
d_{1-2}^{Pt-Pt}	2.35	d_{4-5}^{Ti-Ti}	2.22
d_{1-2}^{Pt-Ti}	2.09	d_{4-5}^{Ti-Pt}	2.25
d_{2-2}^{Pt-Ti}	-0.26	d_{4-5}^{Pt-Ti}	2.22
d_{2-3}^{Pt-Pt}	2.23	d_{5-6}^{Pt-Pt}	2.26
d_{2-3}^{Ti-Ti}	2.38	d_{5-6}^{Ti-Ti}	2.54
d_{2-3}^{Ti-Pt}	2.49	d_{5-6}^{Ti-Pt}	2.29
d_{2-3}^{Pt-Ti}	2.11	d_{5-6}^{Pt-Ti}	2.51
d_{3-4}^{Pt-Pt}	2.25	d_{6-7}^{Pt-Pt}	2.31
d_{3-4}^{Ti-Ti}	2.37	d_{6-7}^{Ti-Ti}	2.29
d_{3-4}^{Ti-Pt}	2.37	d_{6-7}^{Ti-Pt}	2.26
d_{3-4}^{Pt-Ti}	2.26	d_{6-7}^{Pt-Ti}	2.23

Table 5.2. *Calculated distances ($\mathbf{d_{i-j}^{X-Y}}$) between the atomic planes of the relaxed $Pt_3Ti(111)$-Pt terminated system for the slab with seven atomic layers.*

d_{i-j}^{X-Y}(Å)	CASTEP *7 layers*
Bulk value	2.29
d_{1-2}	2.30
d_{2-3}	2.29
d_{3-4}	2.30
d_{4-5}	2.26
d_{5-6}	2.34
d_{6-7}	2.21

Table 5.3. *Calculated distances ($\mathbf{d_{i-j}^{X-Y}}$) between the atomic planes of the relaxed $Pt_3Ti(111)$-Pt terminated system for the slab with seven atomic layers.*

Furthermore, during the STM measurements [21], large terraces with a termination of Pt_3Ti-Pt and two special defects, a bright one (D1) and a dark one (D2), Figure 5.3, at V_{bias} = 0.58 V and V_{bias} = 1.30 V, were observed, respectively.

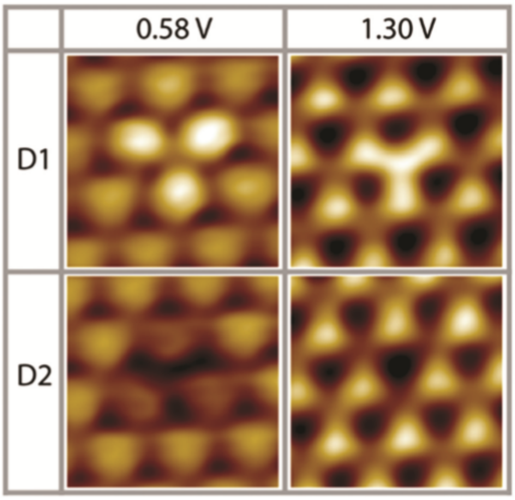

Figure 5.3. *Two different characteristic surface defects on Pt_3Ti-Pt, D1 and D2 (0.58 V, 0.48 nA; 1.30 V, 0.11 nA; low pass filtered; 1.7 nm × 1.7 nm) [21].*

Figure 5.4 shows possible Pt adsorption sites on the $Pt_3Ti(111)$ surface (Figure 5.4.(a)), and Pt_3Ti-Pt surface (Figure 5.4.(b)) with the on top adsorption positions T1, T2, T3 and T4, hollow hcp positions H6, H8, hollow fcc position F5, and bridge position B7.

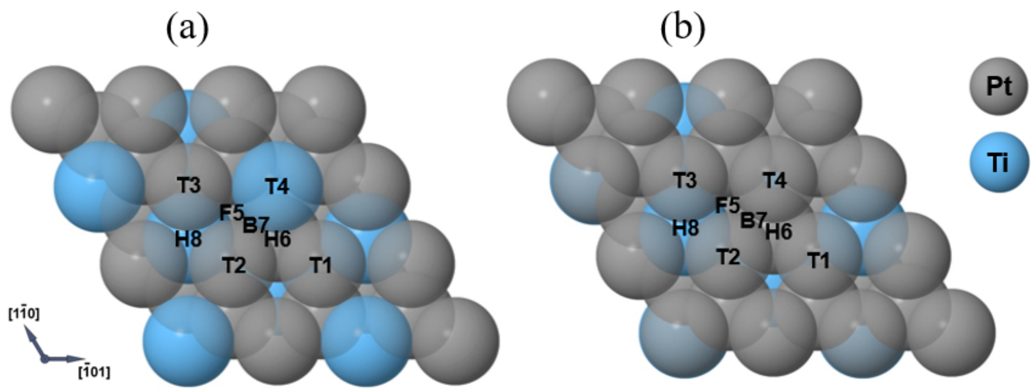

Figure 5.4. *Considered positions of Pt adsorption on the $Pt_3Ti(111)$: (a) and Pt_3Ti-Pt terminated (b) surface: T—on top; F—hollow fcc; H—hollow hcp; and B—bridge.*

The minimum adsorption energy (E_{ads}) was calculated by means of the following total energy difference:

$$E_{ads} = E_T\left(\frac{Pt}{Pt_3Ti\ or\ Pt_3Ti-Pt}\right) - E_T(Pt) - E_T(Pt_3Ti\ or\ Pt_3Ti-Pt) \qquad (5.1)$$

where E_T is the total energy of the system and $\frac{Pt}{Pt_3Ti\ or\ Pt_3Ti-Pt}$, Pt, and Pt_3Ti or Pt_3Ti-Pt refer to the atom-on-metal system, the free Pt atom, and the bare Pt_3Ti or Pt_3Ti-Pt surface, respectively.

Tables 5.4 and 5.5 displays the predicted adsorption energies of Pt on the $Pt_3Ti(111)$ surface and on the Pt_3Ti-Pt terminated surface, respectively.

Considere adsorption position	Atom position after calculation	E_{ads} (eV)
T1	T1→H8	
T2	T2→H8	0.7
T3	T3→H8	
T4	T4	0.6
F5	F5	-0.9
H6	H6	
B7	B7→H6	0.7
H8	H8	

Table 5.4. *Calculation results of the one Pt adsorption atom on the $Pt_3Ti(111)$ surface. E_{ads}—adsorption energy; T1 → H8 means that after calculations platinum atom has moved from the on top position T1 towards the most favorable hollow hcp position H8.*

Considere adsorption position	Atom position after calculation	E_{ads} (eV)
T1	T1→H8	
T2	T2→H8	-0.82
T3	T3→H8	
T4	T4	-0.33
F5	F5	-0.11
H6	H6	-0.8
B7	B7→H6	
H8	H8	-0.82

Table 5.5. *Calculation results of the one Pt adsorption atom on the Pt_3Ti-Pt terminated surface. E_{ads}—adsorption energy; T1 → H8 means that after calculations platinum atom has moved from the on top position T1 towards the most favorable hollow hcp position H8.*

Comparison of the calculated adsorption energies suggest that the Pt_3Ti-Pt surface is preferred. This is in good comparison with the STM experimental results [21]. The adsorption energy of the platinum atom on the $Pt_3Ti(111)$ surface is not favorable and the adsorption place is unstable, see Table 5.4. The most prefered position of the Platinum atom on the Pt_3Ti-Pt terminated surface is the hollow *hcp* (H8 and H6 with the $E_{ads} = -0.82$ eV and $E_{ads} = -0.8$ eV, respectively). The on top position T4 is also prefered with the adsorption energy $E_{ads} = -0.33$ eV. There is good agreement between the experimental data, Figure 5.3 [21] and our theoretical calculations. Namely, the D1 (Figure 5.4) triangles defects are composed by three platinum atoms in contact with a titanium atom from the 2nd atomic layer with the H8 adsorption position. That is why, the Pt atoms appear slightly brighter at $V_{bias} = 0.58$ V, while at $V_{bias} = 1.30$ V the triangles defect is located above a Ti atom in the third layer – T4 adsorption position appear darker.

It looks that a defect in the third layer is monitored, what have influence in a lower energy of the unoccupied surface electronic states. That could be happen when for example Ti atom will repleac position of Pt atom. This is possible because at lower bias voltage mostly unoccupied electronic states at higher energy be conducive to the noticable STM image. As a result, a visible defect in 2nd atomic layer can cause a shift in the surface electronic states to higher energies. It means, defects visible on the STM images for Pt_3Ti-Pt terminated surface [21] can suggest that configurations of atoms at 2nd and 3rd layer have influance for the electronic structure.

5.5. Conclusions

In this work, experimental and theoretical studies of the geometrical properties of the (111) surface of ordered Pt/Pt_3Ti(111) adsorption system have been presented. The analysis of LEED, UPS and STM measurements indicate that we have a Pt terminated surface. Based on LEED results, no change of the lattice constant for Pt_3Ti(111) or Pt_3Ti-Pt terminated was observed. The topography of the obtained STM images of Pt_3Ti(111) surfaces on the level of the atomic resolution demonstrate that the surface structures have hexagonal arrangement of atoms and that the the unit cell of the Ti related p(2 × 2) superstructure with a cell constant of 5.6 Å presents atomic resolution of the Pt_3Ti(111) face with the difference close to 1%. The calculated surface free energy shows that Pt terminated surface is the most stable ($\gamma_{Pt3Ti\text{-}Pt}$ = 1.49 J/m^2 < γ_{Pt3Ti} = 1.74 J/m^2 < $\gamma_{Pt3Ti\text{-}Ti}$ = 2.55 J/m^2). The calculated value of the work function is $\Phi_{Pt3Ti\text{-}Pt}$=4.935eV and it is in very good agreement for Pt terminated surface with the experimental value of the work function Φ_{Pt3Ti}=5.02eV [27]. The calculated adsorption energy of the Pt atom on the Pt_3Ti-Pt terminated surface is dependent on the adsorption site and from Ti atoms in the 2nd and 3rd layer, and there is a preference for a hollow *hcp* site (E_{ads} = −0.82 eV) and top site T4 (E_{ads} = −0.33 eV). Adsorption sites are in very good agreement with previous literature studies, while the hcp position with Ti atom in 2nd layer an on top position with Ti atom in the 3rd layer are compatibile with the observed defects [21].

References

[1] H. Duan, Q. Hao, C. Xu, J. *Power Sources*, **280** (2015) 483.

[2] V.R. Stamenkovic, B.S. Mun, M. Arenz, K.J.J. Mayrhofer, C.A. Lucas, G. Wang, P.N. Ross, N.M. Markovic, *Nat. Mater.,* **6** (2007) 241.

[3] J. Greeley, I.EL. Stephens, A.S. Bondarenko, T.P. Johansson, H.A. Hansen, T.F. Jaramillo, J. Rossmeisl, I. Chorkendorff, J. K. Norskov, *Nat. Chem.,* **1** (2009) 552.

[4] V. Stamenkovic, B.S. Mun, K.J.J. Mayrhofer, P.N. Ross, N.M. Markovic, J. Rossmeisl, J. Greeley and J.K. Norskov, *Angew. Chem., Int. Ed.*, **118** (2006) 2963.

[5] Z. Duan, J. Zhong, G. Wang, *J. Chem. Phys.,* **133** (2010) 114701.

[6] A. Stassi, C. d'Urso, V. Baglio, A. di Blasi, V. Antonucci, A.S. Arico, A.M. Castro Luna, A. Bonesi, W.E. Triaca, *J. Appl. Electrochem*., **36** (2006) 1143.

[7] W. Chen, J.A. K. Paul, A. Barbieri, M.A. van Hove, S. Cameron, D.J. Dwyer, *J. Phys.: Condens. Matter,* **5** (1993) 4585.

[8] W. Chen, L. Severin, M. Göthelid, M. Hammar, S. Cameron, J. Paul, Phys. Rev. B: *Condens. Matter*, **50** (1994) 5620.

[9] M. A. Vasiliev, J. Phys. D: *Appl. Phys.,* **30** (1997) 3037.

[10] H.-C. Tsai, T.H. Yu, Y. Sha, B.V. Merinov, P.-W. Wu, S.-Y. Chen and W.A. Goddard, *J. Phys. Chem. C*, **118** (2014) 26703.

[11] W. Yu, M.D. Porosoff, J.G. Chen, *Chem. Rev.,* **112** (2012) 5780.

[12] W. Kohn, L.J. Sham, *Phys. Rev. A* **140** (1965) 1133,

[13] P. Hohenberg, W. Kohn, *Phys. Rev. B* **136** (1964)

[14] M.D. Segall, P.J.D. Lindan, M.J. Probert, C.J. Pichard, P.J. Hasnip, S.J. Clark, M.C. Payne, *J. Phys. Condens. Matter **14** (*2002) 2717.

[15] J.P. Perdew, J.A. Chevary, S.H. Vosko, K.A. Jackson, M.R. Pederson, D.J. Singh, C. Fiolhais, *Phys. Rev. B* **46** (1992) 6671.

[16] J.P. Perdew, K. Burke, M. Ernzerhof, *Phys. Rev. Lett.* **77** (1996) 3865.

[17] D. Vanderbilt, *Phys. Rev. B* **41** (1990) 7892.

[18] H.J. Monkhorst, J.D. Pack. *Phys. Rev. B* **13** (1976) 5188.

[19] T.H. Fischer, J.J. Almlof, *J. Phys. Chem.* **96** (1992) 9768.

[20] T. H. Yu, T. Hofmann, Y. Sha, B.V. Merinov, D.J. Myers, C. Heske, W.A. Goddard, *J. Phys. Chem. C*, **117** (2013) 26598.

[21] M. Paßens, V. Caciuc, N. Atodiresei, M. Moors, S. Blügel, R. Wasera,, S. Karthäuser, *Nanoscale,* **8** (2016) 13924.

[22] E. Bauer, *Appl. Surf. Sci.* ***11/12*** (1982) 479.

[23] J. Tersoff, *Phys. Rev. Lett.* **74** (1995) 434.

[24] L. Vitos, A.V. Ruban, H.L. Skriver, J. Kollar, *Surf. Sci.* **411** (1998) 186.

[25] W.R. Tyson, W.A. Miller, *Surf. Sci.* **62 (1977)** 267.

[26] F.R. De Boer, R. Boom, W.C.M. Mattens, A.R. Miedema, A.K. Niessen, *Cohesion in Metals*; North-Holland: Amsterdam, The Netherlands, 1988.

[27] S. Le Moal1 , M.Moors, J. M. Essen, Ch. Breinlich, C. Becker, K. Wandelt, J. Phys.: *Condens. Matter* **25** (2013) 045013.

Chapter 6

Conclusions and Future Work

6.1. Conclusion

In this thesis a wide range of techniques have been used to gtowth optimization of $TiO_2/LaAlO_3(001)$ system. State-of-the-art fabrication by UHV-PLD was used to take advantage of such controlled thin film deposition. In summary, it has been shown that the degree of order of epitaxial anatase-TiO_2 thin films can be manipulated by varying growth parameters such as the sample temperature, sample to target distance, oxygen pressure, laser energy, and laser pulse frequency. The results obtained clearly demonstrate that the TiO_2 thin film, which covers the entire substrate, has a distinctly anatase phase, and can be atomically aligned and bonded to $LaAlO_3(001)$ substrate. Anatase-TiO_2 thin films showed high crystalline quality, evidenced by RHEED, XRD, LEED, and atomic resolution STEM. Two, very well ordered domains (1×4) and (4×1) surface reconstruction of anatase were observed by RHEED and LEED. An analysis of the STM measurements indicates the coexistence of atomic steps of both 2.5 Å and 5 Å, confirming the existence of two TiO_2 domains. The STEM images also reveal that the interface is most likely terminated with a LaO layer.

Two other systems Au/Pt(111) and $Pt/Pt_3Ti(111)$ was focused on experimental and theoretical studies of the geometrical and electronic properties. For the Au/Pt(111) analysis of LEED and STM measurements indicates that for a coverage below 1 ML, two-dimensional growth of the first Au monolayer takes place. Based on LEED results, no change of the lattice constant after gold adsorption was observed. The topography of the obtained STM images of Pt(111) and Au/Pt(111) surfaces on the level of the atomic resolution demonstrate that the surface structures have hexagonal arrangement of atoms and that the surface lattice constant is equal to the distance between the nearest platinum surface atoms (=2.80 Å). This is in very good agreement (close to 1%) with our presented DFT calculations, where the distances between the nearest atoms in the case of bare Pt(111) and Au/Pt(111) surface equal to 2.83 Å. It was shown that the first and second interlayer spacings of the clean Pt(111) surface were determined to be expanded by +0.87% and contracted by −0.43%, respectively. The calculated adsorption energy of the Au atom on the Pt(111) surface is dependent on the adsorption site, and there is a preference for a hollow *fcc* site (E_{ads} = −0.578 eV). In the presence of gold layer on the Pt(111) surface, the top interlayer spacing was found expanded by +2.16% with respect to the ideal bulk value. Density of states for the Pt(111) surface present very good agreement with previous literature studies, while observed changes in the electronic properties of the Au/Pt(111) system below the Fermi level are mainly connected to the interaction of Au atoms with Pt(111) surface.

Geometrical properties of (111) surface of ordered Pt/Pt_3Ti(111) adsorption system analysis by LEED, UPS and STM measurements indicate that we have Pt terminated surface. Based on LEED results, no change of the lattice constant for Pt_3Ti(111) or Pt_3Ti-Pt terminated was observed. The topography of the obtained STM images of Pt_3Ti(111) surfaces on the level of the atomic resolution demonstrate that the surface structures have hexagonal arrangement of atoms and that the the unit cell of the Ti related p(2×2) superstructure with a cell constant of 5.6 Å presents atomic resolution of the Pt_3Ti(111) face with the difference close to 1%. The calculated surface free energy shown that Pt terminated surface is the most stable ($\gamma_{Pt3Ti\text{-}Pt}$ = 1.49 J/m^2 < γ_{Pt3Ti} = 1.74 J/m^2 < $\gamma_{Pt3Ti\text{-}Ti}$ = 2.55 J/m^2). The calculated value of the work function for the $\Phi_{Pt3Ti\text{-}Pt}$=4.935eV and it is in very good agreement for Pt terminated surface with the experimental value of the work function Φ_{Pt3Ti}=5.02eV [27]. The calculated adsorption energy of the Pt atom on the Pt_3Ti-Pt terminated surface is dependent on the adsorption site and from Ti atoms in the 2nd and 3rd layer, and there is a preference for a hollow *hcp* site (E_{ads} = −0.82 eV) and top site T4 (E_{ads} = −0.33 eV). Adsorption site are in very good agreement with previous literature studies, while the hcp position with Ti atom in 2nd layer an on top position with Ti atom in the 3rd layer are compatibile with the observed defects.

6.2. Future work

Based on achieved results for the TiO_2, Au/Pt(111) and Pt_3Ti(111) further studies should be continued. Before studying more complex adsorption systems it is important to describe and understand well the electronic and atomic structure of all three presented systems. From that point of few future work should focus on performing experiments at Diamond Light Source at higher resolution using Angle

Resolved Photoemission Spectroscopy (ARPES) – beamline IO5 and Surface X-ray Diffraction (SXRD) – beamline IO7.

In the case of TiO_2 surface it could be interesting to check if the reconstructed surface can act as a templete for growth of ordered metal clusters (e.g. gold). These studies should involve experimental techniques such as LEED, XPS, STM and SXRD.

The presented result for Au/Pt(111) suggest that further theoretical studies are required for better understanding of the adsorption process of gold on the Pt(111) surface.

For the $Pt_3Ti(111)$ system it seems that further insights into relationship between production procedure of bimetallic Pt-Ti alloys and their respective resulting surface termination are needed in order to systematically optimize their catalytic activity.

Appendage I

Materials **2015**, *8*, 2935-2952; doi:10.3390/ma8062935

OPEN ACCESS

materials

ISSN 1996-1944

www.mdpi.com/journal/materials

Article

Structure Determination of Au on Pt(111) Surface: LEED, STM and DFT Study

Katarzyna Krupski [1], Marco Moors [2], Paweł Jóźwik [3], Tomasz Kobiela [4] and Aleksander Krupski [1,3,5,*]

[1] Department of Physics, University of Warwick, Coventry CV4 7AL, UK; E-Mail: k.j.krupski@warwick.ac.uk

[2] Peter Grünberg Institut, Forschungszentrum Jülich, Wilhelm-Johnen-Str., 52425 Jülich, Germany; E-Mail: m.moors@fz-juelich.de

[3] Department of Advanced Materials and Technologies, Faculty of Advanced Technologies and Chemistry, Military University of Technology, Kaliskiego 2 Str., 00-908 Warszawa, Poland; E-Mail: pjozwik@wat.edu.pl

[4] Faculty of Chemistry, Warsaw University of Technology, ul. Noakowskiego 3, 00-664 Warsaw, Poland; E-Mail: kobiela@ch.pw.edu.pl

[5] Faculty of Science, SEES, University of Portsmouth, Portsmouth PO1 3QL, UK

* Author to whom correspondence should be addressed; E-Mail: aleksander.krupski@port.ac.uk.

Academic Editor: Marco Salerno

Received: 20 January 2015 / Accepted: 8 May 2015 / Published: 27 May 2015

Abstract: Low-energy electron diffraction (LEED), scanning tunneling microscopy (STM) and density functional theory (DFT) calculations have been used to investigate the atomic and electronic structure of gold deposited (between 0.8 and 1.0 monolayer) on the Pt(111) face in ultrahigh vacuum at room temperature. The analysis of LEED and STM measurements indicates two-dimensional growth of the first Au monolayer. Change of the measured surface lattice constant equal to 2.80 Å after Au adsorption was not observed. Based on DFT, the distance between the nearest atoms in the case of bare Pt(111) and Au/Pt(111) surface is equal to 2.83 Å, which gives 1% difference in comparison with STM values. The first and second interlayer spacing of the clean Pt(111) surface are expanded by +0.87% and contracted by −0.43%, respectively. The adsorption energy of the Au atom on the Pt(111) surface is dependent on the adsorption position, and there is a preference for a hollow *fcc* site. For the Au/Pt(111) surface, the top interlayer spacing is expanded by +2.16% with respect to the ideal bulk value. Changes in the electronic properties of the Au/Pt(111)

system below the Fermi level connected to the interaction of Au atoms with Pt(111) surface are observed.

Keywords: density functional theory calculations; scanning tunneling microscopy; low-energy electron diffraction; surface structure; metallic surfaces; gold; platinum; metal-metal interfaces; low index single crystal surface

1. Introduction

A large number of studies on epitaxy have been carried out for many years. Ultra-thin epitaxial film systems exhibit a variety of interesting properties due to the strong correlation between the electronic structure of the film and its morphology, strain, and defect structure [1–10]. Structural studies of *fcc/fcc* systems provide a great deal of information on the connection between the geometrical properties of the adsorbed atomic layers and the atomic arrangements of the substrates. Various fields are concerned with epitaxial growth; these range from basic research on the growth mechanism of thin films to advanced research on the development of devices. Platinum is widely used as a catalyst in the chemical and petrochemical industries [11,12]. For example, in oil refineries, platinum catalysts are employed in processes that involve the reforming of paraffin and the hydrogenation of unsaturated hydrocarbons [11–14].

Applied Surface Science 388 (2016) 684–690

Contents lists available at ScienceDirect

Applied Surface Science

journal homepage: www.elsevier.com/locate/apsusc

Optimisation of anatase TiO_2 thin film growth on $LaAlO_3$(0 0 1) using pulsed laser deposition

K. Krupski [a,*], A.M. Sanchez [a], A. Krupski [a,b], C.F. McConville [a]

[a] Department of Physics, University of Warwick, Coventry CV4 7AL, UK
[b] Faculty of Science, SEES, University of Portsmouth, Portsmouth PO1 3QL, UK

ARTICLE INFO

Article history:
Received 15 January 2016
Received in revised form 23 February 2016
Accepted 24 February 2016
Available online 3 March 2016

Keywords:
Anatase
Titanium dioxide
Lanthanum aluminate
Pulsed laser deposition (PLD)
Reflection high-energy electron diffraction (RHEED)
Low-energy electron diffraction (LEED)
X-ray diffraction (XRD)
Atomic force microscopy (AFM)
Scanning tunneling microscopy (STM)
Scanning transmission electron microscopy (STEM)
Growth
Thin film growth

ABSTRACT

Optimisation of epitaxial anatase TiO_2 thin films grown on $LaAlO_3$(0 0 1) substrates was performed using ultra-high vacuum based pulsed laser deposition (PLD) and studied by in-situ reflection high-energy electron diffraction (RHEED). In addition, ex-situ X-ray diffraction (XRD), atomic force microscopy (AFM), and scanning transmission electron microscopy (STEM) were performed to characterise the bulk properties of these thin films. The deposited TiO_2 thin film is demonstrated to have anatase phase and bonded directly to the $LaAlO_3$(0 0 1) substrate. In a separate ultra-high vacuum system low-energy electron diffraction (LEED) and scanning tunneling microscopy (STM) measurements were performed and a well-ordered two-domain (1 × 4) and (4 × 1) reconstruction of anatase surface was observed. Analysis of the STM measurements indicates the coexistence of atomic steps of both 2.5 Å and 5.0 Å, confirming the existence of two TiO_2 domains. The atomic resolution STEM images reveal that the TiO_2/$LaAlO_3$ interface to be terminated with LaO layer and that the anatase-TiO_2 reconstruction was found to be stable during the film growth.